UNIVERSITY OF SOUTHAMPTON

FACULTY OF NATURAL AND ENVIRONMENTAL SCIENCES

Institute for Life Sciences

School of Chemistry

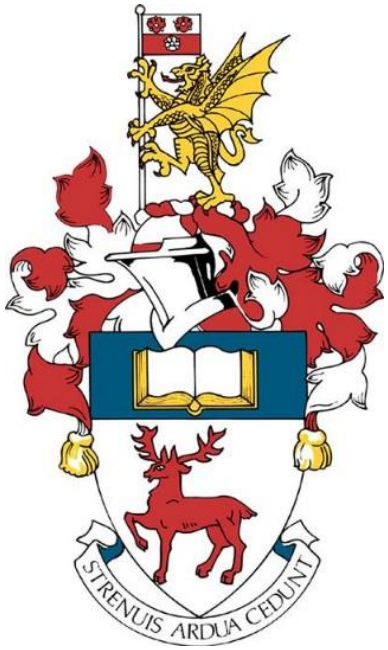

Multimodal label-free imaging to study skeletal stem cells and skeletal regeneration

Catarina da Costa Moura

Thesis for the degree of Doctor of Philosophy

June 2018

UNIVERSITY OF SOUTHAMPTON

ABSTRACT

FACULTY OF NATURAL AND ENVIRONMENTAL SCIENCES

Thesis for the degree of Doctor of Philosophy

MULTIMODAL LABEL-FREE IMAGING TO STUDY SKELETAL STEM CELLS AND SKELETAL REGENERATION

Catarina da Costa Moura

The use of skeletal stem cells (SSCs) in cell-based therapies is currently one of the most promising areas for the treatment of skeletal disease and skeletal tissue repair. The ability to control the modification of SSCs could provide significant therapeutic potential in regenerative medicine, with the prospect to permanently repopulate a host with stem cells. Current limitations in the characterisation of SSC differentiation have led to the development and application of alternative strategies that aim to identify molecules at the subcellular level using their inherent properties, without the use of a dye or label, *i.e.* label-free.

Label-free imaging methods are emerging as powerful alternatives to conventional techniques in biomedicine. The work presented in this thesis aimed to investigate SSC differentiation and to engineer strategies to generate skeletal tissue and temporally evaluate SSC development using multimodal and label-free imaging approaches.

The differentiation process of adult human bone marrow SSCs into adipocytes was evaluated using coherent anti-Stokes Raman scattering (CARS) imaging. CARS provided an enhanced resolution of lipid droplets compared to conventional staining, detectable as early as 24 hours after adipogenic induction.

The combination of CARS microscopy with second harmonic generation (SHG) and two-photon excited auto-fluorescence (TPEAF) offered a novel insight into the chondrogenic differentiation of human fetal-femur derived skeletal cells. Retrieval of 3D information using a non-invasive and non-destructive platform enabled elucidation of the temporal changes in cartilage development.

Subsequently, multimodal label-free imaging was used to investigate the differentiation of live human fetal-femur derived skeletal cells differentiated into chondrogenic cultures. The results demonstrated that label-free CARS live-cell imaging at the molecular level did not significantly affect cell differentiation and development into cartilage. Moreover, it was demonstrated that CARS microscopy is a suitable platform to image additional key molecules of interest, namely proteins and glycosaminoglycans, with bioengineered cartilage tissue imaged at different wavenumbers.

The ability to dynamically follow the formation of new regenerated tissues in real-time using non-invasive techniques offers exciting opportunities for the design and development of innovative tissue engineering solutions for hard and soft tissues. This thesis indicates that multimodal label-free imaging with non-linear techniques such as CARS and SHG are suitable approaches for the assessment of bioengineered skeletal tissues with potential clinical translation.

Table of Contents

Table of Tables

Table of Figures

Abbreviations

ACAN – Aggrecan

ACTB – β-actin

ADSC – Adipose-derived stem cell

AEC – 3 amino-9-ethyl-carbazole

ALPL – Alkaline Phosphatase

BSA – Bovine serum albumin

CARS – Coherent anti-Stokes Raman scattering

cDNA – Complementary deoxyribonucleic acid

COL10A1 – Alpha-1 Type X Collagen

COL1A1 – Alpha-1 Type I Collagen

COL2A1 – Alpha-1 Type II Collagen

CpC – Collagen per cell

DMEM – Dulbecco's modified Eagle medium with glucose and L-glutamine

DMEM/F12 – Dulbecco's modified Eagle medium: nutrient mixture F-12

DMSO – Dimethyl sulfoxide

DNA – Deoxyribonucleic acid

EDTA – Ethylenediamine tetra-acetic acid

FABP4 – Fatty Acid Binding Protein 4

FCS – Fetal calf serum

GADPH – Glyceraldehyde-3-Phosphate Dehydrogenase

gDNA – Genomic deoxyribonucleic acid

IBMX – 3-isobutyl-1-methylxanthine

ITS – Insulin-transferrin-selenium liquid media supplement

MACS – Magnetic activated cell sorting

MSC – Mesenchymal stem cell

OPO – Optical parametric oscillator

PBS – Phosphate buffered saline

PPARG – Peroxisome Proliferator Activated Receptor Gamma

qPCR – Reverse transcription quantitative polymerase chain reaction

RNA – Ribonucleic acid

SHG – Second harmonic generation

SOX9 – Transcription Factor SOX9

SSC – Skeletal stem cell

TGF-β3 – Transforming growth factor beta 3

TPEAF – Two-photon excited auto-fluorescence

UK – United Kingdom

USA – United States of America

α-MEM – Alpha minimum essential medium with deoxyribonucleotides, ribonucleotides and L-glutamine

2D – Two-dimensional

3D – Three-dimensional

Declaration of Authorship

I, Catarina da Costa Moura, declare that this thesis entitled "*Multimodal label-free imaging to study skeletal stem cells and skeletal regeneration*" and the work presented in it are my own and has been generated by me as the result of my own original research, unless when specifically stated otherwise.

I confirm that:

1. This work was done wholly while in candidature for a research degree at this University;
2. Where any part of this thesis has previously been submitted for a degree at this University this has been clearly stated;
3. Where I have consulted the published work of others, this is always clearly attributed;
4. Where I have quoted from the work of others, the source is always given. With the exception of such quotations, this thesis is entirely my own work;
5. I have acknowledged all main sources of help;
6. Where the thesis is based on work done by myself jointly with others, I have made clear exactly what was done by others and what I have contributed myself;
7. Parts of this work have been published or have been submitted for publication as:
    a) Catarina Costa Moura, Konstantinos N Bourdakos, Rahul S Tare, Richard OC Oreffo, Sumeet Mahajan. "Three-dimensional, non-destructive, live-cell imaging of bioengineered cartilage tissue using multimodal non-linear microscopy", *Nature Communications*, 2018. – i*n preparation;*
    b) Catarina Costa Moura, Stuart A. Lanham, Tual Monfort, Konstantinos N. Bourdakos, Rahul S. Tare, Richard O. C. Oreffo, Sumeet Mahajan. "Quantitative temporal interrogation in 3D of bioengineered human cartilage using multimodal label-free imaging", *Integrative Biology*, 2018. – *submitted;*
    c) Catarina Costa Moura, Rahul S Tare, Richard OC Oreffo, Sumeet Mahajan. "Raman spectroscopy and coherent anti-Stokes Raman scattering imaging: prospective tools for monitoring skeletal cells and skeletal regeneration*", Journal of the Royal Society Interface*, 2016. 13(118): pii 20160182. doi: 10.1098/rsif.2016.0182 (2015 IF: 3.818);
    d) Catarina Costa Moura, Rahul S Tare, Richard OC Oreffo, Sumeet Mahajan, "Non-destructive techniques to follow skeletal stem cell development for

skeletal repair and regeneration". *European Cells & Materials*, 2016. Annual meeting of the Tissue and Cell Engineering Society, Vol. 31, Suppl. 1, p. 248. (2015 IF: 4.560) – *abstract in conference proceedings*;

e) Justyna P Smus*, Catarina Costa Moura*, Emma McMorrow, Rahul S Tare, Richard OC Oreffo, Sumeet Mahajan. "Tracking adipogenic differentiation of skeletal stem cells by label-free chemically selective imaging", *Chemical Science*, 2015. 6: p. 7089-7096. doi: 10.1039/C5SC02168E (2014 IF: 9.211) * these authors contributed equally to this work;

f) Catarina Costa Moura, Justyna P Smus, Rahul S Tare, Richard OC Oreffo, Sumeet Mahajan, "Assessing early skeletal stem cell differentiation into adipocytes using coherent anti-Stokes Raman scattering microscopy". *European Cells & Materials*, 2015. Annual meeting of the Tissue and Cell Engineering Society, Vol. 29, Suppl. 3, p. 6. (2014 IF: 4.886) – *abstract in conference proceedings*;

Signed: ……

Date: ……

Acknowledgements

I am deeply thankful to my supervisors Prof Sumeet Mahajan, Prof Richard Oreffo and Dr Rahul Tare, for giving me the opportunity to come to Southampton. I am grateful for their support and guidance as mentors. We had so many valuable discussions which, above all, have enabled me to develop my own research ideas and perspectives. I almost feel I came to Southampton to join the 'Three Musketeers'. And in that case, I really hope that after performing many adventurous experiments and overcoming obstacles I will triumph and join you as the new 'D'Artagnan'.

Bruno Sarmento, Professora Salette Reis and José das Neves – thank you for your guidance during the time I was doing research in Portugal. You have inspired me in so many ways. You made me feel special and that I could make a difference in science and that's why I decided to embark on a PhD. I will always be grateful to you for believing in me.

I would like to thank the Molecular Biophotonics and Imaging group for so many valuable insights and fruitful discussions. In particular, thank you to Justyna, the co-author of my first *sotonian* paper, for our dynamic and enthusiastic collaboration; to Tual, for introducing me to CARS imaging; to Jack, for kindly assisting me during the Raman experiments; to Kostas, for taking care of the amazing multimodal label-free imaging system in our lab; and to Billy and Steph, the old chaps who also started their PhD journeys in this group at the same time as I did.

Thank you to all in the Bone and Joint Research group. I had a great time with you, and you have made my experience in Southampton so much better. I am grateful to all who advised me on experimental protocols, in particular Lauren and Matt, for their useful tips in histology; Emma, for fetal sample preparation procedures; Roxanna, for kindly assisting me during the confocal fluorescence imaging; and Stuart, for his expertise in 3D video reconstruction. Thank you to May, the B&J molecular queen, for sharing her molecular biology expertise and for introducing me to qPCR. For the best technical support we could ask for – thank you to Julia, Stef and Kate. And I am grateful to Janos, not only for all his assistance with the faxitron and visits to the BRF, but also for always being there to solve all the issues and to answer all our questions.

I would like to thank David Chatelet from the Biomedical Imaging Unit for all our productive discussions about image processing and analysis.

I am also grateful I had the opportunity to meet another facet of research during my PhD in Southampton – public engagement. Thank you to Jon, Steve and Tony, for giving me the chance to talk about my research work at various different and unexpected places (including the amazing Glastonbury Festival!).

During my stay in Southampton I met wonderful and inspiring people and I would like to thank you all for being there. In particular Estrela, a brilliant scientist and one of the most resilient woman I have ever met, and Antonio, the friend I had the privilege to meet here in Southampton and who was always there. SRC Southampton and Parkrun played a very important role during my PhD journey. I started running, for the first time, in Southampton. Running was something completely unbearable for me. I started challenging myself and it was amazing how running showed me how powerful we all are. Running taught me we can do everything – we just need to believe in ourselves, fight and pursue our goals. I still can't believe I completed a marathon just a couple of weeks before submitting this thesis!

A big thank you, from the bottom of my heart, to the best parents in the whole world, Luísa and Antero, and the most amazing sister, Patrícia, who always supported all of my dreams and hopes. You decided to fly with me to Southampton in September 2014, to make sure I was well. You understood I was taking an important step in my career and you stood by my side. Thank you so much for being there. Always! Vovô, Lena, Tio Toni, Tia Fernanda, Inês, Sara, Nuno, Lili and Leo – I feel I am the luckiest with such an incredible family! I just wish my grandmother, Vovó, was here with me today, so we could celebrate together the end of my PhD journey. She is my true inspiration to be a strong Woman.

And finally, a massive thank you to my rock, Miguel. My everything. It was a pleasure sharing this amazing journey with my best friend. I have no words to say how grateful and happy I am to have you in my life. I truly admire your perseverance and hard work, and you are a real inspiration for me. Thank you for your endless love, support and laughs.

Thank you. ♥

PREFACE

This thesis was submitted to the Faculty of Natural and Environmental Sciences, University of Southampton, as a partial fulfilment of the requirements for the degree of Doctor of Philosophy.

The research work discussed in this thesis was performed at the Institute for Life Sciences and at the Centre for Human Development, Stem Cells and Regeneration, Institute of Developmental Sciences, University of Southampton, between October 2014 and December 2017.

This thesis is written in the form of a 'Three-Paper PhD'. In Chapter 1, I introduce skeletal stem cell research and highlight the motivation of the research conducted in this thesis. In Chapter 2, I introduce the label-free imaging techniques used in this thesis, and provide an overview of its recent applications in skeletal cell research. A detailed description of the methodologies used is described in Chapter 3. Chapter 4, Chapter 5 and Chapter 6 present work published (or to be submitted) to peer-reviewed scientific journals. The research papers constitute the majority of the substantive work in the thesis. To close, in Chapter 7 I present indications for further investigations and discuss future directions on multimodal label-free imaging in skeletal cell research.

Professor Sumeet Mahajan (Professor of Molecular Biophotonics & Imaging) Professor Richard Oreffo (Professor of Musculoskeletal Science and Director of the Centre for Human Development, Stem Cells and Regeneration) and Doctor Rahul Tare (Lecturer in Musculoskeletal Science and Bioengineering) supervised the work presented in this thesis.

The viva voce examination was held on the 30th May 2018. The examining team was formed by Professor Alistair Elfick (PhD Biomedical Engineering, Head of Research Institute and Chair of Synthetic Biological Engineering) and Doctor Edward Rogers (PhD, Senior Research Fellow in the University of Southampton Optoelectronics Research Centre).

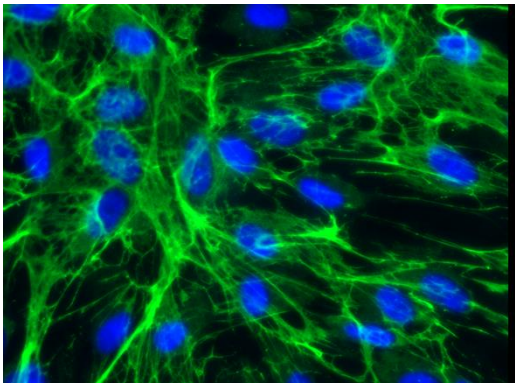

1

Background and Motivation

Chapter 1 introduces skeletal stem cell research and highlights the motivation of the research conducted in this thesis.

Throughout the last century, medical breakthroughs have led to a tremendous increase in life expectancy. However, as a consequence, an increasing aging population has resulted in an increase in age-related diseases, as well as associated reductions in quality of life, leading to a dramatic impact on healthcare.

Skeletal tissue loss due to injury or disease results in significantly reduced quality of life at significant socio-economic cost. Fractures alone cost the European economy €17 billion and the US economy $20 billion annually [1]. In the US, there are around 8 million bone fractures per year, of which approximately 5% to 10% are associated with delayed healing or non-union. Each year in the UK there are approximately 150,000 wrist, vertebral and hip fractures due to osteoporosis, with an estimated healthcare cost of £2.1 billion per annum. Thus, novel and effective medical approaches are essential to fulfil the current demographic challenges [2-4].

The use of stem cells for cell-based therapies is one of the most promising and exciting areas for tissue repair and disease treatment, including those affecting brain, skeletal muscle, and heart [5, 6]. In fact, the unique properties of stem cells, with their ability to self-renew and potential to differentiate into several different specialised cell types, present an ideal tool for reparative medicine [2, 7].

1.1 Skeletal stem cells

The bone marrow, which is the major site of haematopoiesis (the process which leads to the formation of all blood cells), serves as a reservoir for a variety of cells, including haematopoietic cells as well as cells of the non-haematopoietic stroma [3, 8-10]. The bone-marrow stroma constitutes the scaffold that supports the regulation of haematopoiesis, establishing and maintaining the haematopoietic microenvironment necessary for growth and blood-cell maturation [8, 11]. Bone marrow stromal cells include osteoblasts, macrophages, and reticular cells [8]. Within the bone marrow stroma resides a rare multipotent stem cell population called the skeletal stem cell (SSC). The term “skeletal stem cell” is all too frequently confused with “mesenchymal stem cell” (MSC) in the literature (reviewed in Bianco and Robey 2015 [11]). However, MSCs are developmentally distinct from skeletal lineages, and it is important to recognise that the various extra-skeletal tissues and organs noted to retain MSCs are not generated by skeletal progenitors present in bone marrow. The term “skeletal stem cell”, as eloquently detailed by Bianco and Robey [12], denotes specifically the rare population of postnatal non-haematopoietic stromal cells found in the bone marrow with the capacity to regenerate bone and bone marrow stroma (reviewed in Dawson *et*

al. 2014 [2]), and the term SSC will be used throughout this thesis to refer to this select population.

SSCs are self-renewing multipotent cells that give rise to the skeletal lineages and which also act as organisers and regulators of the local bone marrow microenvironment [13, 14]. Depending on the microenvironment, SSCs can generate cartilage, develop into bone-forming cells responsible for bone growth during development and bone re-modelling, and form adipocytes during bone marrow remodelling and growth [3, 15, 16]. The ability to generate bone, cartilage, bone marrow stroma and adipocytes characterises the SSC (Figure 1.1).

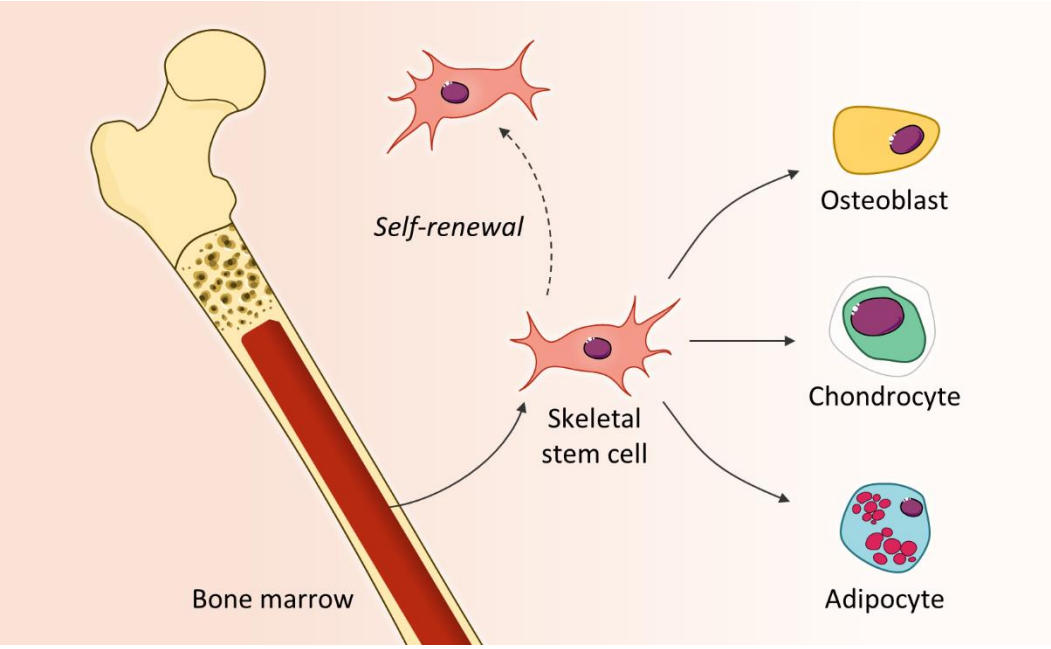

Figure 1.1 – The differentiation potential of skeletal stem cells (SSCs). A population of SSCs can be enriched from the human bone marrow, and expanded *in vitro*. Under appropriate conditions the SSCs have the ability to self-renew and to differentiate towards bone, cartilage and fat lineages.

The unique properties of SSCs have attracted significant attention within the medical community, and promise new opportunities for the use of SSCs for theoretical and practical advances in medicine [2, 9, 17]. SSCs have the potential to be used as a conceptual tool to study skeletal cell biology, as learning tools for cell-based models of health and disease, or as building blocks in bone and cartilage tissue engineering for a range of musculoskeletal conditions.

1.2 Clinical translation of SSCs

Pivotal in the development of successful therapies for bone and cartilage augmentation will be the design of well-defined and reproducible protocols for SSCs [3, 15, 16]. Questions still remain concerning i) SSC isolation and expansion; ii) SSC

differentiation towards the relevant skeletal tissue; iii) SSC delivery to the site of interest; and iv) SSC state and function following transplantation into the human body.

Controlled differentiation of stem cells offers significant therapeutic potential in skeletal regeneration, with the prospect to permanently repopulate a host with stem cells, an objective that could be achieved by careful monitoring and characterisation of the differentiation process of SSCs. Currently, SSC differentiation can be evaluated through a number of assays including colorimetric assays [18], reverse transcription quantitative polymerase chain reaction (qPCR) [18, 19], histochemical analysis [19], and immunohistochemical assays [20]. These methods reveal the detailed biochemical features of SSCs and provide important information regarding their state of differentiation. However, labelling can be a significant disadvantage when studying cellular and intracellular processes, as fluorescent molecules may influence and bias the results by altering the physiological or physical properties of the cell of interest [21, 22]. Current approaches for SSC characterisation are invasive, require cell fixation or cell lysis [23-25], and are unsuitable for time-course studies and SSC monitoring for therapeutic use.

The current limitations in the characterisation of SSC differentiation have led to the need to find new alternatives. Ideally, SSC differentiation would be monitored using a non-destructive method that would allow the identification of molecules at the subcellular level by using their inherent properties.

The work described in this thesis exploits and develops the application of novel imaging methods to examine and investigate SSC differentiation and skeletal tissue formation over time, non-invasively. Using non-invasive and non-destructive approaches to study skeletal regeneration will offer a step change in medical research and will ultimately lead to more effective ways to repair bone and cartilage, with widespread potential in other diseases.

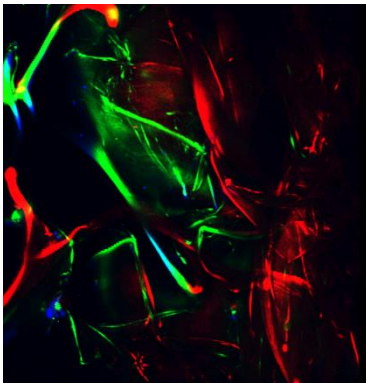

2

LABEL-FREE IMAGING

The second chapter introduces the label-free imaging techniques used in this thesis, namely coherent anti-Stokes Raman scattering (CARS), second harmonic generation (SHG) and two-photon excited auto-fluorescence (TPEAF) microscopy, and provides an overview of its recent applications in skeletal cell research.

Human skeletal cell populations offer significant potential as a cell source for tissue engineering applications, and in particular for skeletal tissue regeneration strategies. The development of appropriate tools to follow skeletal cell development and monitor the formation of newly engineered tissue in real-time, non-invasively or non-destructively is crucial and remains, to date, an unmet goal.

Microscopes are an essential instrument in imaging and have offered the potential to *see* an invisible world of significant complexity. Prospective imaging approaches seek to identify molecules at subcellular level without using any dye or label, *i.e.* 'label-free', but by using the intrinsic properties of the molecules.

2.1 Light-Matter Interactions

For several generations the physics community have debated about the mysterious and incredible phenomenon of light and, at present, light is considered to be simultaneously a particle and a wave [26, 27].

The electromagnetic spectrum consists of an enormous array of wavelengths and frequencies (Figure 2.1), ranging from Gamma rays (the highest energy waves) to radio waves (the lowest energy waves), including visible light [27]. Although these waves have different properties, they all have the extraordinary wave-particle duality and travel at the same speed in vacuum (c = 299792458 m/s [28]).

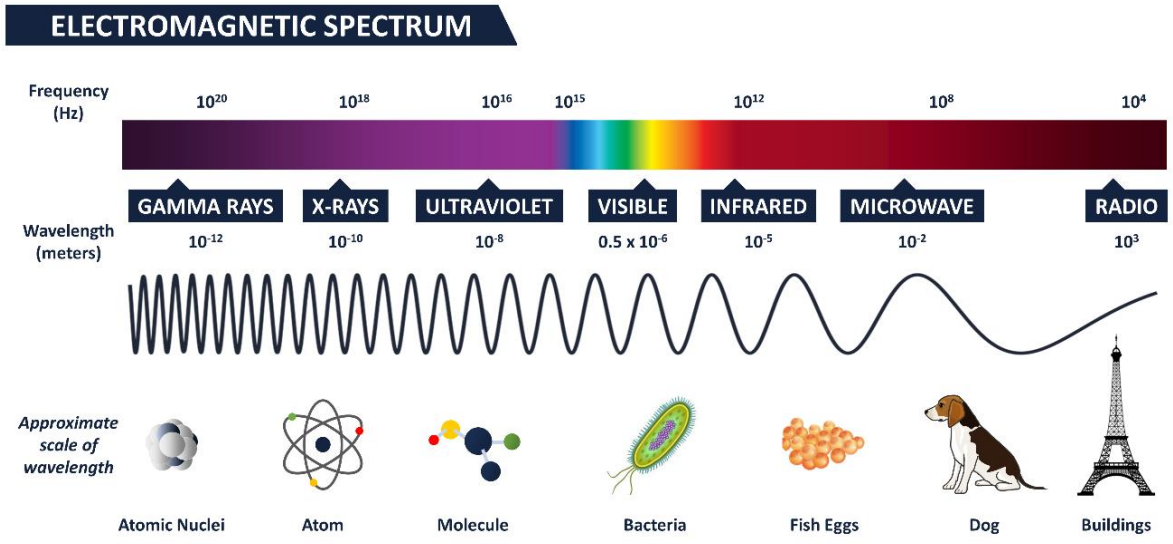

Figure 2.1 – The electromagnetic spectrum. Gamma waves have the highest frequencies and shortest wavelengths, and radio waves have the lowest frequencies and longest wavelengths [26, 27].

Interaction of light with matter involved in spectroscopy and imaging can be explained by its particle nature, *i.e.* in terms of interactions of photons with the state

of the matter. A photon, the elementary particle of light (quantum) [26], can be absorbed, emitted or scattered by a material. Absorption can be interpreted as a material gaining energy from photons, whereas emission of photons will cause a loss of energy from the material [27].

Scattering occurs when energy waves such as light are forced to deviate from a straight path due to interactions with a material. A common example of light scattering is the explanation for why the sky is blue [29]. Sunlight reaches Earth's atmosphere and encounters molecules of the gases present in the atmosphere. Blue light has shorter wavelength, and because scattering has wavelength dependence this light wave interacts with a higher number of molecules and is scattered more (Figure 2.2). That is why we see a blue sky most of the time. When we see the sun lower in the sky during sunset or sunrise, sunlight needs to travel a longer distance to reach our eyes. In this instance, blue light is scattered out away from line of sight (as it scatters more than red wavelengths), and red wavelengths prevail and become visible to us (Figure 2.2).

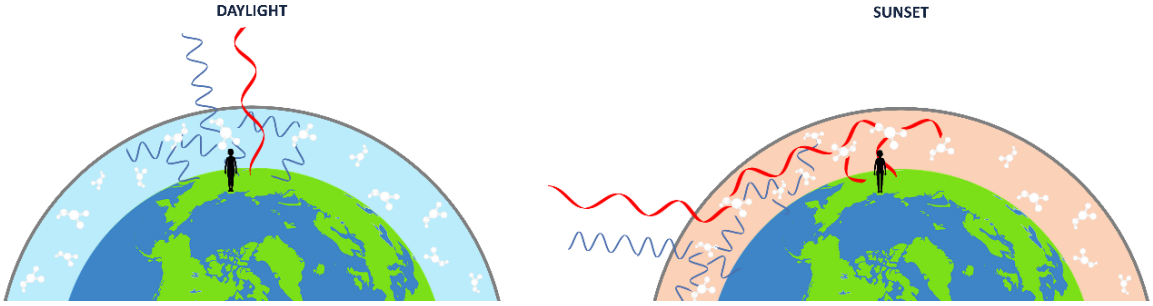

Figure 2.2 – Schematic explanation of Rayleigh scattering – the colour of the sky is caused by the scattering of sun light off the molecules present in the atmosphere [29].

The previous example is known as Rayleigh scattering, where light interacts with a molecule and is scattered elastically, with the same frequency as the incident light, *i.e.* without any loss or gain in energy (Figure 2.3a). However, a few incident photons interact and exchange energy with the molecular bond vibration, resulting in inelastically scattered light known as Raman scattering [30].

Raman scattering occurs when a photon exchanges energy with the molecular vibration and is inelastically scattered. When the molecule interacts with a photon, it is excited into an instantaneous virtual energy level and, almost immediately, emits another photon at a slightly different wavelength. If the incident photon loses energy to the molecular bond vibration, a red-shifted Stokes photon, *i.e.* a photon with a longer wavelength, is generated and the molecule ends up in a higher vibrational state (Figure 2.3b). If the molecule of interest is already in a higher vibrational state, a blue-shifted anti-Stokes scattering occurs, resulting in the emission of a lower wavelength photon

(Figure 2.3c). The difference in frequency between incident and scattered photons corresponds to the vibrational energy level of the molecule [30-33], and is usually called Raman shift.

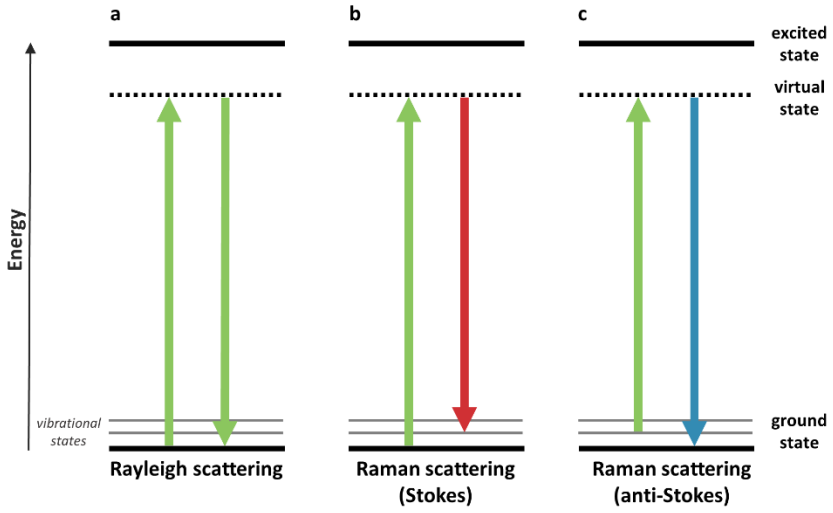

Figure 2.3 – Schematic diagram of the energy transitions involved in Rayleigh scattering (a) and Raman scattering (b and c). Raman scattering occurs through the interaction of an incident photon with a molecular vibration mode, gaining (anti-Stokes scattering, blue-shifted) or losing (Stokes scattering, red-shifted) an amount of energy equal to that vibrational mode [34].

2.2 The Raman Effect

Raman scattering occurs via interaction of an incident photon with a molecular vibrational mode. Two different theories can be used to explain the Raman effect of light: i) classical wave theory and ii) quantum theory of radiation.

According to the quantum theory of radiation [35], light is considered to be a stream of photons which collide with a molecule, and

$$E = h\nu$$

E is the energy (Joules), ν the frequency of radiation (s^{-1}), and h the Planck's constant, equal to 6.626×10^{-34} J s.

When a photon is incident on a molecule, if the collision is perfectly elastic, the photons will be scattered unchanged – Rayleigh scattering. However, it may happen that energy is exchanged between the photon and the molecule (inelastic scattering). The energy change, ΔE, represents a change in the vibrational and/or rotational energy of the molecule [36]. If the molecule gains energy ΔE, the photon will be scattered with energy E equal to ($h\nu - \Delta E$), thus the equivalent radiation will have a frequency equal

to (ν - $\Delta E/h$). If the molecule loses energy, the scattered photon will have a frequency equal to (ν + $\Delta E/h$).

According to the classical theory [36], light is considered as an electromagnetic field. When a molecule is in a static electric field, positive and negative charges experience oppositely directed forces. This separation of charge centres results in an induced electric dipole moment, and the molecule becomes polarized [36]. The size of the induced electric dipole, μ, depends on the magnitude of the applied electric field, E, and on the ability of the molecule to be distorted:

$$\mu = \alpha E$$

α is the polarizability of the molecule. Molecular polarizability is determined by the ease with which the electron cloud has to interact with an electric field.

When a sample is subject to an oscillating electromagnetic field of frequency ν, the electric field becomes:

$$E = E_0 \sin(2\pi \nu t)$$

E_0 is the maximum possible field strength. As the electric field oscillates, the induced dipole also undergoes oscillations of matching frequency ν:

$$\mu = \alpha E = \alpha E_0 \sin(2\pi \nu t)$$

The classical theory of Rayleigh scattering is explained in this equation, when the oscillating dipole emits radiation of its own oscillation frequency ν. However, if the molecule undergoes some vibration motion, the polarizability of the molecule will change periodically:

$$\alpha = \alpha_0 + \beta \sin(2\pi \nu_{vib} t)$$

α_0 represents the equilibrium polarizability, and β the rate of change of polarizability of the molecule. Then, we may write:

$$\mu = \alpha E = [\alpha_0 + \beta \sin(2\pi \nu_{vib} t)] E_0 \sin(2\pi \nu t)$$

Finally, using the trigonometric relation, $\sin(A) \sin(B) = \frac{1}{2} [\cos(A-B) - \cos(A+B)]$, we have:

$$\mu = \alpha_0 E_0 \sin(2\pi \nu t) + \frac{1}{2} \beta E_0 [\cos(2\pi (\nu - \nu_{vib})t) - \cos(2\pi (\nu + \nu_{vib})t)]$$

The induced electric dipole moment varies with the component frequencies ν, (ν - ν_{vib}), and (ν + ν_{vib}), representing Rayleigh, Stokes, and anti-Stokes scattering,

respectively [36]. If the polarizability of the molecule does not change, the rate of change of polarizability of the molecule ß will be 0, and the induced dipole oscillates only at the frequency of the incident radiation (Rayleigh scattering).

As each molecule is unique with its own set of characteristic bonds and therefore vibrational modes, Raman scattering provides a molecular 'fingerprint'. Given that cells and tissues are composed of different molecules, Raman spectroscopy is, potentially, a powerful tool to generate a characteristic signature of SSCs and skeletal tissues.

Raman spectroscopy offers additional advantages for the study of living cells including: i) high spatial resolution, ii) qualitative and quantitative spectral information, iii) ability to detect at the subcellular level, and iv) the ability to analyse cells in real time without altering cell function, as a laser operating at the visible/near-infrared region is applied to prevent significant damage to proteins, DNA, RNA, and other present biomolecules [37-41].

2.2.1 Characterisation of SSCs using Raman spectroscopy

The last decade has witnessed the use of Raman spectroscopy in the search for prospective spectral markers for characterising stem cells, including murine embryonic stem cells [23, 42-44], human embryonic stem cells [24, 45-48], MSCs [24, 49, 50], SSCs [39, 51, 52], adipose-derived stem cells (ADSCs) [24, 53], as well as the monitoring of stem cell differentiation into skeletal tissues [24, 39, 49, 52, 53]. Table 2.1 summarises the current applications of Raman spectroscopy in stem cell research and the major outcomes. Studies relevant for skeletal regeneration are discussed further in detail.

Table 2.1 – Raman spectroscopy applications in stem cells. References are ordered chronologically and by cell type.

Reference (year)	**Cell type**	**Study**	**Main findings**
Notingher *et al.* (2004) **[43, 44, 54]**	Murine embryonic stem cells	Characterisation of murine embryonic stem cells	Changes in the Raman spectra in the RNA peak region can be used as a differentiation marker
Chan *et al.* (2009) **[45]**	Human embryonic stem cells	Embryonic stem cell differentiation into cardiomyocytes	Changes in the RNA and DNA Raman peaks, before and after differentiation
Chiang *et al.* (2009) **[49]**	Human mesenchymal stem cells	MSC differentiation into osteoblasts	Changes in the Raman spectra in the hydroxyapatite characteristic peak region during the osteogenic differentiation
Schulze *et al.* (2010) **[47]**	Human embryonic stem cells	Differentiation status of human embryonic stem cells	Identification of Raman bands and ratios (e.g. RNA/proteins) to indicate embryonic stem cell state of differentiation
Pijanka *et al.* (2010) **[50]**	Human embryonic stem cells & Human mesenchymal stem cells	Differences between human embryonic stem cells and MSCs	Raman scattering allowed to distinguish an increase in the DNA band when comparing the embryonic stem cells with the MSCs nuclei
Downes *et al.* (2011) **[24]**	Human embryonic stem cells	Characterisation of human embryonic stem cells	Differences in the Raman spectra between nucleus (higher levels of RNA) and cytoplasm (higher levels of protein and glycogen)
Downes *et al.* (2011) **[24]**	Human mesenchymal stem cells	MSC differentiation into osteoblasts	Changes in the Raman spectra in the hydroxyapatite, collagen and carbonate chemical shifts during the osteogenic differentiation
McManus *et al.* (2011) **[52]**	Human skeletal stem cells	SSC differentiation into osteoblasts	Changes in the spectra in the hydroxyapatite Raman shift during osteogenic differentiation; Measurement of carbonate-to-phosphate and mineral-to-matrix ratios at different stages of development
Downes *et al.* (2011) **[24]**	Human adipose-derived stem cells	ADSC differentiation into osteoblasts and adipocytes	Changes in the Raman spectra in the hydroxyapatite, collagen and carbonate chemical shifts after osteogenic differentiation; Raman peaks from lipids/proteins are sharper after adipogenic differentiation

Tan *et al.* (2012) **[48]**	Human embryonic stem cells & Human induced pluripotent stem cells	Differences between embryonic stem cells and induced pluripotent stem cells	Very similar Raman spectra, with small changes in the glycogen bands
Pascut *et al.* (2013) **[46]**	Human embryonic stem cells	Embryonic stem cell differentiation into cardiomyocytes	Changes in the Raman spectra of carbohydrate and lipid chemical shifts, increasing during differentiation process
Hung *et al.* (2013) **[39]**	Human skeletal stem cells	SSC differentiation into osteoblasts	Changes in the spectra in the octacalcium phosphate, ß-tricalcium phosphate and hydroxyapatite Raman shifts, able to detect the extent of maturation during osteogenic differentiation
Ichimura *et al.* (2014) **[42]**	Murine embryonic stem cells	Spontaneous differentiation of embryonic stem cells	Differences between Raman spectra of embryonic stem cells before and after spontaneous differentiation
James *et al.* (2015) **[51]**	Human skeletal stem cells	Analysis of functional markers in SSCs using immortalised SSC clonal lines	Different SSC clones were identified by Raman spectroscopy, presenting the same biomolecular profile as human SSC fractions
Ojansivu *et al.* (2015) **[53]**	Human adipose-derived stem cells	ADSC differentiation into osteoblasts, using different bioactive glasses	Similarities in the hydroxyapatite, octacalcium and ß-tricalcium phosphate Raman chemical shifts between different cell culture conditions
Mitchell *et al.* (2015) **[55]**	Human adipose-derived stem cells	ADSC differentiation into adipocytes	Characterisation of ADSC differentiation into adipocytes at early stages of differentiation

In 2009, Chiang *et al.* [49] studied osteogenic differentiation of MSCs applying Raman spectroscopy, with the purpose to monitor the production of hydroxyapatite throughout the osteogenic process. Chiang and colleagues found changes in the hydroxyapatite characteristic 'chemical' shift, over a period of 7-21 days following the initiation of differentiation. The state of differentiation of MSCs was confirmed by the use of alizarin red S staining for calcium. Chiang *et al.* also detailed a novel marker in MSC-derived osteoblasts by monitoring hydroxyapatite with Raman spectroscopy, providing the first indication that this technique could provide a promising tool for the study of skeletal tissue development. Downes *et al.* [24] also induced MSC osteogenic

differentiation for 7 days, and observed characteristic peaks in the spectra of osteoblasts related to phosphate in hydroxyapatite, collagen, and carbonate.

Similar approaches were used, where SSCs derived from human bone marrow, and subsequent differentiation into osteoblasts, were characterised and monitored [39, 52]. For example, McManus *et al.* [52] used Raman spectroscopy as a biochemical characterisation tool for SSC differentiation into osteoblasts, and compared the results with immunocytochemistry and qPCR analysis. McManus *et al.* determined carbonate-to-phosphate and mineral-to-matrix ratios using specific peaks in Raman spectra at different stages of osteogenic development, and observed an increase of the two ratios with time. Hung's research group identified new spectral markers for osteogenic differentiation in SSCs [39]. In this case, the characteristic chemical shift of octacalcium phosphate was present before differentiation, and the peak decreased throughout the assay period. In contrast, the hydroxyapatite signal increased during SSC differentiation into osteoblasts, and, in addition, a new peak belonging to the ß-tricalcium phosphate appeared following differentiation. Hung *et al.* further corroborated their results using histochemical and gene expression analyses.

Other groups have reported on the use of ADSCs for skeletal regeneration and their characterisation by Raman spectroscopy [24, 53]. Downes *et al.* [56] differentiated ADSCs into osteoblasts and adipocytes, and characterised the different populations using Raman spectroscopy. Similar to Hung's work [39], Ojansivu *et al.* [53] recently used octacalcium phosphate, hydroxyapatite and ß-tricalcium phosphate as specific markers for osteogenic differentiation, in order to compare culture conditions of ADSCs with different bioactive glasses. More recently, Mitchell *et al.* [55] demonstrated that Raman spectroscopy can be used to detect biochemical changes associated with adipogenic differentiation of ADSCs in a non-invasive and aseptic manner. Mitchell and colleagues were able to monitor the adipogenic differentiation of live ADSCs during 14 days and found significant differences from day 7.

An interesting possible application of Raman spectroscopy in SSC research, is the identification of different single-cell-derived clones, which could guide the search for new strategies to analyse the differentiation potential of SSCs, or even SSC isolation from human bone marrow. James *et al.* [51] studied distinct subtypes of human bone marrow stromal cells, and Raman spectroscopy was applied to identify the molecular fingerprint of the stromal cell subtypes together with the biomolecular profile of human bone marrow CD317 positive fractions. Peak intensity ratios were obtained, and the main difference in the Raman shift was found at 1088.6 cm^{-1}, which is related to the

symmetric phosphate stretch of the DNA backbone, indicating a fundamental difference in the DNA of the stromal cell subtypes.

Raman spectroscopic analysis is frequently applied in conjunction with multivariate statistical analysis, for example principal component analysis and hierarchical clustering analysis [43, 50, 52], due to the significant amount of chemical information embedded in Raman spectra. These methods provide an important approach to extract information on different constituents which exist in varying proportions in a heterogeneous sample such as bone. In addition, a large amount of spectral data can be generated from a tissue map or from different cell populations (healthy *versus* diseased, etc.). Identification of compositional changes, classification and quantification of concentrations necessitate the use of such statistical methods as has been shown in several studies with stem cells [45, 47, 52], and other diseases such as cancer [57]. Indeed, multivariate statistical methods for spectra analysis have contributed to the increase in Raman spectroscopy applications in the examination of living cells, and could be a helpful and vital tool for the comparison of biological samples.

While Raman spectroscopy provides a powerful tool for characterisation, the efficiency of Raman scattering is extremely small (approximately 1 in 10^7 scattered photons [58]). Thus for imaging Raman scattering is rather limited as acquisition times per pixel can be up to several seconds. In contrast, the use of alternative Raman-based techniques that can significantly boost and enhance Raman signal levels, such as coherent anti-Stokes Raman scattering (CARS), offer exciting alternatives and are detailed below.

2.3 Coherent anti-Stokes Raman scattering

CARS occurs when a target molecule is irradiated using two laser beams simultaneously at different frequencies, a pump beam ω_{Pump}, and a Stokes beam ω_{Stokes} (Figure 2.4) [59]. When the difference between the pump beam (higher frequency) and the Stokes beam (lower frequency) equals the vibrational frequency of the target bond of the molecule, a CARS signal is generated [32, 33, 60, 61], with an angular frequency equal to $\omega_{CARS} = 2\ \omega_{Pump} - \omega_{Stokes}$.

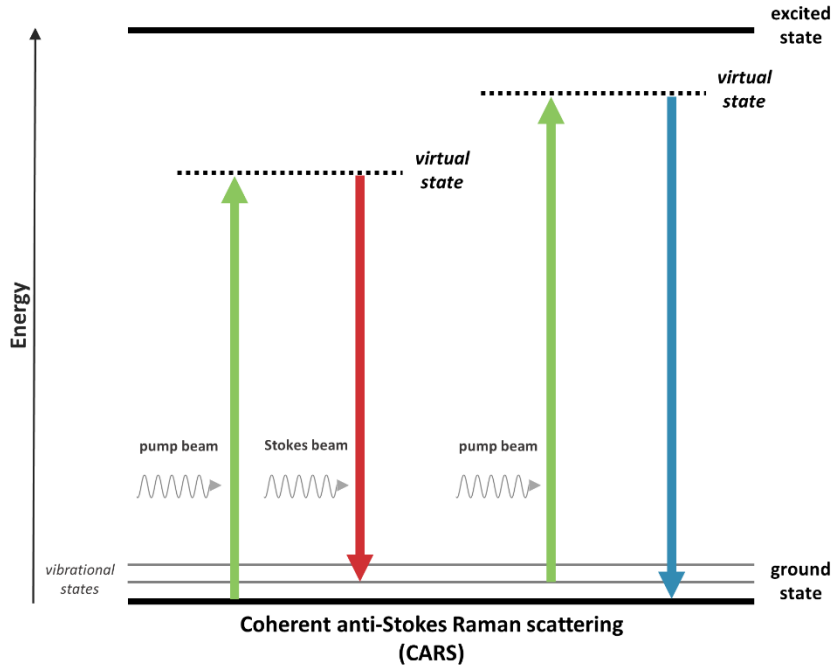

Figure 2.4 – Schematic diagram of the energy transitions involved in coherent anti-Stokes Raman scattering (CARS). In CARS, molecular vibrational modes are coherently populated through optical pumping. When the energy difference between the pump beam (higher frequency) and the Stokes beam (lower frequency) equals a particular molecular vibration of the target, a CARS signal is generated [34].

In contrast to spontaneous Raman scattering, where approximately one in ten million photons is scattered inelastically, CARS uses a four-wave non-linear process to enhance the Raman signal [58, 62]. This third-order process, which generates directional blue-shifted light (anti-Stokes) on the interaction of three photons at two different frequencies, is significantly stronger than spontaneous Raman as there is induced vibrational coherence. CARS is a chemically selective process, where ω_{Pump} and ω_{Stokes} can be tuned to equal the desired vibrational mode, causing all molecular polarizations to oscillate coherently and generate a resonant, strongly enhanced signal [32, 61].

In CARS microscopy, the temporally and spatially overlapped pump and Stokes laser beams are tightly focused into a sample. Since CARS signal has quadratic dependence on the number of oscillators, or Raman vibration modes, intense signals can be obtained in small volumes for high concentrations of vibrational oscillators [62, 63]. Considering CARS is a third-order non-linear process, sufficient pulse energies are required to ensure high conversion efficiency. CARS signal intensity can be enhanced by increasing the pulse energy and lowering the repetition rate. However, although femtosecond lasers have higher pulse energies, femtosecond lasers are not ideal for CARS microscopy as the laser spectral width is broader than Raman bandwidths.

Picosecond lasers have been successfully applied for CARS imaging, offering a more efficient process and high-speed imaging acquisition [63].

CARS is a multiphoton process with no net deposition of energy within the molecule (as illustrated in Figure 2.4), and is typically carried out with near-infrared laser sources. Besides being non-invasive, non-destructive and label-free, CARS provides relevant benefits over other imaging techniques: (i) the sample photo-damage is minimized, as no net energy is transferred to the sample [60], (ii) CARS provides inherent three-dimensional sectioning ability and video-rate imaging due to the nonlinear multiphoton nature of CARS process [31, 60, 64, 65], which is of paramount importance for studying cells or tissues, and (iii) fluorescence does not interfere in CARS, as anti-Stokes Raman scattering occurs at a different (blue-shifted) wavelength from fluorescence [32, 61].

2.3.1 Characterisation of SSCs using CARS imaging

CARS microscopy has been applied in the imaging of living cells and *ex vivo* tissues, using diverse vibrational contrasts such as for DNA, lipids and proteins [9, 66-68]. The abundance and the essential role of lipids in the human body, combined with the fact that lipids have a strong CH_2 and CH_3 stretching vibration signals at 2845 cm^{-1} and 2935 cm^{-1} [31, 68, 69], respectively, have made lipids the target of choice for demonstrating CARS applications. CARS applications in cell studies are being expanded – for instance, in order to develop an adipose-tumour epithelial cell co-culture system designed to reproduce the *in vivo* mammary environment. Thus, Salameh *et al.* [70] required a non-destructive and non-invasive technique to access the viability of adipocytes in co-culture. In this study, CARS analysis demonstrated the sustained viability of adipocytes, and an *ex vivo* co-culture model system to evaluate stromal-epithelial interactions in breast cancer was established. Another example is the application of CARS to study the effect of chemotherapeutic drugs in colon tumour cells. As demonstrated by Steuwe *et al.* [62], CARS proved to be a useful tool to rapidly image the subcellular accumulation of lipids in cancer cells undergoing cell death induced by different chemotherapeutic drugs.

The last few years have seen emergent data on *in vitro* cell studies for skeletal regeneration using CARS imaging (summarised in Table 2.2). One of the first examples, in 2007 by Konorov *et al.* [71], used CARS microscopy to analyse murine embryonic stem cells. Although image quality did not allow the identification of individual cells, this approach provided a first step towards the use of CARS imaging in stem cell research. The following year, Schie *et al.* induced and characterised MSC differentiation

into adipocytes, which is commonly assessed by identifying the development of lipid droplets. As the CARS signal for lipids is particularly strong, Schie and colleagues successfully imaged the lipid droplets after 21 days of adipogenic differentiation [72].

Different research groups have worked with ADSCs and monitored cell differentiation using CARS microscopy. Jo *et al.* [73] selectively imaged lipid droplets in high contrast in differentiated adipocytes, and it was possible to observe a chronological differentiation of ADSCs, comparing Oil red O staining with CARS images. In turn, Downes *et al.* [24] not only used CARS microscopy to characterise adipocytes, but also tried to establish the use of CARS to image osteoblasts. By imaging at the Raman frequency of hydroxyapatite (960 cm^{-1}), Downes obtained preliminary results with some vibrational contrast although with limited resolution.

Most CARS imaging applications map cellular components at a single vibration frequency and do not have the same chemical selectivity as Raman spectroscopy. Broadband or hyperspectral CARS imaging can overcome this limitation – the hyperspectral CARS setup provides CARS images at several vibrational frequencies and generates the corresponding spectra as in Raman spectroscopy. Di Napoli *et al.* [74] recently reported a comparison between CARS and broadband hyperspectral CARS imaging. After inducing adipogenesis in human ADSCs, CARS provided a qualitative contrast imaging while broadband hyperspectral CARS was used to determine the concentration of unsaturated lipids.

Undoubtedly, CARS imaging has emerged as an important alternative imaging technique. The combination of CARS microscopy with complementary imaging techniques, such as with second harmonic generation (SHG) and two-photon excited auto-fluorescence (TPEAF) imaging, is possible with the current lasers available. The association of CARS microscopy with TPEAF and/or SHG can be highly advantageous and offer the potential to inform the development of SSCs.

Table 2.2 – Coherent anti-Stokes Raman scattering (CARS) imaging applications in stem cells. References are ordered chronologically and by cell type.

Reference (year)	Cell type	Study	Main findings
Konorov *et al.* (2007) **[71]**	Murine embryonic stem cells	Distinguish differentiated and undifferentiated embryonic stem cells	Preliminary images of embryonic stem cells; Need improvements in spatial resolution and image contrast
Schie *et al.* (2008) **[72]**	Human mesenchymal stem cells	MSC differentiation into adipocytes	Lipid droplets with high CARS contrast in 21-days differentiated adipocytes
Jo *et al.* (2011) **[73]**	Human adipose-derived stem cells	ADSC differentiation into adipocytes	Characterisation of ADSC differentiation into adipocytes; Lipid droplets with high CARS contrast in differentiated adipocytes
Downes *et al.* (2011) **[24]**	Human adipose-derived stem cells	ADSC differentiation into osteoblasts and adipocytes	Preliminary CARS imaging of differentiated osteoblasts, with frequency tuned to hydroxyapatite (960 cm^{-1}); Lipid droplets with high CARS contrast in differentiated adipocytes
Mouras *at al.* (2012) **[75]**	Human adipose-derived stem cells	ADSC differentiation into osteoblasts and adipocytes	Collagen fibres detected using SHG, and osteoblasts imaged using CARS and two-photon excitation fluorescence Lipid droplets with high CARS contrast in differentiated adipocytes
Mortati *et al.* (2012) **[76]**	Human skeletal stem cells	Collagen production of SSCs in fibrin hydrogel scaffolds	Collagen fibres of SSCs in fibrin hydrogel scaffolds were imaged using CARS and SHG
Di Napoli *et al.* (2014) **[74]**	Human adipose-derived stem cells	ADSC differentiation into adipocytes	Lipid droplets with high contrast in adipocytes, comparing standard CARS and broadband hyperspectral CARS imaging; Hyperspectral CARS was more quantitative than CARS due to non-linear behaviour

2.4 Multimodal imaging: combining CARS microscopy with SHG and TPEAF

Similar to CARS microscopy, SHG and TPEAF are nonlinear imaging modalities that can typically be carried out with the same laser excitation sources, thus allowing a multimodal read-out. Both SHG and two-photon excitation are second-order processes (Figure 2.5), in contrast to CARS (third-order process).

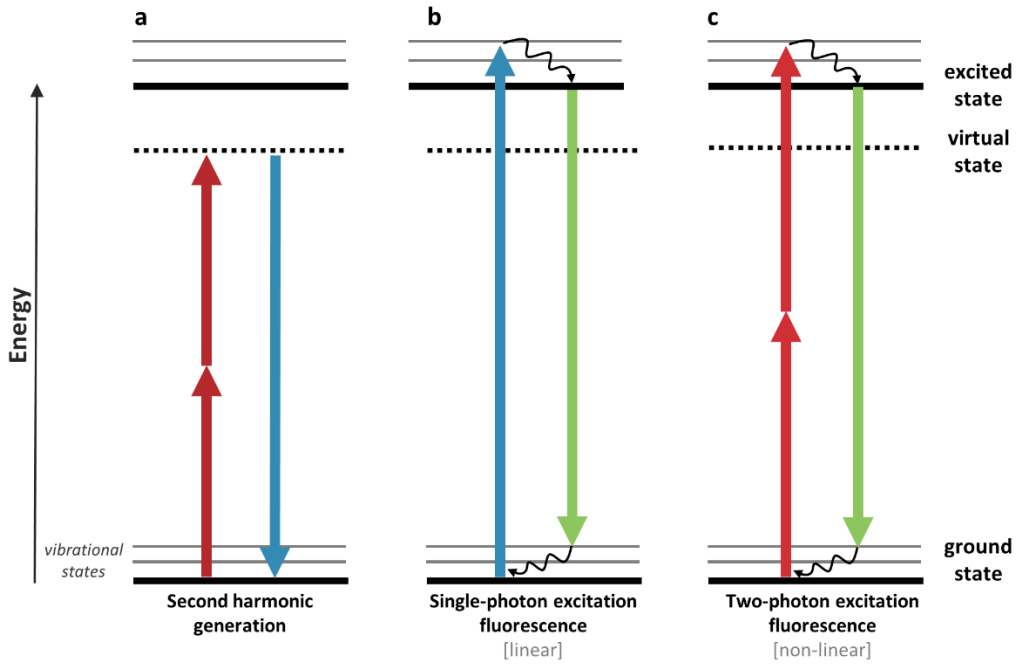

Figure 2.5 – Schematic diagram of the energy transitions involved in second harmonic generation (SHG), single-photon excitation fluorescence, and two-photon excitation fluorescence. In SHG, two lower energy photons are combined to generate a photon with exactly twice the incident frequency (a). Fluorescence involves real energy transition of electrons – in single-photon excitation (linear process), a fluorophore is excited from the electronic ground state to an excited state by a single photon of shorter wavelength than the emission photon (b). The same excitation process can be generated by the simultaneous absorption of two less energetic photons (non-linear process) – in two-photon excitation, two identical excitation photos are combined to generate an emission photon with shorter wavelength (c) [77, 78].

SHG is a second-order coherent process in which non-centrosymmetric structures, *i.e.* structures lacking a centre of symmetry, combine two lower energy photons from an excitation source to generate photons with exactly twice the incident frequency (Figure 2.5a) [77, 79]. SHG microscopy is promising for live cell or tissue imaging, as SHG does not involve excitation of an electronic resonance in molecules, leading to reduced phototoxicity effects. Moreover, SHG has been shown to occur in numerous organised biomolecular structures [77, 80]; examples of intrinsic SHG signal from biological samples include axonal microtubules [81], sarcomeric myosin [82], and collagen fibres [77].

Type I and Type II collagen have a hierarchy of non-centrosymmetric structures within each fibril and both form aligned striated fibres creating a super-structure (high degree of crystallinity) resulting in high SHG activity. In contrast, Type IV collagen has no fibrillary structure and consequently the SHG signal generated is insufficient for imaging [83-85]. For skeletal tissue applications, Type II collagen is a principal component of cartilage and represents more than 90% of the collagen in articular

cartilage extracellular matrix [86-88]. Since SHG has the established ability to directly (in the absence of labels) visualise collagen fibres, SHG is an ideal modality to provide comprehensive structural information on their arrangement in cartilage tissue. Very recently, SHG measurements in human prostate biopsies allowed a quantitative analysis of the collagen fibre alignment in prostate cancer [89], and in mouse joint samples SHG enabled the discrimination of cartilaginous and osseous tissues [90]. Other techniques, namely Raman spectroscopy imaging, are also emerging as powerful tools to measure the distribution and organisation of extracellular matrix constituents in cartilage [91].

In addition to CARS and SHG, TPEAF imaging offers another label-free modality to interrogate cellular composition and tissue development, providing further complementary information [92-95]. While SHG and CARS are coherent and directional processes, two-photon excitation fluorescence is a non-coherent and isotropic process. Although this process involves real energy transition of electrons, two-photon excitation differs from single-photon excitation fluorescence, where the excitation wavelength is shorter than the emission wavelength (Figure 2.5b), as two identical excitation photons are combined to generate an emission photon with shorter wavelength (Figure 2.5c). Since near-infrared excitation is used, two-photon excitation fluorescence has reduced phototoxicity/photodamage compared to single-photon fluorescence microscopy [93, 94].

Flavin adenine dinucleotide (FAD), a redox co-factor associated with mitochondria, is involved in redox reactions in living cells, as well as several other cellular pathways including biosynthetic processes. These co-enzymes contribute significantly to the cellular autofluorescence. Consequently TPEAF enables non-destructive imaging of living cells and tissues without the interference and, crucially, toxicity of exogenous dyes [93, 96]. The use of TPEAF has enabled characterisation of cell morphology and proliferation [97] and the ability to monitor cellular metabolic activity [97], including imaging cells undergoing osteogenesis and chondrogenesis [98].

Mortati *et al.* [76] followed collagen production in living SSCs within a fibrin hydrogel scaffold in a 3D culture system using SHG and CARS, clearly demonstrating the potential of multimodal CARS imaging. Hofemeier *et al.* imaged human mastoid cortex samples using SHG and CARS microscopy. The tissue samples displayed a strong CARS signal for calcium hydroxyapatite. The multimodal system used in this study provided a promising approach to determine the biomineralization of calcium hydroxyapatite and to simultaneously detect collagen in neural crest-derived stem cells [99]. CARS imaging combined with SHG and TPEAF was also applied by Mouras *et al.* to assess ADSC differentiation into adipocytes and osteoblasts [75, 100], and by

Mansfield *et al.* to investigate the elastin fibre network in healthy equine articular cartilage samples from the metacarpophalangeal joint [101].

2.5 Prospects for label-free imaging in SSC research

The studies discussed here demonstrate the potential of label-free techniques for enhanced characterisation of SSC differentiation in a non-invasive and non-destructive way, as neither sample preparation nor dyes/labels and other imaging contrast agents are required.

Raman spectroscopy has enjoyed considerable exploitation in medical diagnostics (reviewed in Kong *et al.* [102]). The translation of Raman spectroscopy from bench to clinic is currently in progress, and considerable studies are directed towards the development of optical fibre Raman probes for endoscopic applications [103]. One exciting example is the intraoperative probe created by Leblond *et al.* (using optical fibres and Raman spectroscopy) for detecting cancer cells during brain surgery [104, 105]. Frequently, it is difficult or even impossible to distinguish cancer from non-cancer brain tissue; consequently, after surgery, malignant cells remain in the brain leading to recurrence. This probe accurately identifies invasive cancer cells in the brain, based on Raman signal, guiding the surgeon in real time in the operating room. A related development is the incorporation of a fibre optic Raman probe in a hypodermic needle, in order to achieve subcutaneous tissue measurements for *in vivo* diagnostics [106]. This non-invasive probe has huge potential for evaluating bone composition through the skin. Buckley *et al.* have applied spatially offset Raman spectroscopy, also known as SORS, to detect a compositional abnormality in the bones of a patient suffering from osteogenesis imperfect, a genetic bone disorder that affects Type I collagen [107]. The developments herein discussed are being followed by clinical trials to validate the use of non-invasive Raman spectroscopy probes in the clinic for objective diagnostics, with the aim to improve patient outcomes and extend patient survival time.

As previously discussed in this thesis, in spontaneous Raman there are few inelastically scattered photons, resulting in weak Raman signal [66, 67, 108, 109]. In order to circumvent this, Raman systems need to be optimised to provide more sensitive instruments, including more powerful detectors and advanced algorithms to enhance signal to noise ratio. However, in CARS microscopy the Raman signal is enhanced, becoming more suitable for real-time imaging applications. For multimodal CARS imaging to be used as a routine technique several technological hurdles still need to be overcome.

The majority of CARS applications are performed imaging at a single vibrational frequency, and to date only a couple of biomolecules are typically visualised using CARS microscopy (including lipids and proteins). Furthermore, CARS, SHG and TPEAF still cannot provide the simplicity and efficiency offered by many of the established characterisation techniques used in skeletal regeneration. Instrumentation needs to be user friendly and of a size compatible with clinical practices [77]. Acknowledgement of the relative advantages/disadvantages and current challenges facing multimodal CARS imaging will provide the step change in methodology to design a label-free technique to monitor the differentiation of SSCs in their natural state.

In summary, the label-free, non-destructive and non-invasive nature of multimodal CARS microscopy offer an exciting alternative to dynamically monitor SSC development during skeletal regeneration, with widespread potential in other hard and soft tissues.

This thesis aims to investigate SSC differentiation during skeletal regeneration, and to engineer strategies to generate skeletal tissue and to temporally evaluate SSC development using multimodal and label-free imaging approaches. The next chapters of this thesis explore the potential of label-free imaging techniques, namely CARS, SHG and TPEAF, with the purpose to establish a novel non-invasive and non-destructive multimodal imaging platform to monitor SSC differentiation and assess skeletal tissue development.

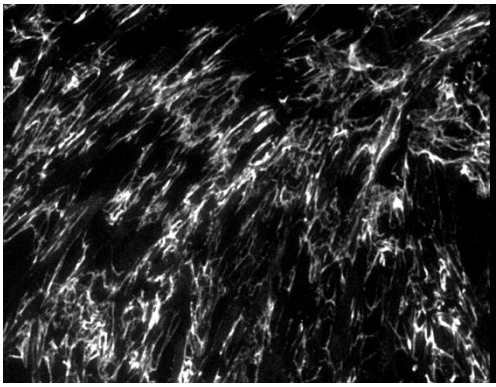

3

EXPERIMENTAL SECTION

Chapter 3 provides detailed descriptions of methodologies used in Chapters 4-6, to avoid redundancies between individual chapters. Methods include cell culture techniques, in vitro differentiation assays, molecular biology methods, histological processing and staining protocols, Raman spectroscopy methods, non-linear imaging instrumentation and methodology, image processing and data analysis. Optimisation of the laboratory procedures was also included in this chapter to provide for a more comprehensive perspective.

3.1 Materials

Alpha minimum essential medium with deoxyribonucleotides, ribonucleotides and L-glutamine (α-MEM), Dulbecco's modified Eagle medium with glucose and L-glutamine (DMEM), fetal calf serum (FCS), Dulbecco's phosphate buffered saline (PBS), and 0.025 % trypsin-EDTA (w/v) solution with 0.05 % glucose were purchased from Lonza (Switzerland). CellTracker™ Green CMFDA, Dulbecco's modified Eagle medium: nutrient mixture F-12 (DMEM/F12), dimethylformamide, and ethidium homodimer-1 were supplied from Thermo Fisher Scientific (USA). Bovine serum albumin (BSA) was obtained from GE Healthcare (USA). Collagenase B was purchased from Roche (Switzerland). Lymphoprep™ was supplied from Stem Cell Technologies (Canada). Transforming growth factor beta 3 (TGF-ß3) was purchased from PeproTech (UK). Anti-mouse IgM microbeads were supplied from Miltenyi Biotec (Germany). Anti-collagen Type I primary antibody, rabbit IgG, was a kind gift from Dr Larry Fisher (National Institutes of Health), and anti-collagen Type II primary antibody, rabbit IgG, was purchased from Calbiochem (Merck,Millipore, Germany). Acetate buffer, acetic acid glacial, 3 amino-9-ethyl-carbazole (AEC), alcian blue 8GX, ascorbate-2-phosphate, ß-mercaptoethanol, biotinylated goat anti-rabbit secondary antibody, calcium chloride, collagenase IV, dexamethasone, dimethyl sulfoxide (DMSO), DPX mountant for histology, ethanol, formaldehyde, ethylenediaminetetraacetic acid (EDTA), ExtrAvidin−Peroxidase, hyaluronidase, hydrochloric acid, hydrogen peroxide solution, human serum AB, 3-isobutyl-1-methylxanthine (IBMX), isopropanol, insulin-transferrin-selenium (ITS) liquid media supplement 100x, molybdophosphoric acid, Oil red O, penicillin-streptomycin (100 U mL^{-1} penicillin and 100 mg mL^{-1} streptomycin), picric acid, rosiglitazone, sirius red F3B, Tween®20, Weigert's haematoxylin constituents, and oligonucleotide primers were supplied by Sigma-Aldrich (USA). Histo-Clear and hydromount were purchased from National Diagnostics (UK).

3.2 Cell Culture

All cell culture procedures were performed using laminar flow Class II biological safety cabinets. All cells were maintained in a humidified chamber at 37 °C and 5 % CO_2.

3.2.1 STRO-1 monoclonal antibody

The enrichment of SSCs from human bone marrow samples can be achieved by immuno-magnetic separation of cells labelled with microbeads against a specific cell surface marker. STRO-1, which was recently described to bind to heat shock cognate

70 (HSC70/*HSPA8*) on the surface of approximately 10 % of human bone marrow mononuclear cells [110], is one of the most widely used monoclonal antibodies for enrichment of SSCs [111-114].

STRO-1 monoclonal antibody IgM was derived from a mouse hybridoma cell line (re-derived from an original donation provided by Dr Jon N. Beresford, University of Bath), using a CELLLine Classic Bioreactor CL350 (Scientific Laboratory Supplies, UK). The bioreactor is based on a two-compartment technology (Figure 3.1), with a 10 kDa semi-permeable membrane separating a medium and a cell compartment. This membrane allows simultaneously a continuous diffusion of nutrients into the cell compartment and removal of cellular waste.

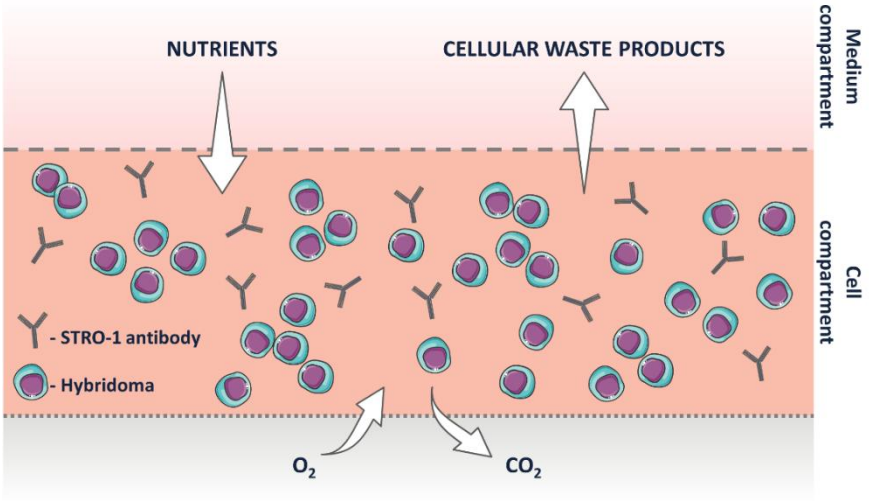

Figure 3.1 – Schematic of the two-cell compartment CELLLine Classic Bioreactor CL350 used for STRO-1 monoclonal antibody hybridoma.

Hybridoma cells (clone 10) were thawed, cultured and maintained in DMEM supplemented with 10 % FCS. Cell culture was maintained for 2 weeks, and media was replenished and changed every other day. Hybridoma cells were carefully inoculated into the bioreactor and plain DMEM was added to the medium compartment. Samples were routinely collected after 1 week of hybridoma culture in the bioreactor. For sample collection, fresh DMEM was replenished, a sample from the cell compartment was removed, and new hybridoma cells were added to the bioreactor. The collected sample from the bioreactor, containing cells and the produced STRO-1 monoclonal antibody, was centrifuged and the STRO-1 hybridoma supernatant was stored at -20 °C until ready to use.

3.2.2 Bone marrow preparation and STRO-1 enrichment

The enrichment of SSCs was achieved by immuno-magnetic separation of STRO-1 positive cells from human bone marrow mononuclear cells [113, 115, 116].

Bone marrow samples were collected following routine total hip arthroplasty surgery at Southampton General Hospital or Spire Southampton Hospital. Only tissue that would have been discarded was used, with approval of the Southampton and South West Hampshire Research Ethics Committee (194/99/1 & 210/01). Patient consent was obtained for every case.

The marrow samples were repeatedly washed with α-MEM and centrifuged, in order to collect the most of marrow cells. After cell extraction from bone marrow, the cell suspension was filtered using a 40 μm cell strainer to remove residual bone fragments and other unwanted tissue. The filtered cell suspension was carefully layered in Lymphoprep™, a density gradient medium. The cell suspension was then centrifuged (800 *g*, for 40 minutes at 18 °C), as the relative density of the Lymphoprep™ allows the isolation of mononuclear cells from the bone marrow cells through exploitation of the differences in cell density.

Bone marrow mononuclear cells (present at the interphase between medium and Lymphoprep™ after centrifugation) were carefully collected from the gradient and washed in α-MEM. The STRO-1 positive fraction was enriched by magnetic activated cell sorting (MACS), using the LS separation column and QuadroMACS™ magnetic field (Miltynei Biotec, Germany). Initially, cells were incubated with a blocking buffer (10 % human serum AB (v/v), 5 % FCS (v/v) and 1 % BSA (v/v) in α-MEM) for 30 minutes at 4 °C, to minimise non-specific antibody binding. After washing with MACS buffer (0.5 % BSA (v/v), 2 mM EDTA (v/v) in PBS), cells were incubated for 30 minutes at 4 °C with STRO-1 monoclonal antibody. Cells were washed with MACS buffer and re-suspended in anti-mouse IgM microbeads (20 μL per 10^7 cells) for an incubation of 15 minutes at 4 °C. Finally, after washing with MACS buffer, the cell suspension was run through LS MACS™ columns on a QuadroMACS™ for positive selection. The magnetically labelled STRO-1 positive cells were held in the column under the influence of the magnetic field, while the unlabelled STRO-1 negative cells were eluted by repeated washes of the column. STRO-1 positive fraction was collected by removing the column from the magnetic stand, and pressing a plunger through the column with MACS buffer.

The enriched SSC population was cultured in basal media (α-MEM supplemented with 10 % FCS (v/v) and 1 % penicillin-streptomycin (v/v)) at a cell density of $1x10^4$ cells cm^{-2}. After one week of culture, the non-adherent cells were washed away, and the media was replenished and changed every other day. Cells were harvested at passage 1 (typically 85 % confluence) using trypsin/EDTA, 3-4 weeks after enrichment.

3.2.3 Human articular cartilage dissection and chondrocyte isolation

Human articular cartilage was obtained following routine total hip arthroplasty surgery at Southampton General Hospital or Spire Southampton Hospital. Only tissue that would have been discarded was used, with approval of the Southampton and South West Hampshire Research Ethics Committee (194/99/1 & 210/01) following patient consent.

Each cartilage sample was cut into small segments and digested by sequential enzymatic treatment with: trypsin/EDTA for 30 minutes; 1 mg mL^{-1} of hyaluronidase in PBS for 15 minutes; and 1 mg mL^{-1} collagenase B in DMEM/F12 for 14 hours [117]. All incubations were performed at 37 °C, with gentle agitation. The human articular chondrocyte cell suspension was filtered through a 70 µm nylon mesh cell strainer, and cells were cultured in DMEM/F12 media supplemented with penicillin-streptomycin, 100 µM ascorbate-2-phosphate, 10 nM dexamethasone, 10 ng mL^{-1} TGFß3, and 1 µL mL^{-1} ITS, at a cell density of $1.5x10^4$ cells mL^{-1}.

3.2.4 Fetal sample isolation

Human fetal tissue were obtained following termination of pregnancy procedure and with informed patient consent according to guidelines issued by the Polkinghorne Report (ethical approval LREC 296100).

Fetal samples were isolated from the lower limbs at the end of Carnegie stage 23 (approximately 60 days post conception). Surrounding skeletal muscle and connective tissue were removed, and each sample was cut into small segments and digested overnight in collagenase B (1 mg mL^{-1} collagenase B in α-MEM) at 37 °C. The cell suspension was filtered through a 70 µm nylon mesh cell strainer, and cells were cultured in α-MEM supplemented with 10 % FCS (v/v) and penicillin-streptomycin. Cells were harvested at 85 % confluence using trypsin/EDTA for 5 minutes at 37 °C and cryopreserved at -80 °C in 10 % DMSO (v/v) in FCS. Derivation of fetal femur explant cultures was performed by Dr Emma Budd, from the Bone and Joint Research Group. Fetal skeletal cells were thawed and cultured in α-MEM supplemented with 10 % FCS (v/v) and penicillin-streptomycin before each experiment [118].

3.2.5 Adipogenic differentiation

For *in vitro* differentiation into adipocytes, human adult STRO-1 positive SSCs were seeded into 6-well cell culture plates at a density of $3x10^3$ cells cm^{-2} in α-MEM supplemented with 10 % FCS (v/v) and penicillin-streptomycin (basal media), and cultured for 6 days. Human fetal femur-derived skeletal cells were seeded at a density

of $1x10^3$ cells cm^{-2} in basal media and cultured for 3 days. Fresh adipogenic media (basal media supplemented with 100 nM dexamethasone, 0.5 mM IBMX, 3 µL mL^{-1} ITS and 1 µM rosiglitazone) was added to induce adipogenic differentiation. Cells treated with basal media served as control. Basal and adipogenic media was changed every 3-4 days.

3.2.6 Chondrogenic differentiation

Human fetal femur-derived skeletal cells were pre-treated with collagenase IV (200 mg mL^{-1} in serum-free α-MEM) for 30 minutes at 37 °C, and harvested using trypsin/EDTA for 5 minutes at 37 °C. Cells were centrifuged and re-suspended in 1 mL serum-free chondrogenic media (α-MEM supplemented with penicillin-streptomycin, 100 µM ascorbate-2-phosphate, 10 nM dexamethasone, 10 ng mL^{-1} TGF-ß3, and 1 µL mL^{-1} ITS) at a cell density of $3x10^5$ cells mL^{-1}. After a second centrifugation in a conical bottom tissue culture tube, the resulting cell pellet was maintained in culture for 21 days. Chondrogenic media was replenished every 2-3 days, and the pellet was regularly stirred within the media to ensure nutrient access to all sides, and to prevent the pellet from adhering to the walls of the tube [119]. The methodology used for human articular chondrocytes was identical with only substitution of DMEM/F12 media in place of α-MEM.

3.2.7 Gene expression analysis

3.2.7.1 RNA extraction

For experiments further described in Chapter 4, total RNA was isolated using the Qiagen RNeasy Plus Mini Kit (Qiagen, Netherlands), according to the manufacturer's instructions. Cells were lysed and homogenised in 600 µL buffer RTL Plus and stored at -80 °C. Sample lysates were thawed in ice, transferred to a gDNA eliminator spin column, and centrifuged for 1 minute at 8000 *g*. All centrifugations were performed at 18 °C. The column was discarded, and 600 µL 70 % ethanol (v/v) added to the flow-through. After mixing by pipetting, the mixed lysates were transferred to RNeasy spin columns and centrifuged for 1 minute at 8000 *g*. Flow-through was discarded, spin columns were washed with 700 µL buffer RW1 and centrifuged for 1 minute at 8000 *g*. After discarding the flow-through, the spin columns were washed twice in 500 µl buffer RPE, and centrifuged for 2 minutes at 8000 g. To remove any remaining buffer, spin columns were centrifuged for an extra 1 minute at 8000 *g*. The RNeasy spin columns were placed in fresh collection tubes, 30 µL RNase-free water added directly to the spin column membranes, and tubes centrifuged for 1 minute at 8000 *g*. The flow-through was collected and re-added directly to the spin column membrane, and centrifuged for 1 minute at 8000 *g*. Purified RNA samples were stored at -80 °C until further analysis.

For experiments detailed in Chapter 5 and Chapter 6, total RNA was isolated using the Bioline Isolate II RNA/DNA/Protein kit (Bioline, UK), according to the manufacturer's instructions. Cell pellets were disrupted and homogenised in 600 µL lysis buffer TX with 1 % ß-mercaptoethanol (v/v) by using a Ultra-Turrax handheld homogeniser, and stored at -80 °C. Sample lysates were thawed in ice, transferred to an Isolate II DNA column, and centrifuged for 1 minute at 14000 *g*. Flow-through was collected for total RNA purification, and 600 µL 100 % ethanol added. After mixing by pipetting, the mixed lysates were transferred to RNA columns and centrifuged for 1 minute at 3500 *g*. RNA columns were washed with 400 µL buffer W1 and centrifuged for 2 minutes at 14000 *g*. After adding 115 µL of DNase I buffer mix, columns were centrifuged for 1 minute at 14000 *g*. The flow-through was collected, and re-added directly to the spin column membranes for an incubation of 15 minutes at room temperature. RNA spin columns were washed twice with 400 µl of buffer W1, and centrifuged for 2 minutes at 14000 *g*. To remove any remaining buffer, RNA columns were centrifuged for further 2 minute at 14000 *g*. The RNA columns were placed in fresh collection tubes, 50 µL RNA elution buffer were added directly to the spin column membranes, and tubes centrifuged for 2 minutes at 200 *g*. The flow-through was collected and re-added directly to the spin column membrane, and centrifuged for 1 minute at 200 *g*. Purified RNA samples were stored at -80 °C until further analysis.

For each experiment, purified RNA samples were quantified using a Nanodrop ND-1000 UV-Vis spectrophotometer at 260 nm, and dilutions prepared to provide the same amount of RNA for each sample.

3.2.7.2 Reverse transcription

After RNA extraction (Chapter 4), cDNA synthesis was performed using the SuperScript® VILO™ cDNA Synthesis Kit (Invitrogen, USA), according to the manufacturer's instructions. The reaction was performed using 7 µL diluted sample, 2 µL 5X VILO™ Reaction Mix and 1 µL 10X SuperScript Enzyme Mix. The reaction conditions for the reverse transcription reaction included: i) initial incubation at 25 °C for 10 minutes, ii) reverse transcription incubation at 42 °C for 120 minutes, and iii) final incubation at 85 °C for 5 minutes.

For the experiments discussed in Chapter 5 and Chapter 6, cDNA synthesis was performed using TaqMan™ Reverse Transcription Reagents from Applied Biosystems™ (Thermo Fisher Scientific, USA), following the manufacturer's instructions. The reaction was performed using 7.7 µL diluted sample, 2 µL 10X TaqMan RT buffer, 4.4 µL 25 mM magnesium chloride, 4 µL dNTP mix, 1 µL random

hexamer, 0.4 µL RNase inhibitor, and 0.5 µL reverse transcriptase MultiScribe™. The reaction conditions for the reverse transcription reaction included: i) initial primer incubation at 25 °C for 10 minutes, ii) reverse transcription incubation at 48 °C for 30 minutes, and iii) reverse transcriptase inactivation at 95 °C for 5 minutes.

3.2.7.3 Reverse transcription quantitative polymerase chain reaction (RT-qPCR)

Relative quantification of gene expression was performed with RT-qPCR using an ABI Prism 7500 detection system (Applied Biosystems, USA). The primers used for RT-qPCR are shown in Table 3.1.

Table 3.1 – Primers used for reverse transcription quantitative polymerase chain reaction (RT-qPCR) analysis (F: forward and R: reverse).

Transcript	Symbol	Primer sequence (5'-3')
Aggrecan	*ACAN*	F: GACGGCTTCCACCAGTGT R: GTCTCCATAGCAGCCTTCC
Alkaline Phosphatase	*ALPL*	F: GGAACTCCTGACCCTTGACC R: TCCTGTTCAGCTCGTACTGC
Alpha-1 Type I Collagen	*COL1A1*	F: GAGTGCTGTCCCGTCTGC R: TTTCTTGGTCGGTGGGTG
Alpha-1 Type II Collagen	*COL2A1*	F: CCTGGTCCCCCTGGTCTTGG R: CATCAAATCCTCCAGCCATC
Alpha-1 Type X Collagen	*COL10A1*	F: CCCACTACCCAACACCAAGA R: GTGGACCAGGAGTACCTTGC
ß-actin	*ACTB*	F: GGCATCCTCACCCTGAAGTA R: AGGTGTGGTGCCAGATTTTC
Glyceraldehyde-3-Phosphate Dehydrogenase	*GADPH*	F: GACAGTCAGCCGCATCTTCTT R: TCCGTTGACTCCGACCTTCA
Peroxisome Proliferator Activated Receptor Gamma	*PPARG*	F: GGGCGATCTTGACAGGAAAG R: GGGGGGTGATGTGTTTGAACTTG
Fatty Acid Binding Protein 4	*FABP4*	F: TAGATGGGGGTGTCCTGGTA R: CGCATTCCACCACCAGTT
Transcription Factor SOX9	*SOX9*	F: CCCTTCAACCTCCCACACTA R: TGGTGGTCGGTGTAGTCGTA

All primers were designed and validated previously in-house, at the Bone and Joint Research Group, by Dr Rahul S Tare. For demonstration purposes, *ACTB* and *ACAN* primer efficiency was evaluated [120]. RT-qPCR was performed on a series of dilutions of a cDNA sample from STRO-1 positive SSCs (Figure 3.2).

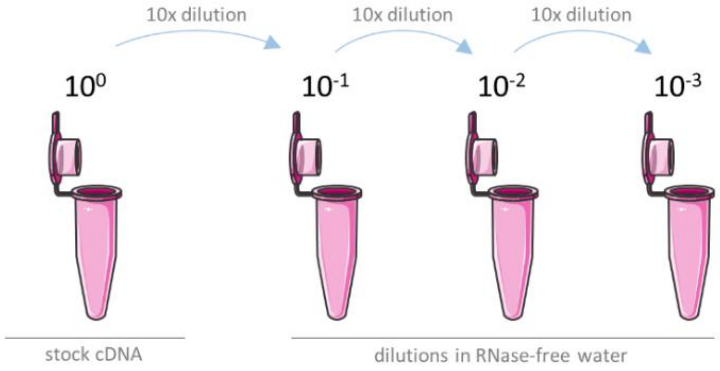

Figure 3.2 – Schematic of the serial dilutions of the cDNA template for primer validation and reverse transcription quantitative polymerase chain reaction (RT-qPCR) efficiency calculation.

Melt curve plots enable visualisation of the rate of change in normalised fluorescence throughout the course of the temperature ramp, and display the melt curve data for a single experiment (Figure 3.3). Each peak present within the melt curve plot corresponds to a maximum rate of change in fluorescence for a particular well. As there is only one characteristic peak present in each graph (Figure 3.3), this confirms the presence of one specific product of the RT-qPCR reaction and primers specificity. Non-specific amplification or contamination of the samples may cause unexpected peaks in the melt curve. Melting curves were always verified for all RT-qPCR experiments in this thesis.

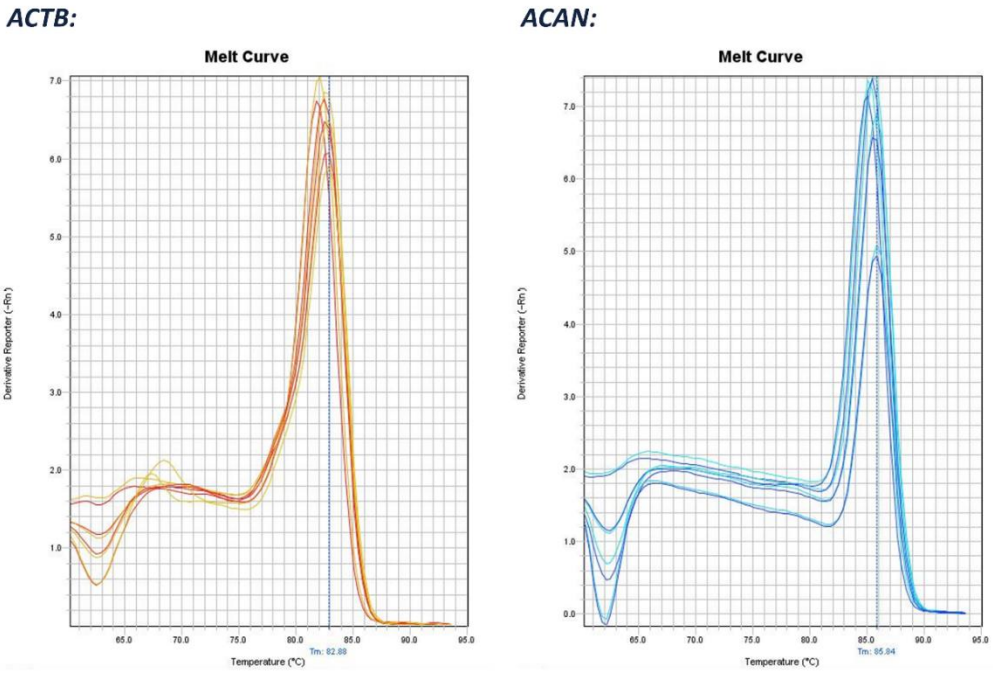

Figure 3.3 – Representative melt curve plots showing melting temperature values of *ACTB* and *ACAN* primers for reverse transcription quantitative polymerase chain reaction (RT-qPCR) primer validation.

The cycle threshold (Ct) values for each dilution were plotted to obtain a linear regression analysis equation (Figure 3.4). The slope of the standard curve indicates RT-qPCR efficiency, by using the formula $10^{-1/slope} - 1$. When efficiency is maximum (100 %), the fold increase will be 2 at each cycle, and indicates that polymerase enzyme is working at maximum capacity. The quantity of PCR product generated at each cycle decreases with decreasing efficiency, and the amplification plot is delayed. Ideally, primer efficiency should be between 90 %-110 % (theoretical values can exceed 100 % due to polymerase inhibition, as the efficiency plot is flatten out, resulting in a lower slope). Efficiency of *ACTB* and *ACAN* primers were estimated to be 106 % and 96 %, respectively (Figure 3.4).

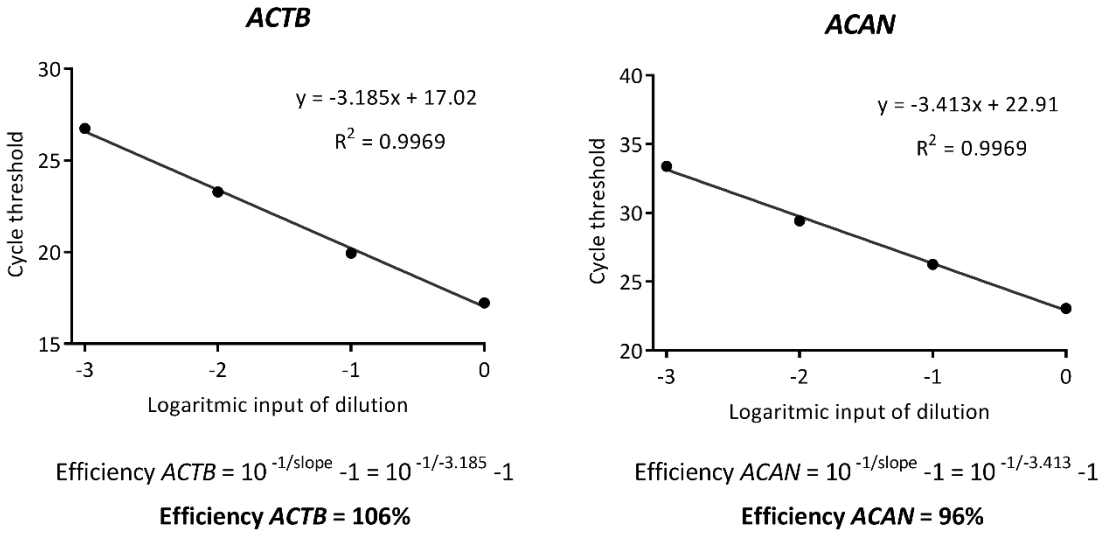

Figure 3.4 – Reverse transcription quantitative polymerase chain reaction (RT-qPCR) efficiency calculation for *ACTB* and *ACAN* primers. Efficiency of *ACTB* and *ACAN* primers were estimated to be 106 % and 96 %, respective, by using RT-qPCR cycle threshold (Ct) values.

RT-qPCR was performed combining the cDNA samples with the relevant primers and a RT-qPCR master mix, according to each experimental conditions. For experiment detailed in Chapter 4, a 20-µL reaction mixture was prepared per well, containing 1 µL of cDNA, 10 µL of Power SYBR Green PCR Master Mix (Thermo Fisher Scientific, USA) and 1 µM of each primer. For experiments detailed in Chapter 5, a 10-µL reaction mixture was prepared per well, containing 0.5 µL of cDNA, 5 µL of GoTaq qPCR Master Mix (Promega, USA) and 1 µM of each primer. For RT-qPCR experiments detailed in Chapter 6, a 20-µL reaction mixture was prepared per well, containing 2 µL of cDNA, 17.5 µL of GoTaq qPCR Master Mix and 0.375 µM of each primer. All reactions were performed in triplicate and included a negative control with no cDNA. Thermal cycler conditions were programmed with an initial activation step at 50 °C for 2 minutes and 95 °C for 10 minutes, followed by 40 cycles of 95 °C for 15 seconds and 60 °C for 1

minute. The melt curve stage was included with 95 °C for 15 seconds, 60 °C for 1 minute, 95 °C for 30 seconds, and finishing with 60 °C for 15 seconds. The relative quantification of gene expression was determined using the arithmetic formula $2^{-\Delta\Delta Ct}$, and all data were normalised to the housekeeping gene expression (*ACTB* for human adult STRO-1 positive SSCs and human fetal femur-derived skeletal cells, and *GADPH* for human articular chondrocytes) and compared to the expression values of each gene at day 0, set at 1.

3.2.8 Oil Red O

For Oil Red O staining, cells cultured in monolayer were washed with PBS and fixed in Baker's formal calcium solution, containing 1 % calcium chloride (w/v) and 4 % formaldehyde (v/v), for 25 minutes at room temperature. Following fixation, cells were rinsed with 60 % isopropanol (v/v), and stained using double-filtered Oil Red O solution for 15 minutes. To prepare the staining solution, a saturated Oil Red O solution in isopropanol was mixed with dH_2O, to a final ratio of 3:2. Cells were carefully washed three times in excess water, and images were captured using a Carl Zeiss Axiovert 200 phase contrast inverted microscope, AxioCam HR (colour) digital camera, and the software package AxioVision 4.7.0.0.

3.2.9 Histological analysis

3.2.9.1 Sample preparation and sectioning

Cell pellets were washed with PBS and fixed in 4 % formaldehyde (v/v) solution for 25 minutes at room temperature. Fixed samples were dehydrated by immersion through a series of ethanol and Histo-Clear washes – 50 % ethanol, 70 % ethanol, 90 % ethanol, 100 % ethanol, 100 % ethanol, 50:50 100 % ethanol: Histo-Clear, 100 % Histo-Clear, 100 % Histo-Clear, for 30 minutes each. The dehydrated samples were transferred to paraffin wax and incubated at 50 °C for 45 minutes, to ensure complete paraffin penetration of the sample. The paraffin was then replaced with fresh paraffin to fully embed the samples, and the paraffin block was stored at 4 °C. Embedded samples were sequentially sectioned with a thickness of 5 µm using a Microm HM330 D-6900 microtome (Heidelberg Instruments, Germany) and mounted on glass slides for histological assessment. Slides were dried at 37 °C for 3 hours, and stored at 4 °C.

3.2.9.2 Alcian blue/Sirius red staining

Samples mounted on glass slides were dewaxed following two incubations in Histo-Clear for 7 minutes, and rehydrated through a series of ethanol washes (100 %, 90 %, 70 % and 50 % ethanol), for 2 minutes each. Sections were stained with

haematoxylin. Equal volumes of Weigert's haematoxylin A solution (10 g L^{-1} haematoxylin in 100 % ethanol, left for a minimum of 4 weeks to mature) and B solution (6 g ferric chloride, 500 mL dH_2O, and 5 mL concentrated hydrochloric acid) were mixed, filtered through a paper filter and dripped directly onto the slides. Samples were subsequently incubated with the haematoxylin solution for 10 minutes, and rinsed in a running water bath for 10 minutes. After dipping three times in an acid/alcohol solution (1 % hydrochloric acid (v/v) in 70 % ethanol (v/v)), slides were rinsed in a running water bath for further 5 minutes. Sections were stained with Alcian blue 8GX (5 mg mL^{-1} in 1 % glacial acetic acid (v/v)) for 10 minutes, molybdophosphoric acid 1 % (w/v) for 10 minutes, and Sirius red F3B (10 mg mL^{-1} in 33 % picric acid (v/v) for 45 minutes. Slides were rinsed in a running water bath for 1 minute between each incubation. The sections were again dehydrated through a series of ethanol washes (50 %, 90 %, 100 % and 100 %), for 30 seconds each, and incubated twice in Histo-Clear for 30 seconds, prior to glass slide mounting using DPX mounting medium.

3.2.9.3 Immunohistochemistry staining

Samples mounted on glass slides were dewaxed following two incubations in Histo-Clear for 7 minutes, and rehydrated through a series of ethanol washes (100 %, 90 %, 70 % and 50 % ethanol), for 2 minutes each. Sections were covered with 3 % hydrogen peroxide (v/v) for 5 minutes at room temperature, to quench endogenous peroxidase activity. After washing in a running water bath, samples were incubated in hyaluronidase solution (0.8 mg mL^{-1} in 1 % BSA (w/v) in PBS) for 20 minutes at 37 °C in order to unmask the collagen fibres and render them accessible for immunostaining. Subsequently, samples were incubated with the blocking buffer (1 % BSA (w/v) in PBS) for 5 minutes at 4 °C, to block unspecific binding of antibodies. The primary antibody solutions (anti-collagen Type I, dilution 1:1000 in blocking buffer, and anti-collagen Type II, dilution 1:500 in blocking buffer), were added to the sections for an overnight incubation at 4 °C. Negative controls (omission of the primary antibody) were included in all immunohistochemistry procedures. Slides were rinsed in dH_2O and washed three times with 0.5 % Tween®20 (v/v) in PBS for 5 minutes. Biotinylated secondary antibody (dilution 1:100 in blocking buffer) was applied for 1 hour at 4 °C. Samples were rinsed gently in dH_2O and washed three times in Tween®20 for 5 minutes. ExtrAvidin-Peroxidase was added at a 1:50 dilution in blocking buffer for 30 minutes at room temperature. After rinsing the samples with dH_2O and three washes in Tween®20 for 5 minutes, sections were treated with AEC for 4 minutes until visualisation of a red-brown reaction product. The AEC solution was prepared by mixing 500 µL of stock solution (0.01 g AEC in 1250 µL dimethylformamide) with 9.5 µL acetate buffer (pH

5.0) and 5 µL 30 % hydrogen peroxidase (v/v). Slides were rinsed in a running water bath to terminate the reaction. All sections were counter-stained using Alcian blue 8GX for 60 seconds and mounted in hydromount mounting medium.

3.2.10 Raman spectroscopy

Raman measurements were performed on a Renishaw® InVia Raman microscope system, fitted with an upright Leica DM 2500-M bright field microscope. In this thesis, Raman spectra were obtained using a 633 nm laser. In essence, the laser beam enters the Raman system and is collimated and expanded. The beam reaches a dichroic beam splitter, and subsequently is focused by an objective and directed onto the sample. The objective used was a water dipping 20x magnification objective with 0.5 numerical aperture. Scattered light is backward collected by the same objective, and passes through the dichroic filter and a long pass edge filter to remove Rayleigh and anti-Stokes shifted scattering. A 1200 lines per mm grating diffracts the scattered Raman radiation into its constituent wavelengths, and is detected by a charge-coupled device camera. Raman spectra were obtained in combination with WiRE 3.4 software to control acquisition parameters and microscope settings. Before each experiment, an internal silicon reference was measured for spectral calibration and to test system performance.

For Raman spectra acquisition on monolayer cultures, cells were cultured on sterilised glass coverslips, washed with PBS and fixed in 4 % formaldehyde (v/v) solution for 25 minutes at room temperature. Cell pellets were washed with PBS and fixed in 4 % formaldehyde (v/v) solution for 30 minutes at room temperature. Following fixation, samples were washed and stored in PBS at 4 °C. For each spectrum, a minimum of 3 accumulations were collected, with an exposure time of 60 seconds and 6mW laser power at the sample.

After Raman spectra acquisition, data was processed using IRootLab, a MATLAB based toolbox for vibrational spectroscopy [121]. Baseline correction by polynomial fitting and wavelet de-noising were carried out in IRootlab. An example of Raman spectra processing is shown in Figure 3.5.

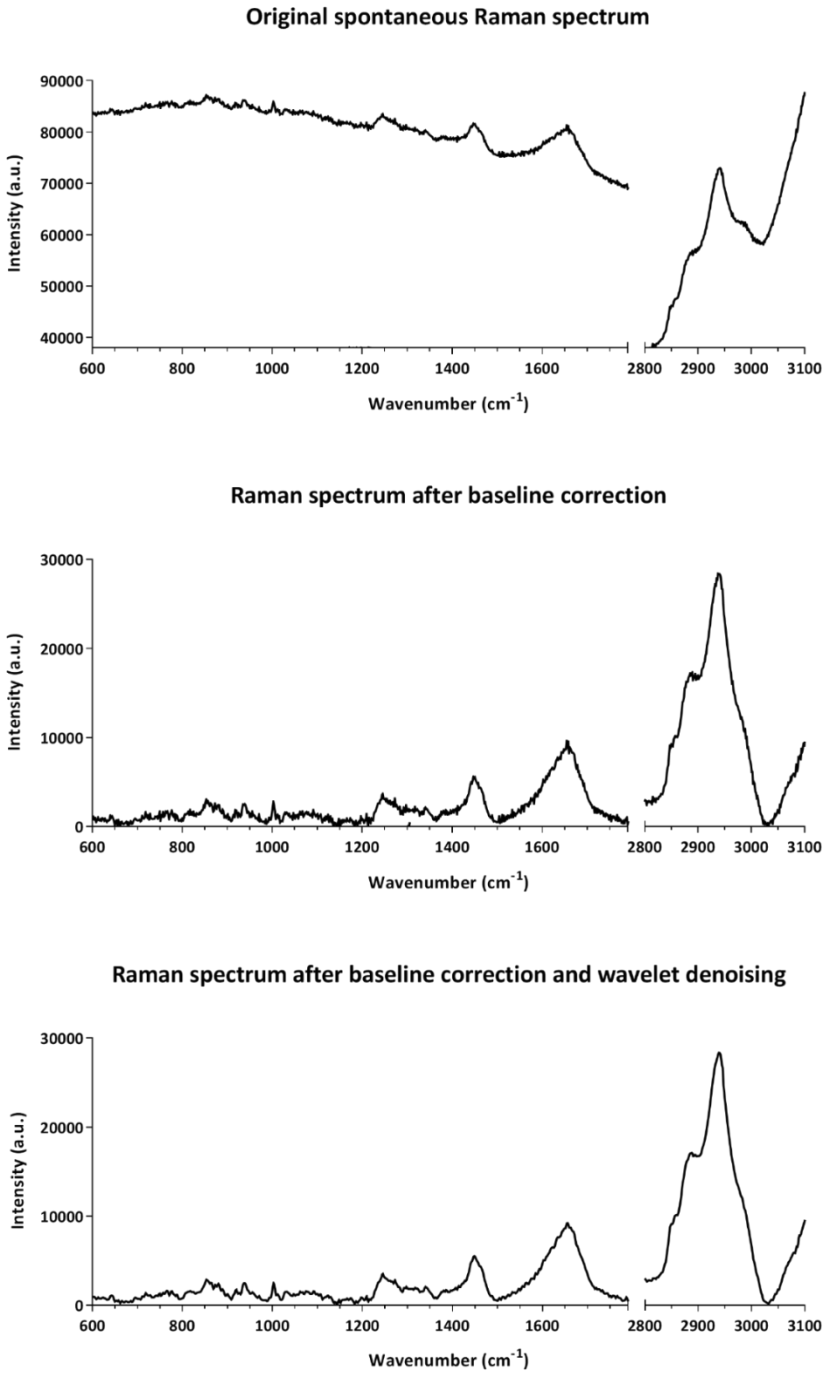

Figure 3.5 – Raman spectra processing steps: wavelet de-noising and baseline correction using IRootLab.

3.2.11 CARS imaging

For CARS imaging, discussed in Chapter 4, SSCs were cultured on sterilised glass coverslips. After culture for different time points, cells were washed with PBS and fixed in 4 % formaldehyde (v/v) solution for 30 minutes at room temperature. Cells were washed with excess PBS, and images were captured using a home-built CARS system as schematised in Figure 3.6.

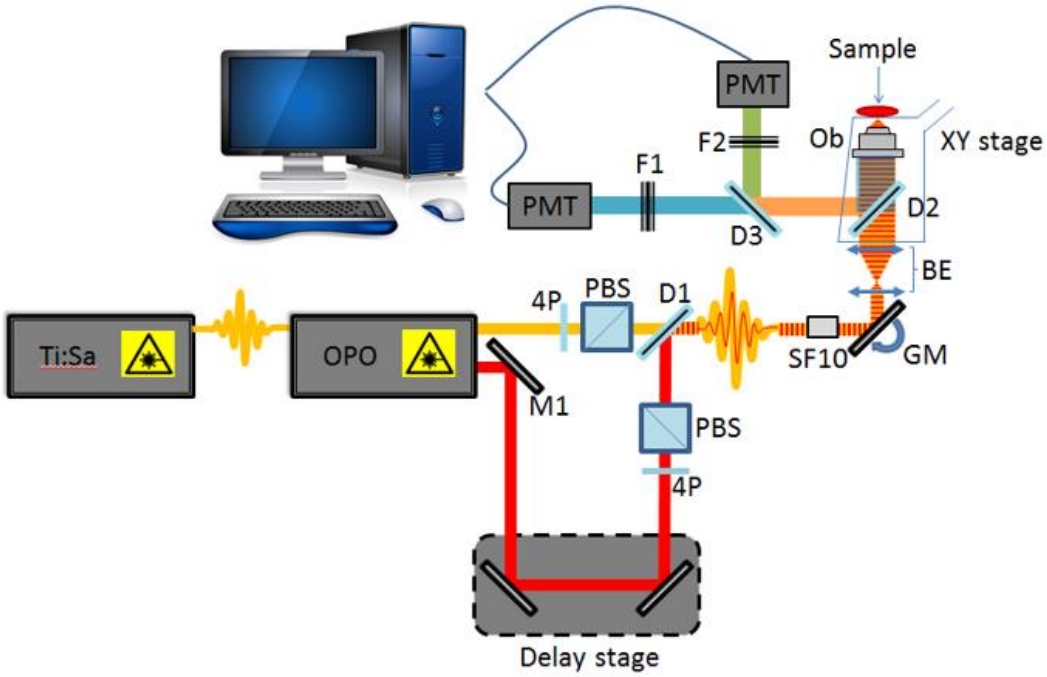

Figure 3.6 – Schematic of home-built femtosecond coherent anti-Stokes Raman scattering (CARS) imaging setup used for tracking adipogenic differentiation of human adult SSCs. OPO: optical parametric oscillator, PBS: polarizing beam splitter, PMT: photomultiplier, SF10: ultrafast laser dispersion compensating prism, BE: beam expander, Ob: objective, D: dichroic mirror, F: filter, M: mirror. 4P: half-wave plate, GM: galvanometer mirrors.

A Chameleon Ultra Titanium:Sapphire laser (Coherent, UK, 700-1000 nm, 100 fs, 80 MHz) was used to generate a beam which was then split into two. One beam was used as the pump beam, and the other beam served to drive an optical parametric oscillator (OPO) (APE Berlin, Germany) to generate the Stokes beam. Both beams were spectrally compressed (approximately 50 cm^{-1} spectral resolution), spatially and temporally combined and collinearly placed into an inverted microscope (Nikon Ti-U); the resulting epi-CARS signal (back-scattered) was detected. Epi-detection was used as this approach minimised the non-resonant background signal present during imaging. For imaging lipids in the cells, the CH stretch mode at 2845 cm^{-1} was targeted, using a pump beam wavelength of 835 nm and the OPO beam of 1097 nm. Lipids were visualised as bright areas on the images. Each sample was imaged using a 40x objective, with a 2x optical zoom using galvanometric scanning, and the acquisition time was 16 ms per line for a 512 x 512 pixel image. The total incident power on the sample was 30 mW, with 20 mW in the pump and 10 mW in the Stokes beam. Four images were taken from each coverslip (12 images for each time point).

3.2.12 SHG and TPEAF multimodal imaging

For simultaneous SHG and TPEAF imaging, on experiments presented in Chapter 5, sample sections at different time points were imaged using a home-built laser scanning microscope as schematised in Figure 3.7.

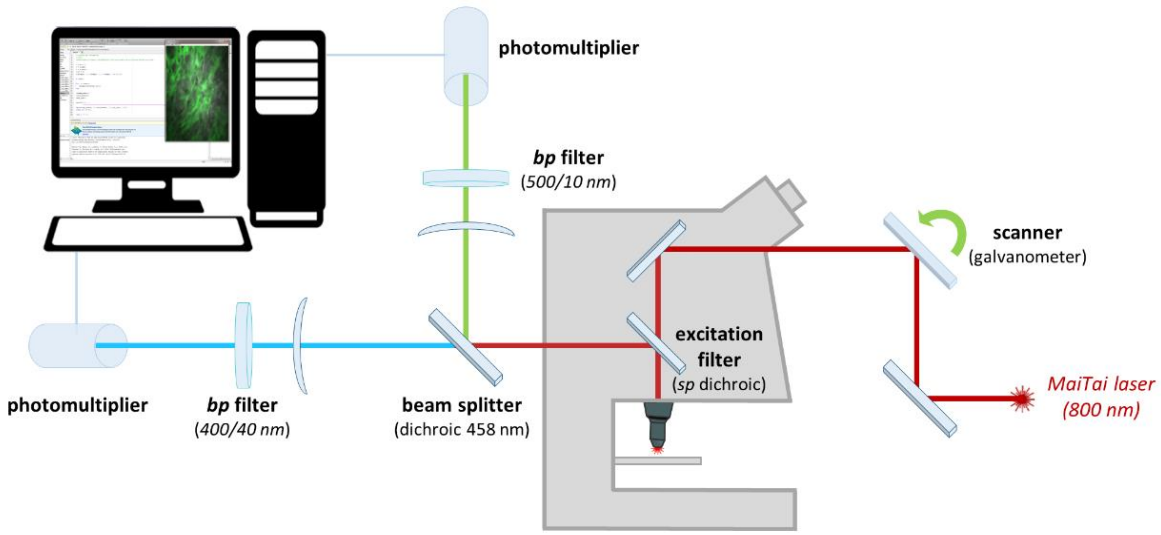

Figure 3.7 – Schematic of the home-built 2D imaging setup used for simultaneous imaging of second harmonic generation (SHG) and two-photon excited auto-fluorescence (TPEAF).

ScanImage 5.1 (Vidrio Technologies), an open source software, was used to acquire images with the laser scanning microscope [122]. A brief description of this system is as follows: a tuneable Titanium:Sapphire oscillator (Spectra-Physics Mai Tai®, 700-1000 nm, 100 fs, 80 MHz) was coupled through a galvanometric scanner to an upright microscope configured for epi-detection of SHG and TPEAF. A long pass dichroic beam splitter with cut-off at 775 nm was used to separate the laser excitation from the epi-collected emission. A further long pass dichroic beam splitter with cut-off at 458 nm was used in the collection path for separating the SHG and TPEAF signals, which after passing through narrow band pass filters centred at 400 nm and 500 nm respectively, were focused with short focal length lenses on the respective detectors (photomultiplier tubes). The laser oscillator was tuned at 800 nm. The narrow band pass filter used for TPEAF signal collection was selected after testing different filters for imaging cell autofluorescence, using the same laser wavelength (800 nm) as the one used for SHG (Figure 3.8). Each sample was imaged using a water dipping 20x magnification objective with 0.5 numerical aperture, 3x optical zoom using galvanometric scanning, and acquisition time of 16 ms per line for a 1024x1024 pixel image. The total incident power on the sample was approximately 70 mW.

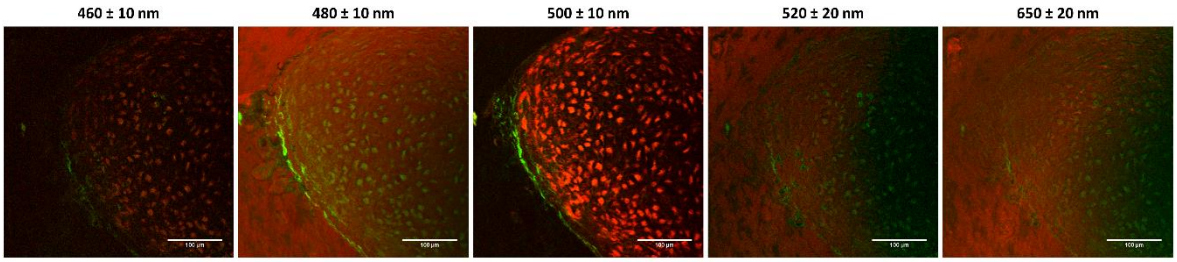

Figure 3.8 – Examination of different narrow band pass filters for two-photon excited auto-fluorescence (TPEAF) signal collection (red). SHG signal is shown in green. The sample used for methodology optimisation was a paraffin-embedded section of human articular chondrocyte cell pellet. Colour scales are not comparable between each image as acquisition settings were different for each filter. Scale bars correspond to 100 µm.

3.2.13 Multimodal imaging: combining CARS, SHG and TPEAF

Fetal femur-derived skeletal cell pellets were washed with PBS and fixed in a 4 % formaldehyde (v/v) solution for 25 minutes at room temperature. Cell pellets were washed with excess PBS, and images captured using a home-built system, as illustrated in Figure 3.9, which allows for image acquisition with CARS, SHG and TPEAF.

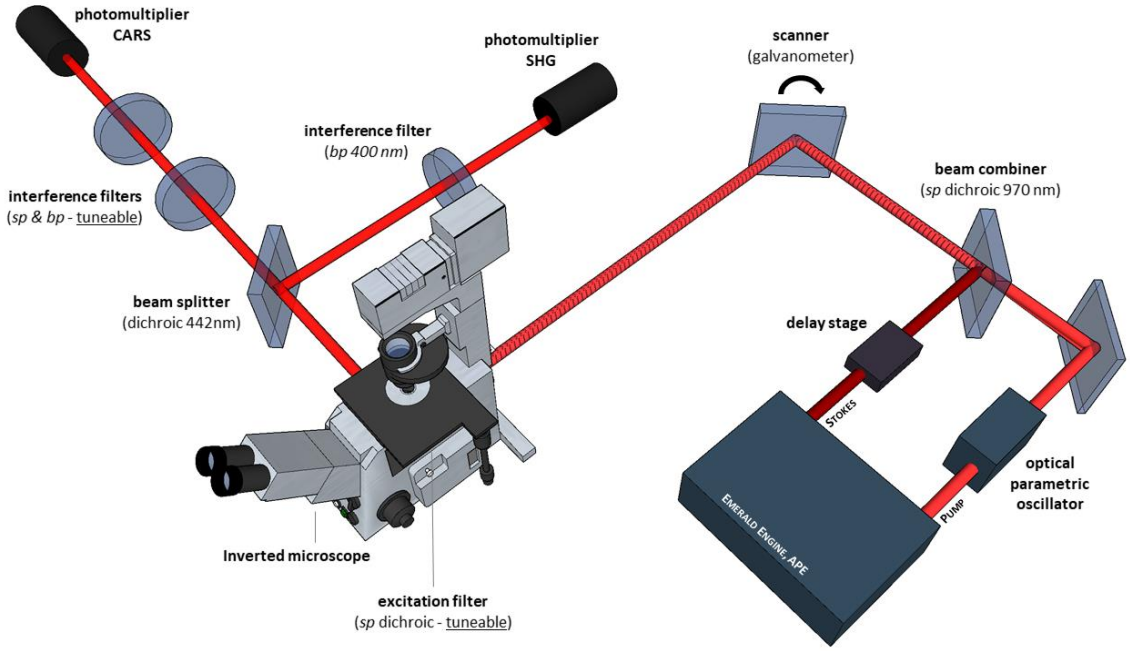

Figure 3.9 – Schematic of the home-built multimodal imaging setup used for 3D imaging, combining coherent anti-Stokes Raman scattering (CARS), second harmonic generation (SHG) and two-photon excited auto-fluorescence (TPEAF). The pump laser, excitation filter (short pass dichroic) and interference filters (short pass and band pass) are tuneable.

This multimodal laser scanning microscope also used ScanImage for image acquisition [122]. For CARS imaging, a fibre laser (Emerald Engine, APE, 1031 nm, 2 ps, 80 MHz,) was used as a Stokes beam, and the output of an OPO (APE, Levante

Emerald, 650-950 nm), which was synchronously pumped by the second harmonic (516 nm) of the fibre laser, was used as a pump beam. The two beams were made collinear and coupled to an inverted microscope (Nikon Ti-U) through a galvanometric scanner. The temporal overlap was controlled with a delay line, and the system was configured for epi-detection. For imaging lipids in the cell pellets the CH stretch mode at 2845 cm^{-1} was targeted, and the OPO was tuned to 797.8 nm. The total incident power on the sample was approximately 147 mW. The SHG (400 nm) and TPEAF (520 nm) signals were collected with the OPO beam at 800 nm. Each sample was imaged using a 20x magnification objective with 0.75 numerical aperture, 6x optical zoom using galvanometric scanning, 29 ms per line period for a 512x512 pixel image.

Before each experiment, a 40-µm polystyrene microsphere reference sample was imaged to calibrate the temporal delay (for the known CH vibrations of polystyrene) and optimise system performance. To verify if the signal collected was indeed due to CARS, additional images were acquired after modifying the delay stage, and after blocking the Stokes and the pump beam. An example of the system performance check is shown in Figure 3.10.

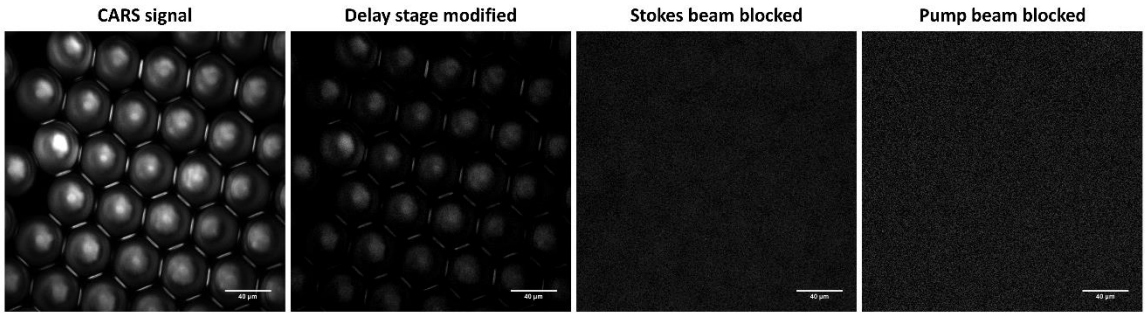

Figure 3.10 – System performance check for coherent anti-Stokes Raman scattering (CARS) signal using a 40-µm polystyrene microsphere reference sample. Images were acquired with modified delay stage, after blocking the Stokes beam and the pump beam. Scale bars correspond to 40 µm.

3.2.14 Live-cell multimodal imaging

Living cell pellets were washed with PBS and placed in a sterile coverslip cell chamber for live-cell imaging (Figure 3.11). Label-free multimodal imaging was performed using the home-built laser scanning system described in section 3.2.13. For CARS imaging, the CH stretch mode at 2845 cm^{-1} was targeted by tuning the OPO to 797.8 nm. The SHG signal was acquired using the same laser source at 797.8 nm. Each sample was imaged using a 20x magnification objective with 0.75 numerical aperture, with 14.5 ms per line period for a 1024x1024-pixel image. The total incident power on the sample was approximately 120 mW. After live-cell imaging, serum-free

chondrogenic media was replenished, and human fetal femur-derived skeletal cell pellets were maintained in a humidified chamber at 37 °C and 5 % CO_2.

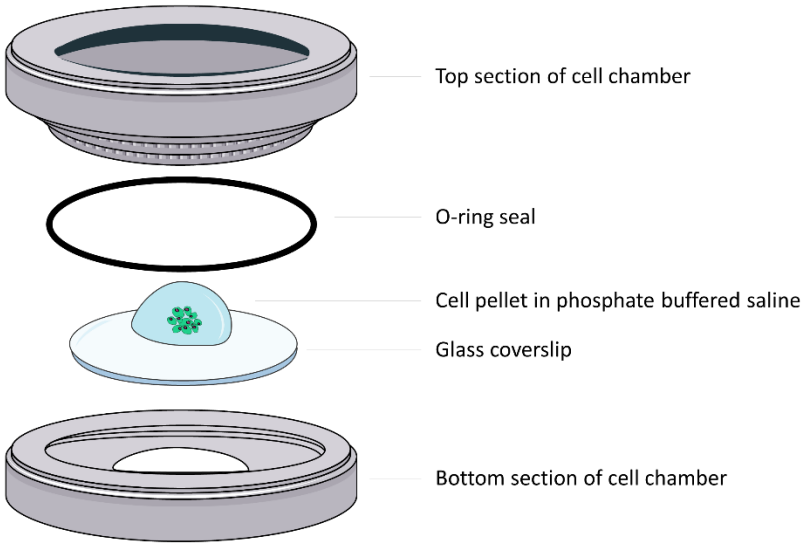

Figure 3.11 – Schematic of the coverslip cell chamber used for live-cell imaging on the multimodal inverted microscope.

3.2.14.1 Methodology optimisation

For live-cell multimodal imaging protocol optimisation, human articular chondrocytes were stimulated to generate cartilage tissue in an *in vitro* 3D pellet culture system. At day 5 of chondrogenic culture, living cell pellets were washed with PBS and placed in a sterile coverslip cell chamber for live-cell imaging. Label-free multimodal imaging was performed using the home-built laser scanning system described in section 4.2.13. After live-cell imaging, serum-free chondrogenic media was replenished, and cell pellets maintained in a humidified chamber at 37 °C and 5 % CO_2 for a further 3 days. At day 8 of pellet culture, a live/dead assay was performed to assess cell viability after live-cell imaging.

Cell pellets were incubated with 10 mM CellTracker™ Green and 5μg mL-1 ethidium homodimer-1 in DMEM/F12 media for 90 minutes at 37 °C. CellTracker™ Green is a fluorescent dye that passes freely through cell membranes into cells, and where it is transformed into cell membrane-impermeant reaction products (staining 'live' cells). Ethidium homodimer-1 enters cells with damaged membranes and the fluorescence is highly enhanced upon nucleic acid binding, emitting strong red fluorescence (therefore staining 'dead' cells). After incubation, fresh cell culture media was replenished and cell pellets were maintained at 37 °C for 1 hour. After washing with PBS, cells pellets were fixed with 95 % ethanol (v/v) for 5 minutes at -20 °C. A human articular cartilage sample was used as a control to optimise staining and imaging protocols. Fluorescence images to visualise live/dead cell viability were

captured using a Leica SP5 Laser Scanning Confocal microscope, with two argon laser lines (excitation/emission: 496 nm/506-544 nm for ethidium homodimer-1; excitation/emission for CellTracker™ Green: 561 nm/582-632 nm). Fluorescence microscopy images are shown in Figure 3.12, as an overlay of the recorded images at different focal planes. Although the used dyes did not penetrate into cell pellets (Figure 3.13), thus not allowing to make conclusions on the overall cell viability, it was possible to determine the laser power required for the live-cell imaging procedure (approximately 120 mW) to be used in fetal femur-derived skeletal cells without compromising the pellet structure.

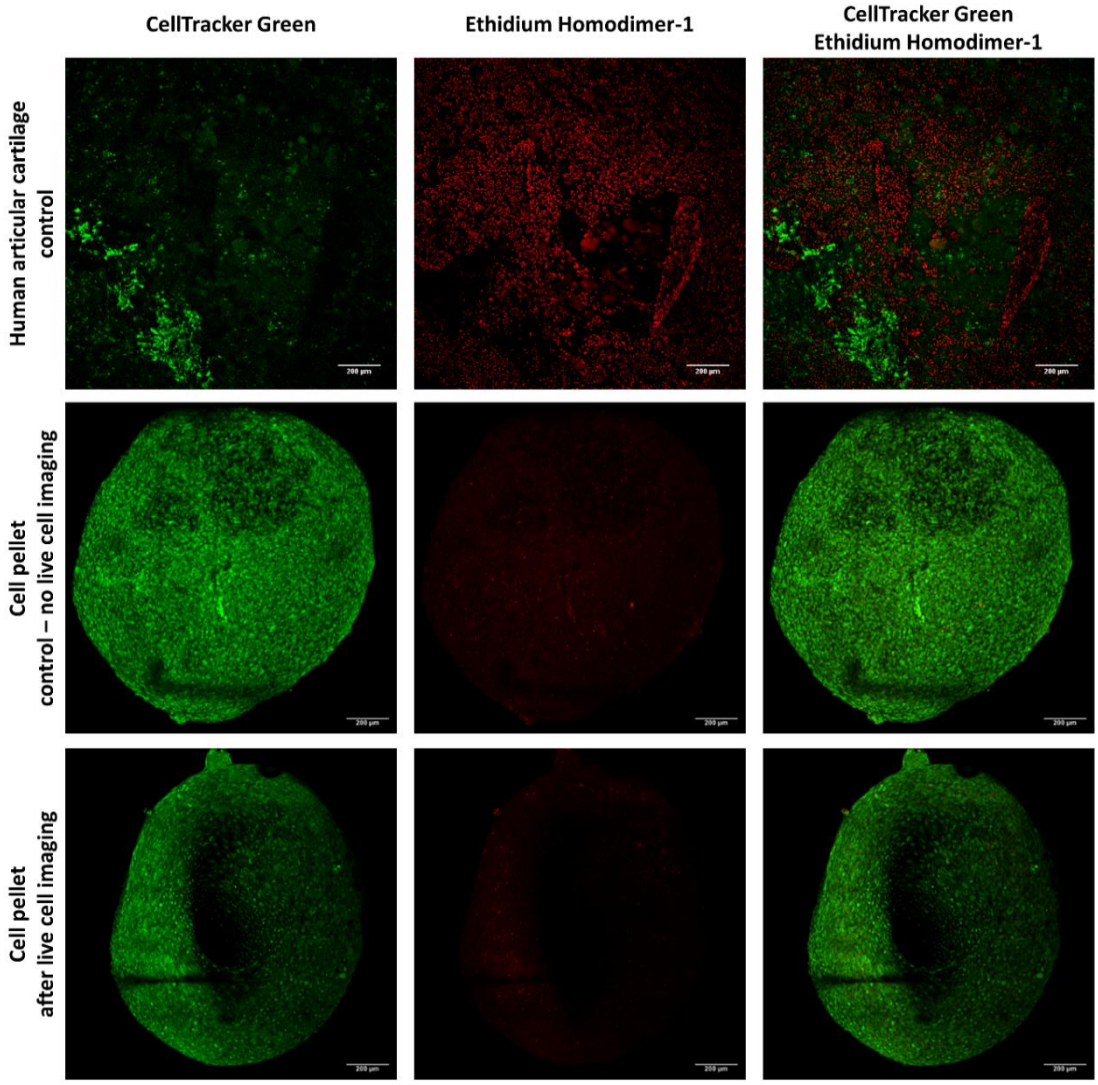

Figure 3.12 – Live-cell multimodal imaging protocol optimisation – live/dead assay to assess cell viability after live-cell imaging. A human articular cartilage sample was used as a control to optimise staining and imaging protocols. Live human articular chondrocyte cell pellets were imaged at day 5 using the home-built laser scanning system described in section 4.2.13. Cell viability was verified at day 8 of culture. Confocal fluorescence images show an overlay of the recorded images at different focal planes. Scale bars correspond to 200 µm.

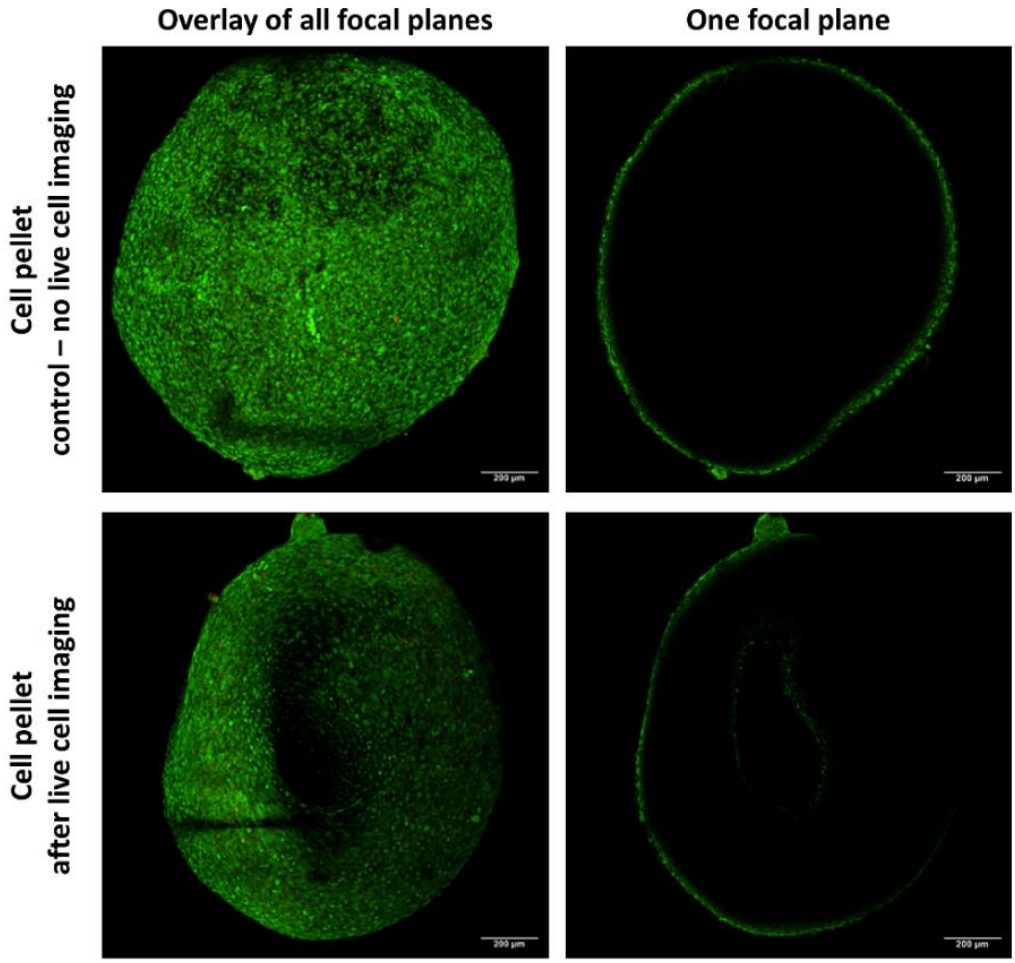

Figure 3.13 – Live-cell multimodal imaging protocol optimisation – live/dead assay to assess cell viability after live-cell imaging. Confocal fluorescence images as an overlay of the recorded images at different focal planes and as just one single focal plane revealed that the dyes used for the cell viability assay did not penetrate the cell pellets. Scale bars correspond to 200 μm.

3.2.15 CARS imaging at different wavenumbers

CARS imaging at different wavenumbers was performed in the same home-built system and conditions used for live-cell imaging. Fixed human fetal femur-derived skeletal cell pellets were placed in a sterile coverslip cell chamber for CARS imaging. The different vibrational modes, 1061 cm^{-1}, 1450 cm^{-1}, 1668 cm^{-1}, 2845 cm^{-1}, 2935 cm^{-1} and 3030 cm^{-1}, were targeted by tuning the OPO to 930.2 nm, 897.7 nm, 880.4 nm, 797.8 nm, 792.1 nm, and 786.2 nm, respectively. Table 3.2 shows the required modifications in the multimodal label-free imaging set up to acquire CARS images at different wavenumbers. For CARS imaging at other wavenumbers using this home-built system, a more detailed table can be consulted in Table A.1, Appendix A.1.

Table 3.2 – Vibrational modes targeted for coherent anti-Stokes Raman scattering (CARS) imaging and the corresponding modifications in the multimodal label-free imaging set up.

Raman peak	Vibrational assignment	Biochemical association	Pump laser	Excitation filter	Interference filters	
				short pass dichroic	*short pass*	*band pass*
1061 cm^{-1}	$\nu_s(OSO_3^-)$	glycosaminoglycans	930.2 nm	875 nm	no filter	840/12 nm
1450 cm^{-1}	$\delta(CH_2)$	proteins, collagen	897.7 nm	825 nm	800 nm	800/12 nm
1668 cm^{-1}	$\nu(C=O)$	amide I, collagen	880.4 nm	825 nm	800 nm	766/13 nm
2845 cm^{-1}	$\nu_s(CH_2)$	lipids	797.8 nm	750 nm	775 nm	643/20 nm
2935 cm^{-1}	$\nu_s(CH_3)$	proteins	792.1 nm	750 nm	775 nm	643/20 nm
3030 cm^{-1}	$\nu_{as}(CH_3)$	proteins	786.2 nm	750 nm	775 nm	643/20 nm

3.2.16 Image processing and analysis

The number of single lipid droplets in CARS images was counted using Fiji (Figure 3.14). CARS images were enhanced using histogram equalisation. After setting an automatic threshold level, a binary image was created by converting the original CARS image to black and white. Watershed segmentation was performed to automatically separate particles that are in contact with others. The segmented image was analysed using the Fiji command 'Analyze Particles'. The outlined lipid droplets were overlaid on the original image, and the count, area and average size of each lipid droplet calculated.

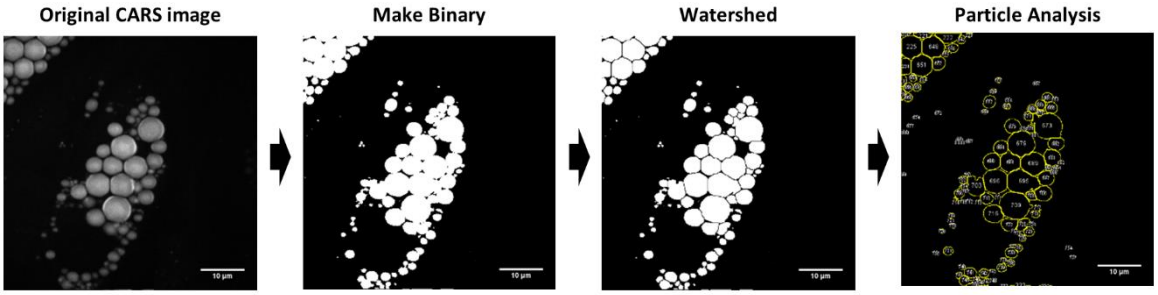

Figure 3.14 – Methodology for lipid droplet analysis using coherent anti-Stokes Raman scattering (CARS) imaging. CARS images were processed and analysed using Fiji using the commands 'Make Binary', 'Watershed' and 'Analyze Particles'.

For processing images acquired with the home-built laser-scanning microscope comprising SHG and TPEAF, multiple images were combined from the same sample as the pellet sections could not fit into a single field of view of the microscope. Tile scanning was performed using ScanImage. Image tiles were assembled using the Grid/Collection

stitching plugin from Fiji [123]. For data analysis of 3D images, volumes of interest (122.45x122.45x30 µm) were outlined for all different samples in order to allow the comparison of corresponding normalised values. 3D images and videos were recorded using CTVox (Bruker microCT).

For experiments further discussed in Chapter 5 and Chapter 6, CARS images were pre-processed using the rolling ball background subtraction tool. The size and number of cells, as well as the ratio between the quantity of collagen fibres to number of cells per area of interest, were quantified. CARS image processing and analysis to quantify number of cells consisted of image thresholding, noise removal and filling holes, watershed segmentation, followed by particle analysis (Figure 3.15).

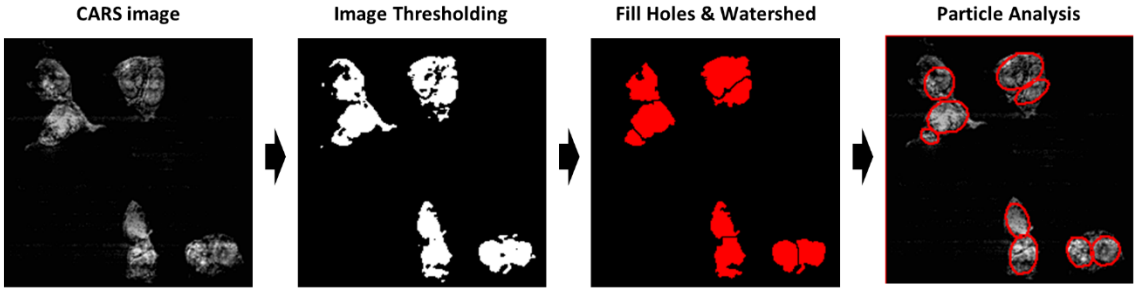

Figure 3.15 – Methodology for cell analysis using 3D coherent anti-Stokes Raman (CARS) imaging. CARS 3D images were processed and analysed using Fiji to investigate cell number and size in volumes of interest for each cartilage pellet.

CT-FIRE was used to automatically extract collagen fibres in SHG images (Figure 3.16), and quantify fibres with descriptive statistics, namely fibre angle, fibre length and fibre straightness [124]. This software combines the advantage of the fast discrete curvelet transform for denoising the image and enhancing the fibre edge features, with the advantage of fibre extraction algorithm for extracting individual fibres [124, 125].

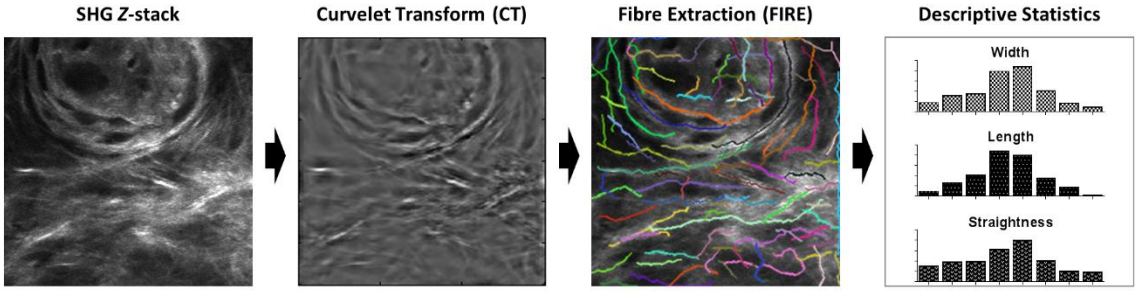

Figure 3.16 – Methodology for quantification of collagen fibre width, length and straightness. Second harmonic generation (SHG) 3D images were analysed using CT-FIRE to extract collagen fibre details.

3.2.17 Statistical analysis

All experiments were performed using three independent samples. Graphs were prepared using GraphPad Prism 7 and statistical analysis was performed using IBM® SPSS® Statistics version 21.0. Data distributions were tested for normality using the Shapiro-Wilk test and statistical significance was tested using one-way analysis of variance (ANOVA) with Tukey's post-hoc test for samples following a normal distribution, or the Mann-Whitney U-test for samples not following a normal distribution. Differences were considered to be statistically significant at $P \leq 0.05$.

4

TRACKING ADIPOGENIC DIFFERENTIATION OF SSCS BY LABEL-FREE CHEMICALLY SELECTIVE IMAGING

Chapter 4 presents work published in the peer-reviewed journal Chemical Science: "Tracking adipogenic differentiation of skeletal stem cells by label-free chemically selective imaging", Justyna P Smus, Catarina Costa Moura*, Emma McMorrow, Rahul S Tare, Richard OC Oreffo, Sumeet Mahajan. Chemical Science, 2015. 6: p. 7089-7096. doi: 10.1039/C5SC02168E.*

Contributions: *JP Smus and CC Moura are joint first authors. CC Moura performed bone marrow preparation, cell culture, Raman spectroscopy, CARS imaging, RNA extraction and cDNA synthesis, RT-qPCR, Oil Red O staining, data analysis, image processing and analysis, statistical analysis, and participated in the design of the study. JP Smus performed Raman spectroscopy, CARS imaging, data analysis, image processing and analysis, and participated in the design of the study. E McMorrow performed cell culture and Oil Red O staining. RS Tare, ROC Oreffo and S Mahajan conceptualised, designed and coordinated the study. All authors contributed to the writing of the manuscript and gave final approval for publication.*

4.1 Abstract

CARS is a chemically selective label-free imaging technique which is rapidly emerging as a powerful alternative to conventional microscopy in biomedicine. The strength of this imaging approach is the provision of rapid insight into chemical distribution especially of small biomolecules such as lipids. The label-free, non-destructive and non-invasive nature of CARS lends itself for use with stem cells, as labelling or staining will render stem cells otherwise unsuitable for therapy. Isolation, enrichment and characterisation of skeletal stem cells (SSCs) and their progeny is of tremendous significance in regenerative medicine. However, SSC differentiation into bone, cartilage or fat progeny, is currently assessed using several invasive and, typically, destructive methodologies. Thus, CARS presents an exciting alternative to interrogate the differentiation of SSCs in their natural state. In the current study, the adipogenic differentiation of SSCs over time was examined using CARS imaging, and the observed differentiation was verified using molecular analysis of gene expression as well as comparison to results from conventional Oil Red O lipid staining. CARS analysis provided an enhanced resolution and definition of lipid droplets, detectable as early as 24 hours and 72 hours after adipogenic induction. Quantification of the CARS image data sets also demonstrated a change in lipid droplet size distribution during the course of adipogenesis over 14 days. The current studies pave the way for the use of CARS as a powerful chemical imaging tool in therapeutics, regenerative medicine and skeletal cell biology.

4.2 Introduction

Imaging remains the cornerstone of much of modern biological research providing exquisite resolution of structure and allowing the study of biochemical processes in cells, tissues and whole organisms. However, the current cellular imaging techniques rely on staining or labelling, with dyes or fluorophores, to visualise target molecules. This is far from ideal as stains are often non-specific and are, typically, only suitable for fixed specimens, while fluorescent labels need to be attached and therefore can interfere with natural processes and, furthermore, can be hampered by photo-bleaching. Consequently, the results obtained from such experiments cannot be readily extrapolated to unlabelled cells in a living organism. Vibrational spectroscopy provides an alternative approach, providing chemically selective contrast, generated due to intrinsic vibrations of molecules in their native state, and thus is label-free [126].

One such vibrational spectroscopic technique is CARS, which permits rapid, non-invasive and non-destructive, label-free chemical imaging. In essence, in CARS, the

bond vibrations characteristic of a molecule are targeted by using two excitation laser beams (pump and Stokes beam) which are temporally and spatially overlapped [127, 128]. In CARS, the pump beam (at frequency ω_{pump}) and a Stokes beam (at ω_{Stokes}) combine to yield an anti-Stokes signal at frequency $\omega_{CARS} = 2\omega_{pump} - \omega_{Stokes}$. When the frequency difference between the pump and the Stokes beams matches the frequency of a vibrational mode of the molecule of interest, vibrational coherence is induced. The outcome of this process is a dramatically enhanced anti-Stokes Raman signal that is the foundation for the increased vibrational contrast and sensitivity achieved in CARS which leads to rapid video-rate imaging with <10 μs dwell times [60, 129, 130]. CARS signals can be up to 9 orders of magnitude stronger than conventional Raman scattering [131, 132]. Furthermore, as a multiphoton process, CARS has natural z-sectioning ability enabling 3D imaging [133]. Typically, near-infrared wavelengths are used allowing deep penetration into the sample and therefore thick tissues can be imaged with ease [66]. Consequently CARS offers a chemically selective label-free technique for cells, tissues and organisms in biology and medicine [31].

In biomedicine, chemically selective, label-free imaging is crucially required in the area of stem cells and regenerative medicine given the requirement for original (un-labelled/un-stained) samples for *in vivo* application in humans. Over the last decade, stem cell-based therapies have come to the fore for tissue repair and skeletal regeneration [2], necessitating the development of appropriate technologies to enable stem cell characterisation and thus enhance therapeutic applications. While CARS imaging has been applied to stem cells [24, 73], CARS application in human skeletal regeneration studies, to date, remains limited. Current available techniques to characterise and monitor the ability of human SSCs to form cartilage, bone and fat, are invasive and unsuitable for time-course studies. Schie and co-workers performed a primordial assay using adipocytes from human bone marrow stem cells and imaged the lipid droplets after 21 days of differentiation, with the primary objective to improve the simultaneous imaging in forward- and epi-CARS microscopic system [72]. Neither the differentiation process of SSCs nor the effect of chemical modulation was examined, nor was any CARS based analysis performed.

In this chapter, the application and advantageous use of label-free CARS imaging to study early adipogenic differentiation of human SSCs is shown. In the absence of exogenous labels, lipid droplet formation was monitored to assess temporal changes in adipogenesis, subsequently correlated with gene expression analysis. The current work establishes the utility of chemically selective CARS imaging for skeletal cell biology and

potential wider applications in hard and soft tissue characterisation in the field of regenerative medicine.

4.3 Methods

All the methodology used in this chapter is detailed in Chapter 3.

4.4 Results and Discussion

In this chapter, SSC differentiation into adipocytes was studied, as well as the effect of different chemical factors using the non-invasive, non-destructive and chemically selective label-free technique of CARS.

At the outset Raman spectroscopy was carried out to establish the chemically selective vibrational frequency for imaging lipids in SSCs by CARS. Therefore Raman spectra were obtained by focussing on large lipid droplets in differentiated adipocytes. A representative spectrum is shown in Figure 4.1. SSCs were cultured for 14 days in adipogenic media in order to visualise lipid droplets and obtain their Raman spectra, since, unlike CARS, signals in Raman spectroscopy are weak. Nevertheless, the spectra were characteristic and reproducible for different lipid droplets acquired in different cells. A strong peak at 2845 cm^{-1} corresponds to the CH_2 symmetric stretching frequency, indicating the predominant presence of lipids. Additional peaks at 1440 cm^{-1} and 1650 cm^{-1} correspond to the C-H deformation and C=C stretching vibrations, respectively [134], and symmetric CH_3 stretching modes at 2935 cm^{-1} confirm the assignment to the presence of lipid droplets in adipocytes [135]. Furthermore, 1650 cm^{-1} and 2935 cm^{-1} peaks are associated with amide I and CH_3 stretching in proteins. As the content of unsaturated fatty acids in lipid droplets is known to be variable [136], these peaks likely originate from adipose differentiation-related protein and caveolin-2ß, which are proteins dominantly associated with lipid droplets and their membranes [137, 138] . These peaks were not observed in undifferentiated SSCs (cultured in basal media, no lipid droplets) under the acquisition conditions. When compared to traditional characterisation techniques, this Raman-based spectral analysis thus allows identifying, locating and comparing molecular composition between different samples. Nevertheless, the Raman spectra of the samples confirmed the strong presence of the CH stretch vibration characteristic of lipids [62], and established the suitability of using the 2845 cm^{-1} vibrational frequency to image lipid droplets in SSCs and was subsequently used for CARS imaging.

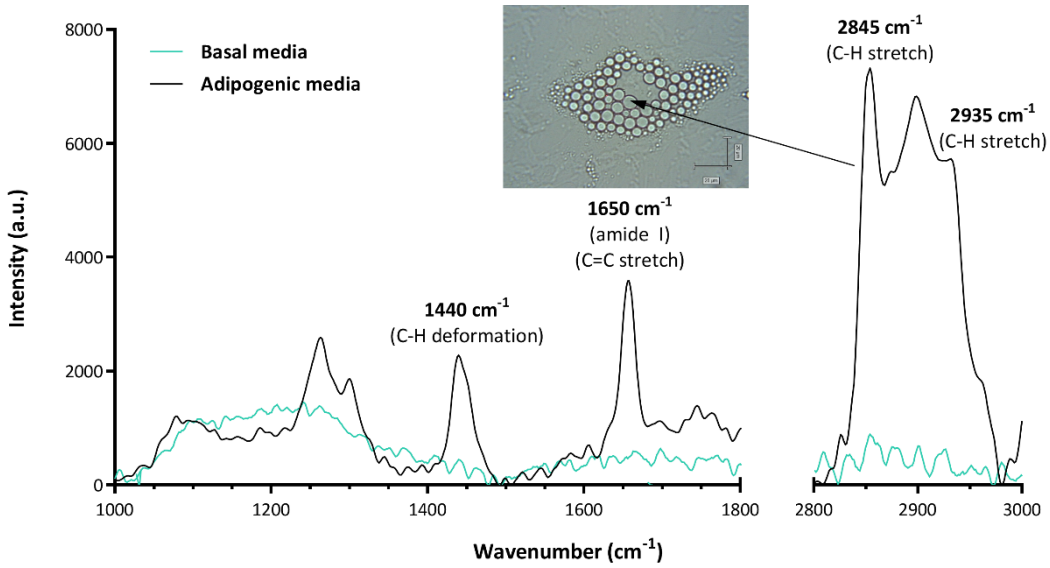

Figure 4.1 – Raman spectra of differentiated (adipogenic media) and undifferentiated (basal media) human adult skeletal stem cells (SSCs) (laser 633 nm, 0.6mW power), and bright field image of lipid droplets that yielded the Raman signal. The spectrum from cells cultured for 14 days in adipogenic media was acquired by directly focussing on a single lipid droplet. The prominent CH stretch mode peak at 2845 cm^{-1} was targeted to image lipids using coherent anti-Stokes Raman scattering (CARS) microscopy.

To study the temporal evolution of their differentiation, SSCs were cultured in adipogenic and basal media, and temporal changes observed using CARS over 14 days. Adipocytes are readily identified by the accumulation of lipid droplets through the differentiation process [139]. The CH stretch vibration signal at 2845 cm^{-1} was monitored by CARS microscopy by tuning the pump and OPO beams to 835 nm and 1097 nm, respectively. Representative CARS images acquired at day 1, 3, 7 and 14 are shown in Figure 4.2. Additionally, adipocytes were imaged at the same time-points using conventional Oil Red O staining of lipids. CARS microscopy and Oil Red O staining images of SSCs cultured in basal media, which show very few lipid droplets and do not show an increase over time, are shown in Figure 4.3.

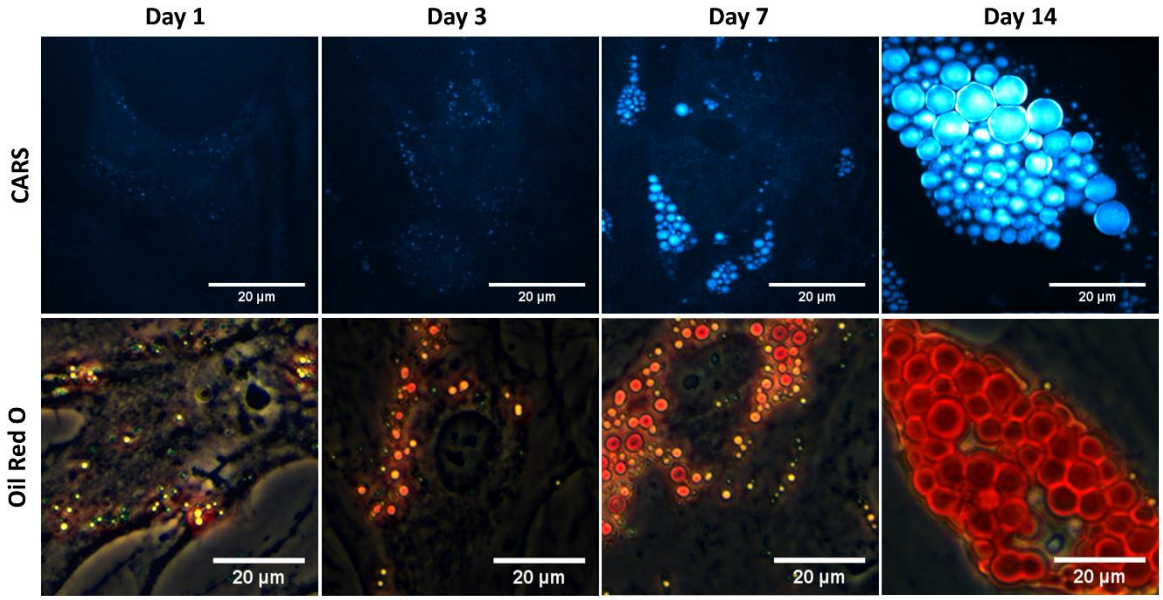

Figure 4.2 – Comparison of label-free coherent anti-Stokes Raman scattering (CARS) imaging and Oil Red O staining (phase contrast) to assay adipogenic differentiation of skeletal stem cells (SSCs). SSCs were cultured in adipogenic media for 1, 3, 7 and 14 days. Scale bars correspond to 20 µm.

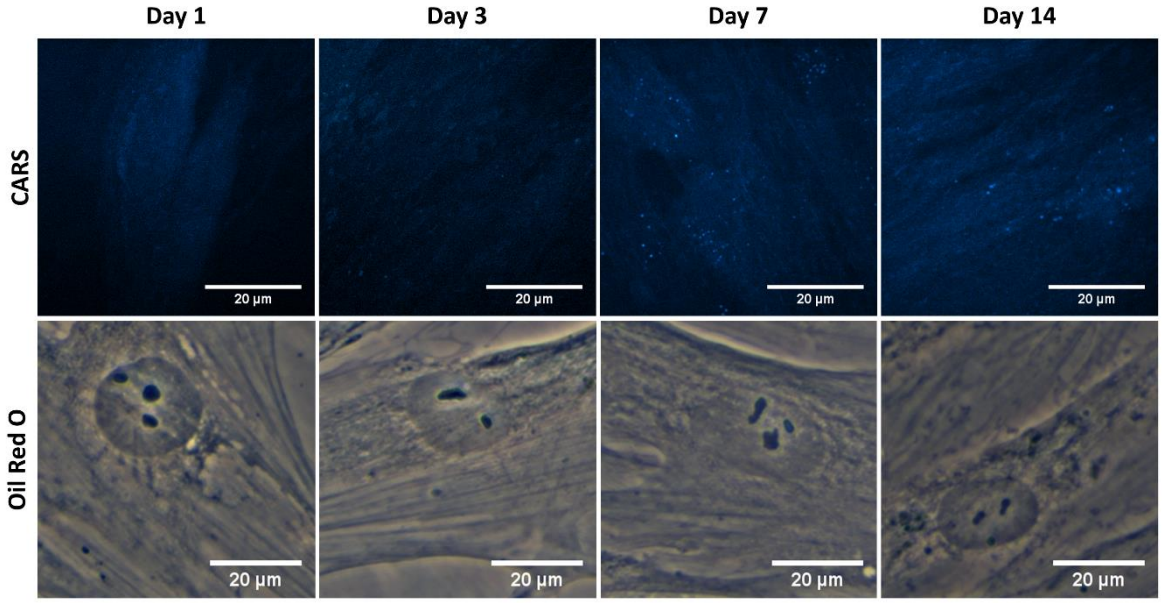

Figure 4.3 – Comparison of label-free coherent anti-Stokes Raman scattering (CARS) imaging and Oil Red O staining (phase contrast) of skeletal stem cells (SSCs) cultured in basal media for 1, 3, 7 and 14 days. Scale bars correspond to 20 µm.

Images taken at different magnifications with Oil Red O staining are presented in Figure 4.4, Figure 4.5, and Figure 4.6, to demonstrate cell growth over time over different fields of view. Overall, these results demonstrate that while there is good correspondence between both methodologies, several advantages of CARS over Oil Red O staining are clearly apparent. CARS provided a chemically-selective and label-free approach, in contrast to the application of Oil Red O staining that required a much more laborious process and is subject to variability depending on preparation conditions

[140]. Most significantly, in terms of performance, CARS displays a higher sensitivity towards detection of small lipid droplets (blue) observable after only 24 hours and 72 hours, but poorly visualised using Oil Red O staining. Moreover, at low levels of lipid droplet presentation, such as at day 1, the generation of artefacts due to Oil Red O crystal deposition and non-specific binding cannot be ruled out. These results demonstrate the feasibility of CARS as a label-free chemical imaging tool to monitor SSCs differentiation in a temporal manner, thereby facilitating detection of early adipogenic differentiation.

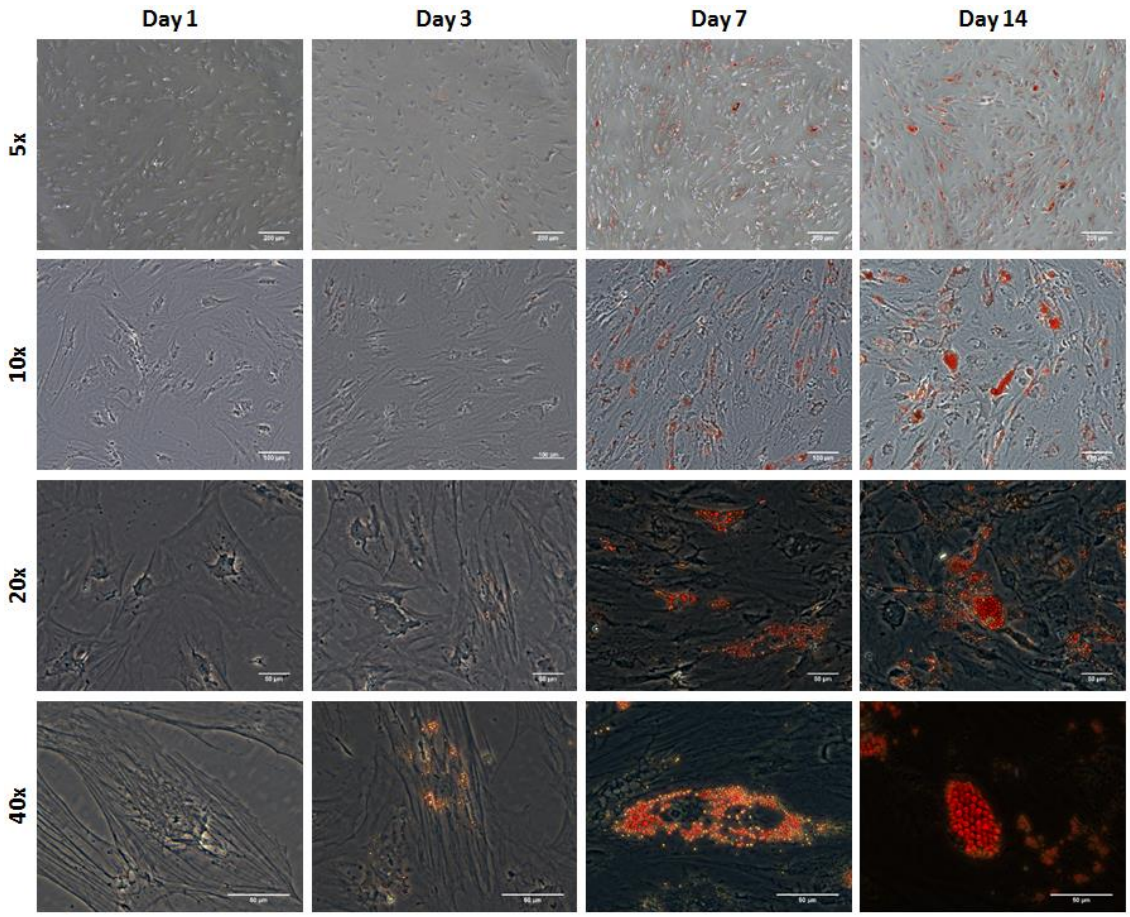

Figure 4.4 – Oil Red O staining images using different objectives (5x, 10x and 20x) of skeletal stem cells (SSCs) cultured in adipogenic media for 1, 3, 7 and 14 days (Donor 1). Scale bars correspond to 200 µm (5x), 100 µm (10x), and 50 µm (20x and 40x).

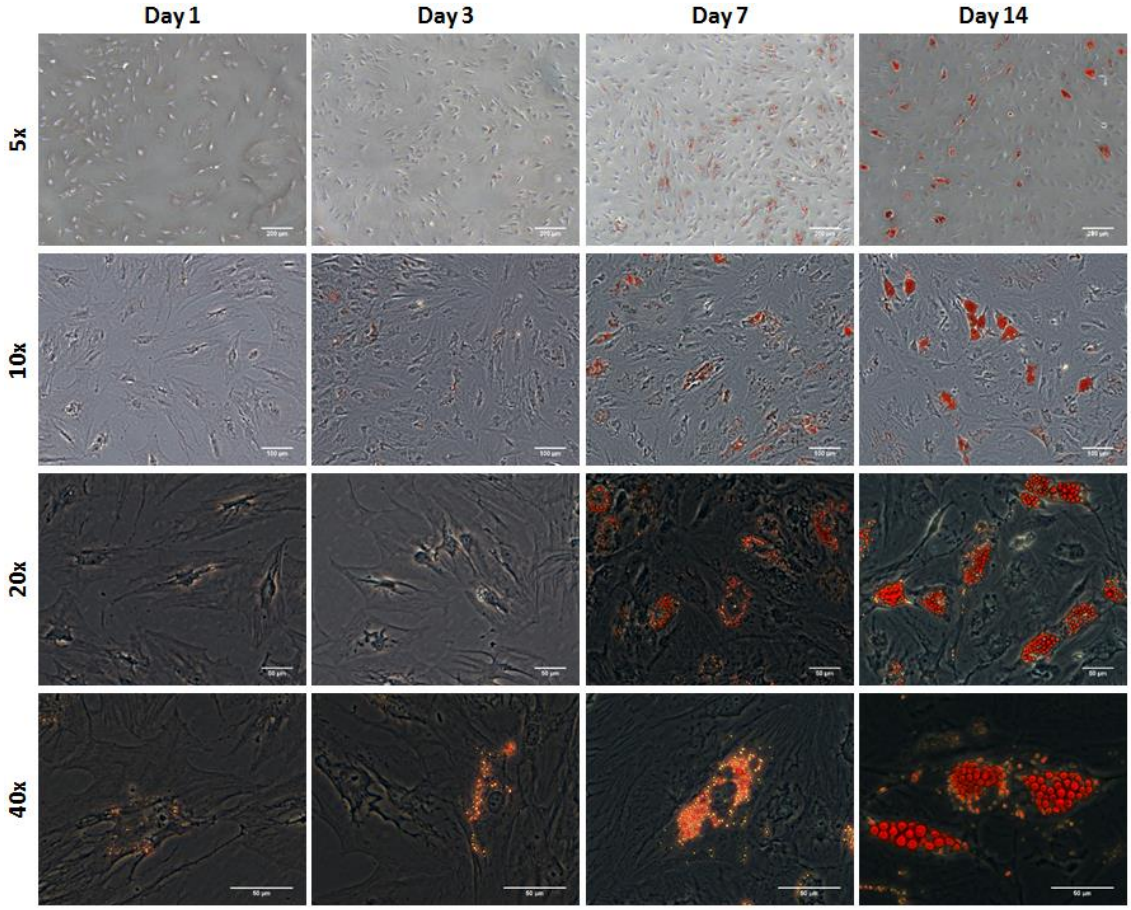

Figure 4.5 – Oil Red O staining images using different objectives (5x, 10x, 20x and 40x) of skeletal stem cells (SSCs) cultured in adipogenic media for 1, 3, 7 and 14 days (Donor 2). Scale bars correspond to 200 µm (5x), 100 µm (10x), and 50 µm (20x and 40x).

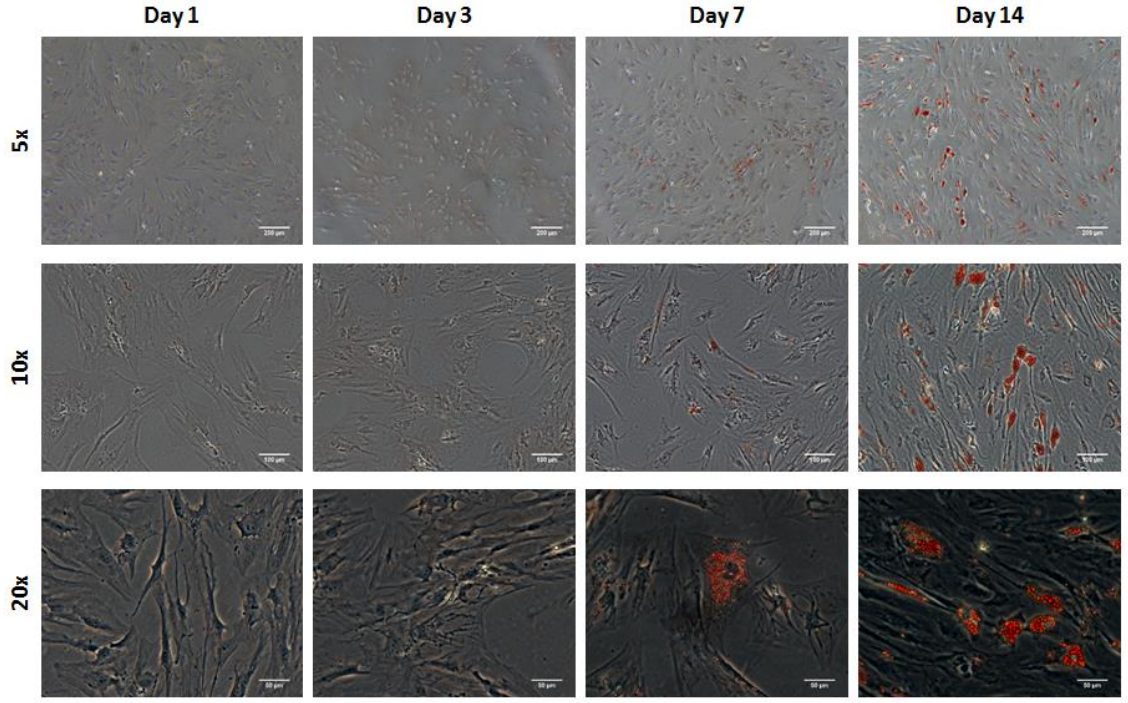

Figure 4.6 – Oil Red O staining images using different objectives (5x, 10x, 20x and 40x) of skeletal stem cells (SSCs) cultured in adipogenic media for 1, 3, 7 and 14 days (Donor 3). Scale bars correspond to 200 µm (5x), 100 µm (10x), and 50 µm (20x).

Image analysis was carried out to quantify the increase in lipid droplets and change in lipid size. Lipid droplet quantification observed using CARS is shown in Figure 4.7. As differentiation proceeds, adipogenesis leads to increased lipid accumulation in contrast to control cultures (undifferentiated cells maintained in basal media). The presence and change in the number of lipid droplets within the cultures was further analysed (Figure 4.7b). The presence of only small lipid droplets (<0.2 μm^2) was detected at day 1. However, by day 3, small (<0.2 μm^2) and medium (0.2–10 μm^2) lipid droplets had increased in number. Finally, at day 7 and day 14, it was possible to detect a decrease in the number of small lipid droplets, and an increase in the number of medium (0.2–10 μm^2) and large (>10 μm^2) lipid droplets. This may suggest that large- and medium-sized droplets grow at the expense of small droplets as differentiation progresses. The increase in number of small and medium lipid droplets, respectively, points to early changes during SSC differentiation to adipocytes detected by CARS before they are fully formed.

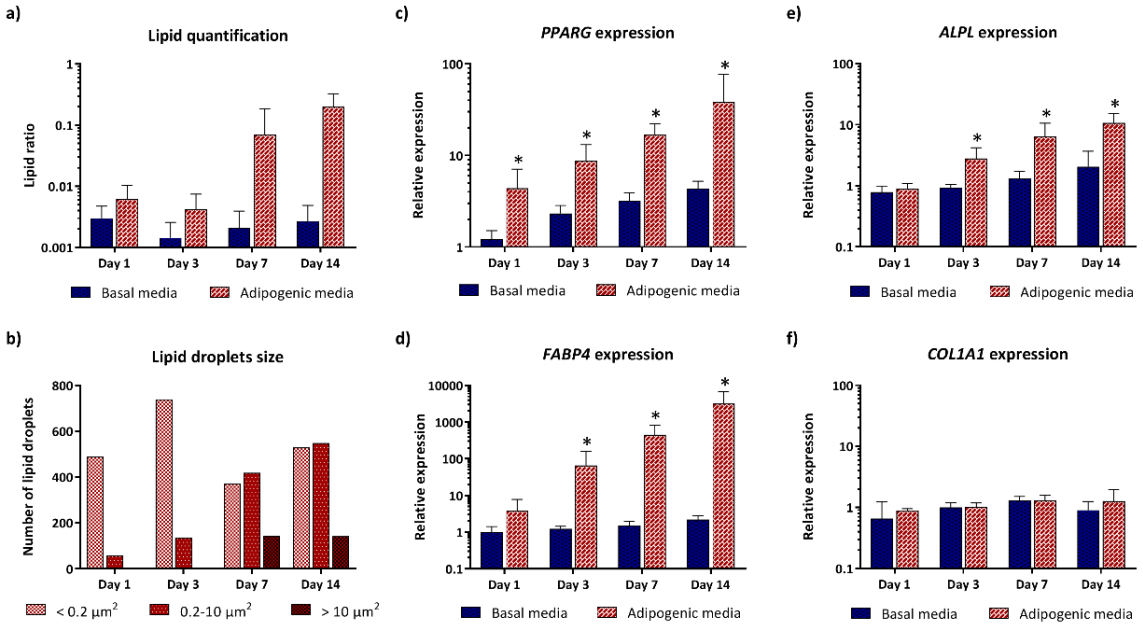

Figure 4.7 – Quantitative analysis of coherent anti-Stokes Raman scattering (CARS) images and comparison with gene expression profiles. (a) Ratio of lipid area to total image area and (b) size of lipid droplets in skeletal stem cells cultured in adipogenic media, for 1, 3, 7 and 14 days. Expression of (c) *PPARG* (d) *FABP4*, (e) *ALPL* and (f) *COL1A1* in skeletal stem cells (SSCs) cultured in basal and adipogenic media, for 1, 3, 7, and 14 days. Relative expression was normalized to *ACTB*, and day 0 values were set to an expression of one. Data represent the average of three independent patient samples plotted and error bars represent standard deviation. **P*<0.05, calculated using Mann–Whitney test.

In order to confirm adipogenic differentiation and correlate to the CARS imaging, the gene expression profile of characteristic adipogenic genes (*PPARG* and *FABP4*) and non-specific (osteogenic) genes (*COL1A1* and *ALPL*) at corresponding time-points was examined. The expression profile in basal and adipogenic media is shown in Figure 4.7c-f. *PPARG* expression, a nuclear receptor gene known to regulate the development of adipose tissue [141], increased significantly during differentiation into adipocytes (Figure 4.7c). From day 1 to day 14, large variation in *PPARG* relative expression was observed in SSCs cultured in adipogenic media, and expression levels were 39-fold higher at day 14. The increase in *PPARG* expression, a key regulator gene in adipogenesis, appears to correlate with the development and increase of lipid droplets in SSCs cultured in adipogenic media, as shown in Figure 4.2. In addition, *FABP4* expression (encodes fatty acid binding protein in adipocytes during adipogenic differentiation) known to be regulated by *PPARG* agonists, insulin and fatty acids [142], was assessed. Comparing the values between SSCs cultured in adipogenic media with day 0 cultures, *FABP4* displayed a 66-fold increase in expression at day 3, a 458-fold increase at day 7, and 3180-fold increase at day 14. *FABP4* expression exponentially increased compared to undifferentiated cells (Figure 4.7d). *ALPL* and *COL1A1* expression was also assessed as a control (Figure 4.7e and Figure 4.7f) [143].

Adipogenesis and osteogenesis share the same pathway in the early stromal differentiation cascade [144], and *ALPL* is believed to be involved, in an as yet undetermined manner, in the control of adipogenesis – *ALPL* is associated with intracellular lipid droplets [145, 146]. In Figure 4.7e, a modest increase in *ALPL* relative expression during adipogenesis was observed which suggests that *ALPL* also has a role in the adipogenic differentiation of SSCs. However, *COL1A1* expression was unchanged over time in differentiated and undifferentiated cells as expected. Such molecular analysis to monitor gene expression, although destructive and ensemble based, remains currently a key sensitive tool to monitor phenotypic changes in cells. The CARS imaging results correlated closely with the gene expression studies, affirming the utility of CARS in skeletal stem cell biology.

4.5 Conclusions

To date, SSC differentiation has been characterised and studied using invasive methods; therefore, a reliable non-invasive, non-destructive and label-free (stain-less) imaging technique is urgently required to evaluate SSC fate and function. The current chapter indicates that the chemically selective technique of CARS imaging provides an ideal alternative to monitor SSC differentiation. Lipid accumulation within adipocytes

can be visualised earlier, at higher definition and resolution, compared to conventional Oil Red O staining approach. This study confirms the robust potential of a CARS-based assay to monitor and understand the effect of physicochemical parameters on stem cell differentiation. The results establish the value of using CARS as a label-free chemical imaging technique for skeletal stem cell biology with implications therein for wider stem cell biology, regenerative medicine and therapeutics.

.

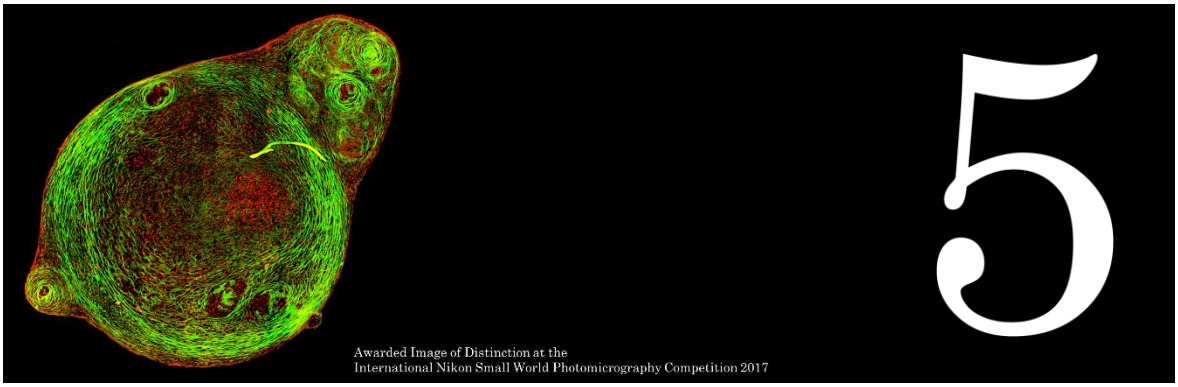

5

QUANTITATIVE TEMPORAL INTERROGATION IN 3D OF BIOENGINEERED HUMAN CARTILAGE USING MULTIMODAL LABEL-FREE IMAGING

Chapter 5 presents work submitted to the peer-reviewed journal Integrative Biology: "Quantitative Temporal Interrogation in 3D of Bioengineered Human Cartilage using Multimodal Label-free Imaging", Catarina Costa Moura, Stuart A. Lanham, Tual Monfort, Konstantinos N. Bourdakos, Rahul S. Tare, Richard O. C. Oreffo, Sumeet Mahajan.

Contributions: CC Moura performed cell culture, molecular and histology lab work, Raman spectroscopy, 2D and 3D imaging, data and image processing and analysis, statistical analysis, and participated in the design of the study. SA Lanham contributed to the 3D imaging processing and analysis. S Mahajan, T Monfort and KN Bourdakos designed the multimodal microscopy systems, and T Monfort and KN Bourdakos carried out the construction and set-up. RS Tare, ROC Oreffo and S Mahajan conceptualised, designed and coordinated the study. All authors contributed to the writing of the manuscript and gave final approval for publication.

5.1 Abstract

The unique properties of skeletal stem cells have attracted significant attention in the development of strategies for skeletal regeneration. However, there remains a crucial unmet need to develop quantitative tools to elucidate skeletal cell development and monitor the formation of regenerated tissues using non-destructive techniques in 3D. Label-free methods such as CARS, SHG and TPEAF microscopy are minimally invasive, non-destructive, and present new powerful alternatives to conventional imaging techniques. This study details a combination of these techniques in a single multimodal system for the temporal assessment of cartilage formation by human skeletal cells. The evaluation of bioengineered cartilage, regarding collagen amount per cell, collagen fibre structure and chondrocyte distribution, was performed using a 3D non-destructive platform. 3D label-free temporal quantification paves the way for tracking skeletal cell development in real-time and offers a paradigm shift in tissue engineering and regenerative medicine applications.

5.2 Introduction

Articular cartilage damage as a result of trauma, injury or degeneration can result in tissue loss and a deterioration in the specialised extracellular matrix [147]. Skeletal stem cells, present in bone marrow stroma, have the capacity to differentiate and give rise to the stromal lineages, namely bone, haematopoiesis-supportive stroma, fat and cartilage [2, 14, 17]. The ability to enrich for skeletal stem cells from bone marrow has enabled the evaluation and application of this multipotent stem cell population in skeletal reparative strategies, including cartilage regeneration. Cartilage tissue engineering using, for example, three-dimensional scaffold-free pellet cultures has been extensively applied for *in vitro* cartilage formation [14, 148]. However, these culture systems typically rely on two-dimensional (2D) imaging modalities to provide biological information [21, 149]. Furthermore, current available techniques for skeletal cell characterisation are: i) invasive (involve labels or stains), ii) require cell fixation or lysis, and/or iii) are destructive. Thus, there remains a crucial unmet need to develop appropriate tools to follow skeletal stem cell development and to monitor the formation of regenerated tissues using non-destructive, non-invasive and label-free techniques that, importantly, enable temporal interrogation in 3D. The main objective of the work described in this chapter was to establish multimodal label-free imaging as a platform to quantitatively assess and evaluate the development of human fetal skeletal cells towards a cartilage phenotype in 3D, non-destructively, and in the absence of any labelling with dyes or fluorophores.

Techniques which rely on the measurement of vibrational information such as spontaneous Raman spectroscopy and CARS microscopy are inherently non-invasive, non-destructive, and chemically selective. Although spontaneous Raman spectroscopy has been used to perform quantitative volumetric analysis of 3D stem cell cultures [21], the required long acquisition times preclude rapid (≈ 10 μs per pixel) or video-rate (>5 frames per second) imaging. In contrast, coherent Raman imaging techniques excite vibrational coherences in molecules which can enhance signals by $>10^5$ times [150].

Research by Downes et al. and our group has demonstrated that CARS microscopy can be applied to image the differentiation of ADSCs into osteoblasts [151], and skeletal stem cells into adipocytes [152], respectively. However, the application of coherent Raman techniques in assessing chondrogenesis (differentiation into cartilage) has not been studied. Moreover, 3D imaging using CARS or its multimodal combination with other label-free techniques has not been applied to analyse chondrogenic cultures or bioengineered cartilage, obtained through differentiation of fetal skeletal cells into chondrocytes.

Crucially, current available lasers allow the use of higher harmonic generation techniques, such as SHG, in conjunction with CARS on a multimodal system [153]. SHG is a second-order coherent process in which non-centrosymmetric structures, *i.e.* structures lacking a centre of symmetry, combine two lower energy photons from an excitation source to generate photons with exactly twice the incident frequency [77, 79]. Type I and Type II collagen have a hierarchy of non-centrosymmetric structures within each fibril and both form aligned striated fibres creating a super-structure (high degree of crystallinity) resulting in high SHG activity. In contrast, Type IV collagen has no fibrillary structure and consequently the SHG signal generated is insufficient for imaging [83-85]. Type II collagen is a principal component of cartilage tissue and represents more than 90 % of the collagen in articular cartilage extracellular matrix [86-88]. Given SHG has the established ability to directly (without labelling) visualise collagen fibres it is an ideal modality to provide comprehensive structural information on their arrangement within a 3D cell construct such as cartilage pellets.

In addition to CARS and SHG, TPEAF imaging offers another label-free modality to interrogate cellular composition and tissue development, providing complementary information [92-95]. Two-photon excitation fluorescence has reduced phototoxicity/photodamage compared to single-photon fluorescence microscopy, as explained in Chapter 2, section 2.4 [93, 94]. Flavin adenine dinucleotide (FAD), a redox co-factor associated with mitochondria, is involved in redox reactions in living cells, as well as several other cellular pathways including biosynthetic processes. These co-

enzymes contribute significantly to the cellular auto-fluorescence. Consequently TPEAF enables non-destructive imaging of living cells and tissues without the interference and, crucially, toxicity of exogenous dyes [93, 96], and TPEAF has been applied to image cells undergoing chondrogenesis [98]. TPEAF imaging of cells in cartilaginous pellets of fetal skeletal cells thus provides an invaluable method to elucidate the spatial organisation of cells within the extracellular matrix of cartilaginous pellets.

Given that CARS, SHG and TPEAF are all multiphoton microscopy techniques and therefore have inherent z-sectioning capability, this allows 3D imaging as well as the application of near infrared wavelengths for deep penetration into a 3D construct and thick tissue samples, enabling detailed imaging [154]. The multimodal combination of complementary imaging techniques, namely CARS, SHG and TPEAF, is highly advantageous and could provide a holistic insight into the development and differentiation of skeletal cells. In this work, the power of multimodal, non-destructive imaging was harnessed, namely CARS, SHG and TPEAF, to establish and detail for the first time a label-free platform for 3D quantitative assessment of human fetal skeletal cell development towards cartilage.

5.3 Methods

All the methodology used in this chapter is detailed in Chapter 3.

5.4 Results and Discussion

To investigate whether label-free, multimodal, non-linear techniques could be used to follow chondrogenic differentiation of skeletal cell populations, human fetal-femur derived skeletal stem/progenitor populations (fetal skeletal cells) were stimulated to differentiate into chondrocytes and generate cartilage tissue in an in vitro 3D pellet culture system over a period of 21 days in chondrogenic medium [155]. To validate chondrogenic development, unstained histological sections of the pellets were imaged for collagen distribution and cellular auto-fluorescence (at 520 nm corresponding to FAD emission). Temporal analysis across the centre of the 3D cartilaginous pellet was performed. Figure 5.1 shows multimodal images of the fetal skeletal cell pellet cultured in chondrogenic conditions for 4, 7, 14 and 21 days. Cellular auto-fluorescence was imaged using TPEAF (blue) and collagen fibres imaged using SHG (green) simultaneously. Pellets were formed by skeletal cell aggregation in chondrogenic media, which starts to form extracellular matrix to provide structural integrity to the bioengineered cartilaginous construct [156, 157]. Using the multimodal

imaging platform developed in our group, SHG enabled the temporal interrogation of chondrogenic differentiation of fetal skeletal cells in pellet culture. SHG allowed high resolution imaging of the concomitant extracellular deposition of fibrillar collagen that proceeds alongside the differentiation of progenitor cells into chondrocytes, as evidenced by the increase in SGH signals and gradual accumulation of collagen fibres over time. Interestingly, the images illustrate that collagen deposition commences from the periphery of the construct and progresses inwards, over time, as the cartilage pellet develops and matures. At day 21 the cartilaginous pellets show secondary structures in the periphery. Although these tissue structures were not investigated in detail, it was observed in all pellets at day 21 during chondrogenic development of human fetal-femur derived skeletal cells, and it was previously detected in similar scaffold-free 3D pellet culture systems [118, 158].

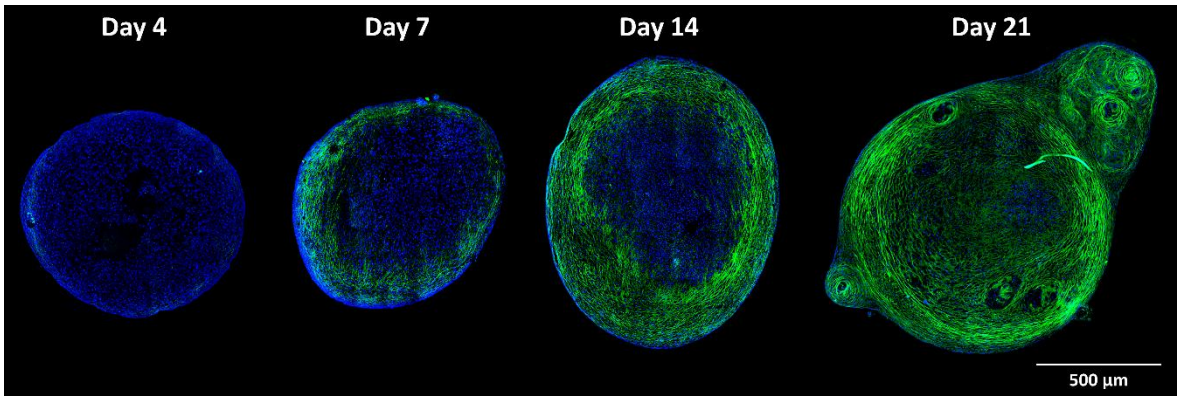

Figure 5.1 – Multimodal imaging of 2D sections of the developing cartilage (paraffin-embedded samples were sectioned using a microtome). Simultaneous imaging of two label-free modalities in human fetal skeletal cell pellets in chondrogenic media over 4, 7, 14, and 21 days of culture. Second harmonic generation (SHG) was used to image collagen fibres in the cartilaginous pellet (green), and two-photon excited autofluorescence (TPEAF) was used visualise cells based on their intrinsic autofluorescence (blue). Scale bar corresponds to 500 µm.

This pattern of collagen deposition can also be observed with conventional stains using histological analysis (Figure 5.2). All sections were counter-stained with Alcian blue to visualise the dense proteoglycan matrix in the cartilage pellets. Sirius red staining showed formation of collagen fibres. Immunohistochemistry revealed expression of collagen Type I and very strong expression of collagen Type II. However, histological stains can bind non-specifically while SHG is selective to non-centrosymmetric super-structures such as Type II collagen [159]. Moreover, SHG provided a spatial resolution of approximately 350 nm which is considerably superior to resolutions observed by transmission/brightfield light microscopy used in histology.

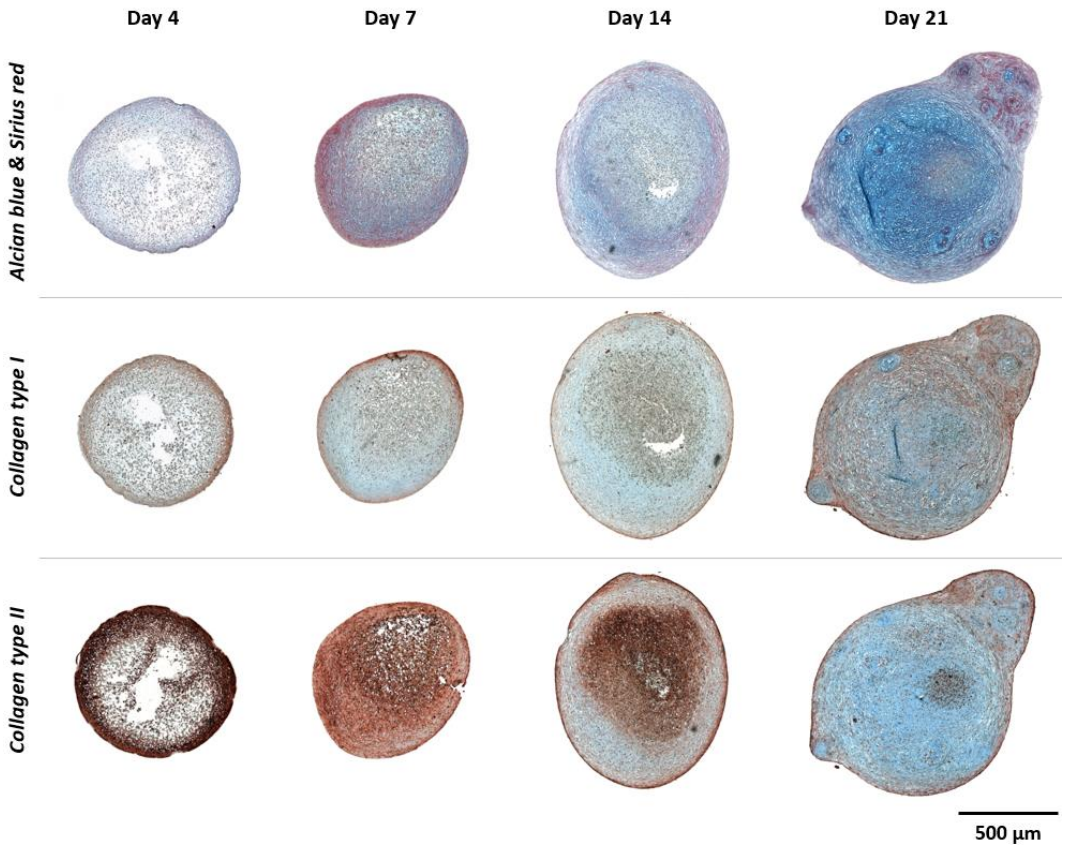

Figure 5.2 – Histological analysis of human fetal skeletal cells cultured in chondrogenic media for 4, 7, 14, and 21 days. All sections were counter-stained with Alcian blue to visualise the dense proteoglycan matrix in the pellets. Sirius red staining showed formation of collagen fibres. Immunohistochemistry (red) revealed expression of collagen Type I and very strong expression of collagen Type II. Scale bar corresponds to 500 µm.

In addition to conventional histological analysis, chondrogenic differentiation of human fetal skeletal cells was also verified by analysis of gene expression using RT-qPCR (Figure 5.3). By day 21 of pellet culture, expression of *SOX9*, the key chondrogenesis transcription factor, *COL2A1*, encoding the α-chain of hyaline cartilage-specific Type II collagen, and *ACAN*, the major proteoglycan in cartilage, were all significantly up-regulated. As cartilage, bone, and marrow fat (adipocytes) are related to each other within the specific stromal developmental process and niche environment, and share a common progenitor (the skeletal stem cell) [14], we also examined the expression profiles of characteristic adipogenic (*PPARG* and *FABP4*) and osteogenic genes (*ALPL* and *COL1A1*) at the corresponding time-points. No significant differences were observed in the temporal expression levels of the adipogenic genes, *PPARG* and *FABP4*. Furthermore, after 21 days of chondrogenic differentiation, no significant difference in *ALPL* expression, a key osteogenic marker, was observed. Although fetal skeletal cell populations demonstrated a modest increase in expression of *COL1A1*, a constituent of fibrocartilage and bone matrix, this was not statistically significant.

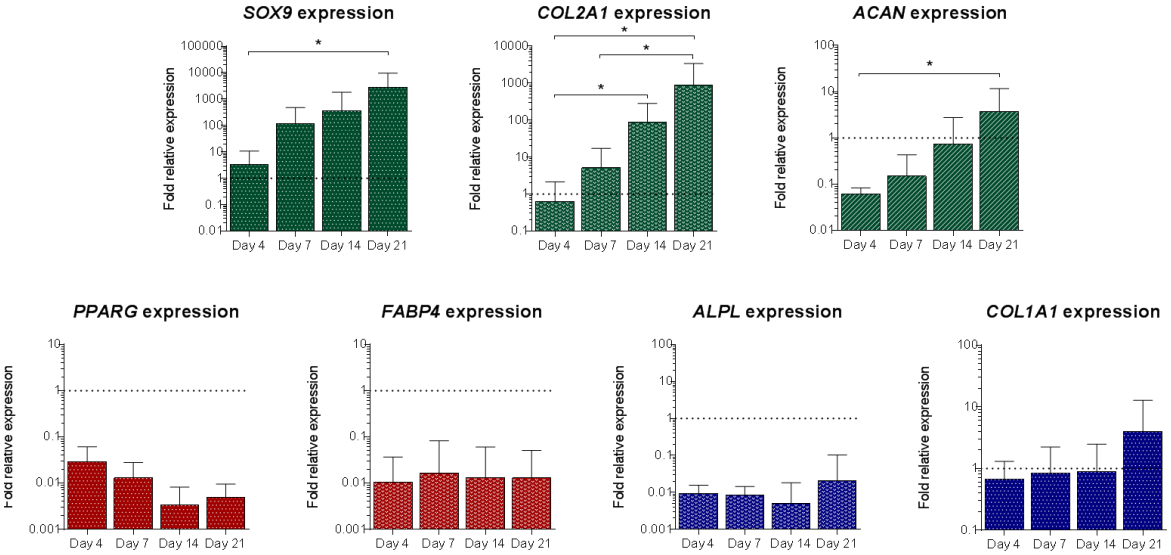

Figure 5.3 – Gene expression analysis. Expression of *SOX9*, *COL2A1*, *ACAN*, *PPARG*, *FABP4*, *ALPL* and *COL1A1* genes in human fetal skeletal cells cultured in chondrogenic media for 4, 7, 14, and 21 days. Relative gene expression was normalized to *ACTB*, and values for gene expression on day 0 were set to one (dotted line). Data represent the average of three independent patient samples plotted and error bars represent standard deviation. **P*<0.05, calculated using Mann–Whitney test.

While 2D imaging of sections of bioengineered tissue can be used for assessment of tissue development by label-free imaging or conventional histological analysis, it is important to recognise that the actual tissue has a complex 3D architecture. Histological analysis necessitates a sample is sectioned using a microtome. In this work, cell pellets were sectioned every 5 µm for histology. Thus, to analyse a 100 µm-thick sample, one would need 20 consecutive 5 µm-sections, assuming no loss of material during sample preparation. In addition, combination of multiple staining procedures simultaneously is challenging, while fixation, sectioning and staining can destroy functionality, potential preclinical evaluation and *in vivo* deployment. Moreover, 2D image analysis can lead to misinterpretation of the results, especially when analysing a system with complex fibril structures such as collagen. Figure 5.4 shows an example of potential misinterpretation following 2D image analysis. When the assessment of collagen content is based on a single image of the tissue-engineered construct, it is possible to infer the presence of either negligible (Figure 5.4-A) or extensive collagen fibres (Figure 5.4-B) in the same cartilaginous construct.

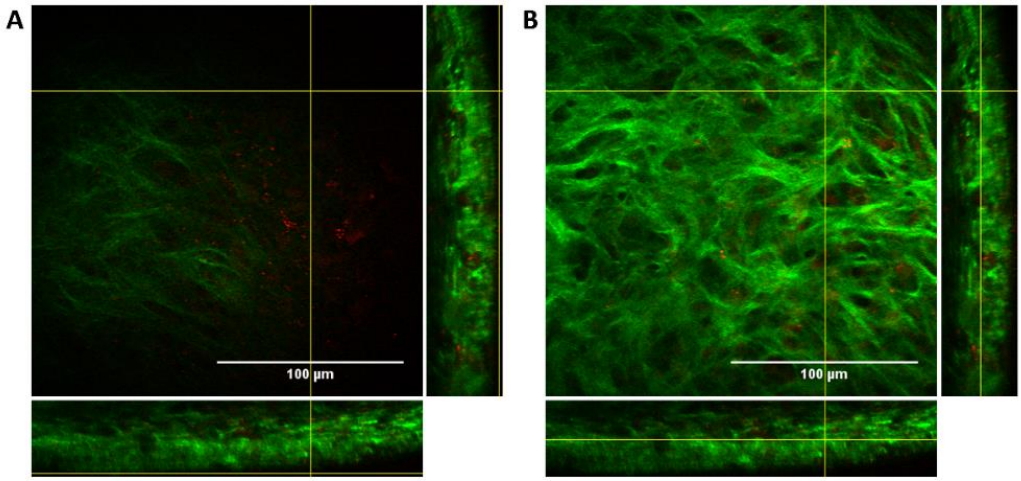

Figure 5.4 – Orthogonal views (xy, xz and yz) of the 3D bioengineered cartilage using multimodal label-free imaging. Second harmonic generation (SHG) identifies collagen fibres (green) and coherent anti-Stokes Raman scattering (CARS) detects lipid droplets within the cartilage pellet (red). Orthogonal views show the intersection planes at the position of the yellow cross-hair. Left and right show two different z views in the same two-dimensional space xy. Scale bars correspond to 100 µm.

Elucidation of the three-dimensional architecture of the bioengineered tissue by non-perturbative 3D imaging is crucial to determine whether the tissue structures are arranged appropriately and, critically, are functional for eventual therapeutic use. Moreover, in addition to imaging the extracellular collagen as a marker for chondrocyte differentiation, it is vital to image cells in a non-invasive, non-destructive manner to obtain a holistic view of cartilage development.

To extend the current work, CARS was combined with SHG and TPEAF in a multimodal platform to image chondrogenesis in 3D. Although CARS has, to date, predominantly been used to image lipid droplets, it can be potentially applied to image other biological components by targeting different vibrational frequencies [151]. Here, CARS microscopy was used to image lipids and cells in 3D in the developing cartilaginous pellet. The CH stretch mode predominant in lipids at 2845 cm^{-1} (Raman spectrum is shown in Figure 5.5) was targeted. This allowed visualisation of the distribution of lipid droplets during chondrogenesis. In an additional innovative step the information provided by CARS imaging was used for visualisation of cells. While lipid droplet distribution is usually ignored during chondrogenesis (possibly due to the lack of visualisation tools), lipids may have an important role informing metabolic activity. Imaging cells in a label-free manner is important to understand and characterise cell-matrix phenotypes, especially in cartilage tissue. Thus, the multimodal combination of CARS with SHG and TPEAF results in a powerful platform for label-free and non-destructive evaluation of chondrogenesis, informing matrix and lipid activity as well as resultant bioengineered cartilage architecture and composition.

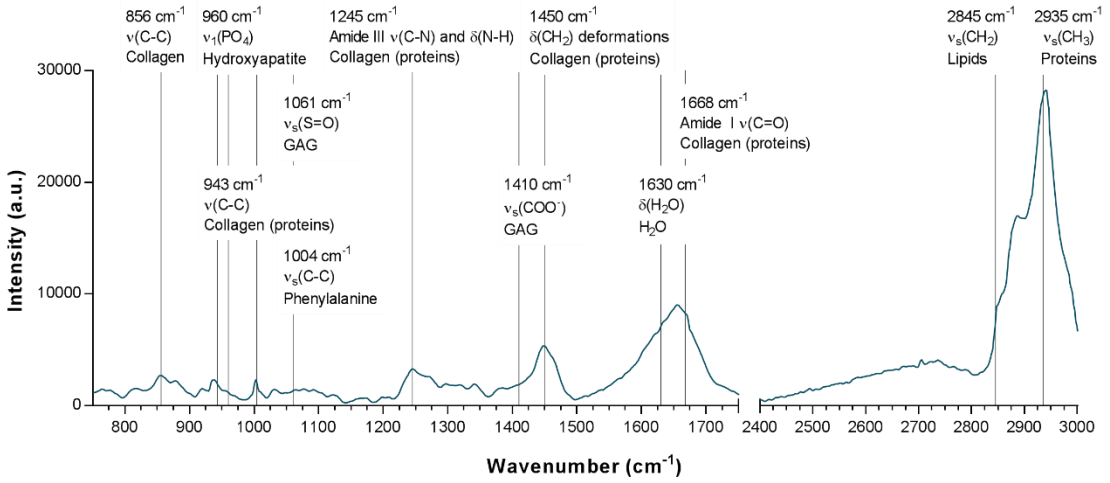

Figure 5.5 – Raman spectrum of human fetal skeletal cells cultured in chondrogenic media for 21 days. The prominent CH stretch mode peak at 2845 cm^{-1} was targeted to image lipids using coherent anti-Stokes Raman scattering (CARS) microscopy.

Figure 5.6 shows 3D multimodal images of fetal skeletal cells cultured in chondrogenic conditions for 4, 7, 14 and 21 days, with maximum intensity z-projections and 3D visualisation of the image stacks. During the chondrogenic differentiation of skeletal cells and subsequent cartilage formation, the collagen fibres (green) were noted to change their shape and configuration. The cartilaginous pellet displayed rich fibrillar collagen from the early stages of differentiation, with cells (blue) distributed throughout the pellet within the network of collagen fibres, reminiscent of native articular cartilage [87]. Additionally, the use of CARS provided information on the distribution of lipid droplets in the cartilaginous pellets (red). This is important, as while glucose is a key source of energy for chondrocytes, lipids within cartilage tissue are also essential for cartilage physiology [160]. Chondrocytes have the ability to synthesise lipids and to harness lipids as an additional source of energy and as structural components and signalling molecules [160, 161]. Figure 5.6 demonstrates that cells synthesise lipids from day 4 of culture throughout the development of cartilage. The gene expression profile of adipogenic genes (*PPARG* and *FAPB4*) demonstrated negligible differences during chondrogenic differentiation (Figure 5.3), indicating that the skeletal cells were not differentiating into adipocytes. However, as indicated above, temporal images of the 3D bioengineered cartilage demonstrate noticeable lipid production by skeletal cells during chondrocyte differentiation and chondrogenic maturation. 3D label-free imaging offers major advantages over standard imaging procedures, and with this detailed label-free approach, a 100 µm-thick sample can be imaged with no sample preparation, and without staining or application of dyes.

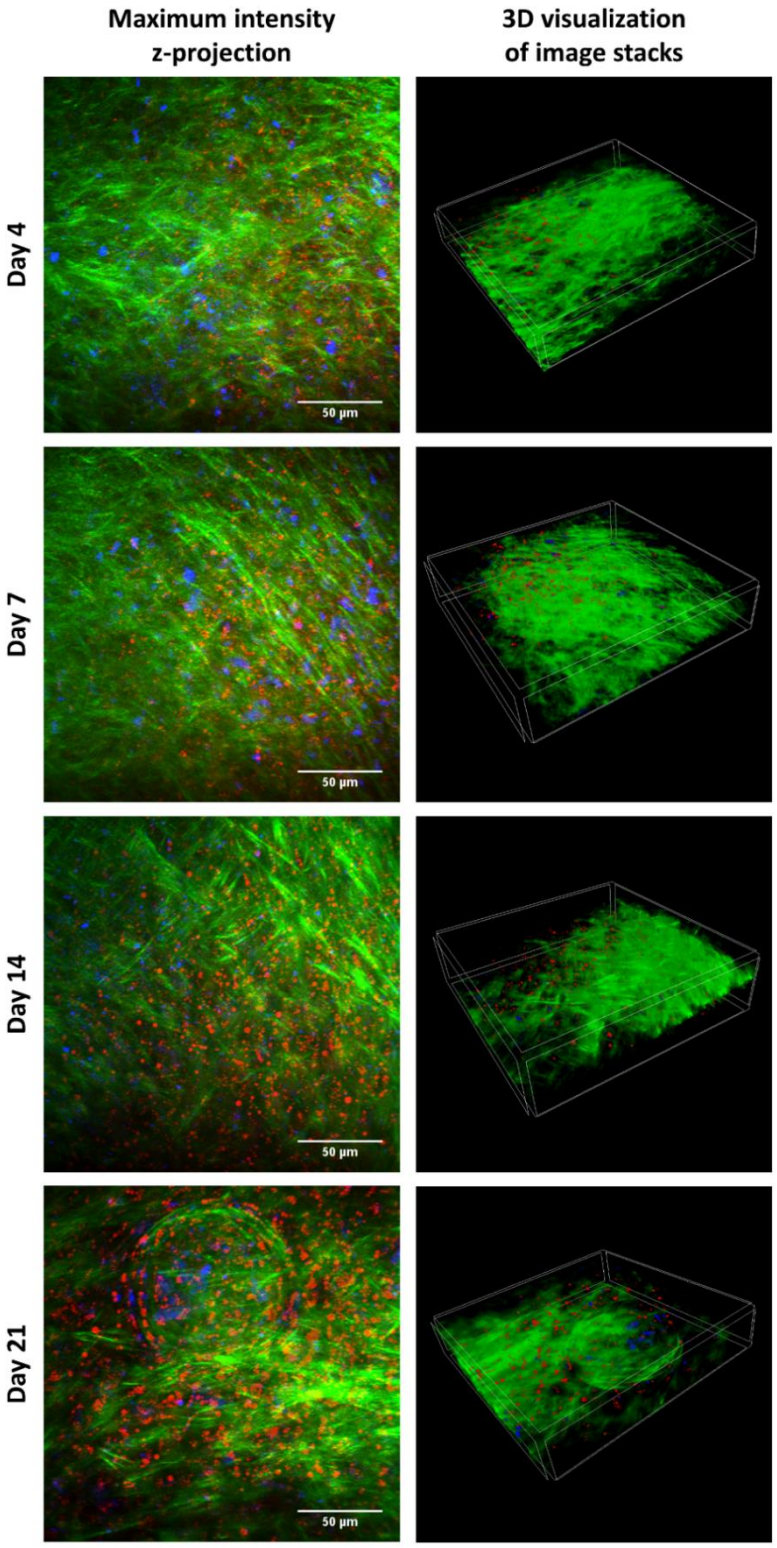

Figure 5.6 – Temporal interrogation of 3D bioengineered cartilage using multimodal label-free imaging. Simultaneous imaging of three label-free modalities in human fetal skeletal cells cultured in chondrogenic media for 4, 7, 14, and 21 days. Second harmonic generation (SHG) identifies collagen fibres (green), coherent anti-Stokes Raman scattering (CARS) detects lipid droplets within the cartilage pellet (red), and two-photon excited autofluorescence (TPEAF) distinguishes the cells using their intrinsic autofluorescence (blue). Maximum intensity z-stack projection is displayed on the left (scale bar corresponds to 50 µm) and the 3D image projection of the cartilage pellet is displayed on the right. Scale bars correspond to 50 µm.

Critically, quantification of the changes during cartilage development using multimodal label-free techniques provides enhanced understanding of fetal skeletal cell chondrogenesis and cartilage growth. The SHG signal of human fetal skeletal cell pellet cultures was analysed using an established image analysis technique that enabled measurement of collagen fibre parameters (CT-FIRE [124]) to determine collagen fibre composition and distribution. Using image analysis, amounts as well as geometric parameters, namely length, width and straightness of each collagen fibre, were extracted from each z-stack image. Image analysis revealed that collagen fibre width did not change significantly during fetal skeletal cell differentiation along the chondrogenic lineage from day 4 to day 21 (Figure 5.7). The measured collagen fibre width was approximately between 2 and 2.5 μm. Published studies indicate that mature collagen fibres assemblies of such fibrils are typically wider than 2 μm [87, 162-164]; this is well within the resolution limit of our multimodal microscope, which is approximately 370 nm, given by the formula 0.7λ/NA [165] (for the 20x magnification objective with 0.75 numerical aperture, as described in section 3.2.13). Quantitation of collagen fibre length over time demonstrated a significant increase in mean length from 22 μm at 4 days to 27 μm at 14 days of chondrogenic culture. There was a modest subsequent decrease at day 21 to give a mean collagen fibre length of 26 μm, indicating that collagen deposition occurs longitudinally (increase in length during cell culture time). Interestingly, there were no significant differences in fibre straightness in cartilaginous pellets of fetal skeletal cells between the different time-points of culture in chondrogenic medium. The trend in these preliminary results is for collagen fibres to become slightly straighter following culture to day 14. These results might indicate that initial deposition up to day 14 occurs by linear extension (length). By increasing the number of samples it would help to better understand any changes in straightness, possibly linked to the spirals of collagen fibres formed in discrete regions as chondrogenic maturation occurred (Figure 5.6).

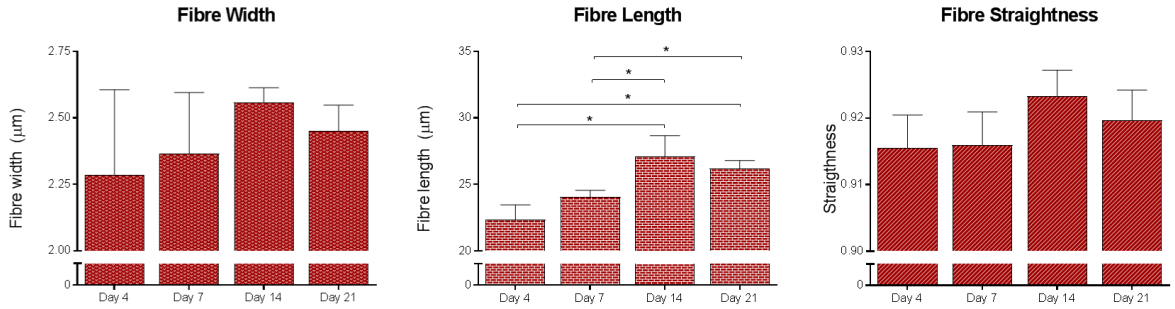

Figure 5.7 – Quantification of collagen fibre width, length and straightness. Second harmonic generation (SHG) 3D images of human fetal skeletal cells cultured in chondrogenic media for 4, 7, 14, and 21 days were analysed using CT-FIRE to extract collagen fibre details. The results are presented as average of three independent patient samples and error bars represent standard error (n=3). **P*=0.05, calculated using Mann–Whitney test.

As pellet cultures provide an optimal 3D environment for robust cartilage development, the quantitative cell analysis was extended to 3D imaging. Cell quantification is essential to understand cell-matrix interactions as, in combination with collagen quantification, it can yield an analytical parameter for evaluating the cartilage phenotype. The cells were counted using CARS images incorporating a modification of 3D particle analysis function in Fiji. Although not statistically significant (n=3 patients) there is an increase in the number of cells per unit volume in fetal skeletal cell pellets cultured under chondrogenic conditions for 7 days before cell numbers decreased (Figure 5.8). Interestingly, the corresponding mean cell size per unit volume was also increased. Given that the overall size of the chondrocytic pellet increased, these observations indicate enhanced cell proliferation up to day 7 after which the cells grow in size. This individual increase in size of each cell accompanied by a decrease in cell numbers per unit volume indicates differentiation (collagen and proteoglycan formation typical of the chondrocytic phenotype) and enhanced extracellular matrix production resulting in an overall increase in size of the cartilage pellet.

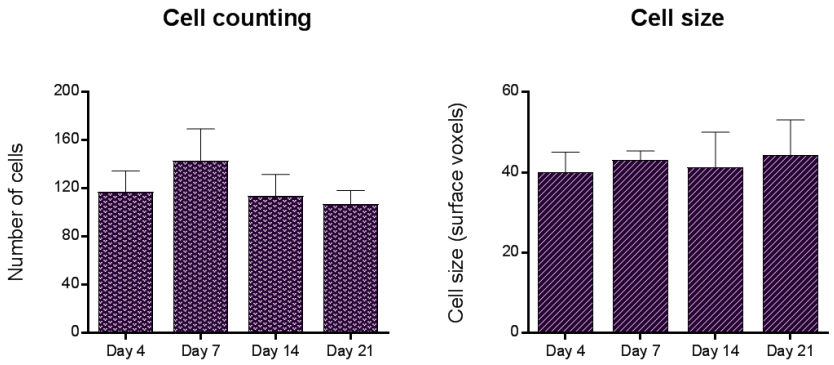

Figure 5.8 – Cell analysis using 3D coherent anti-Stokes Raman scattering (CARS) imaging. CARS 3D images of human fetal skeletal cell pellets cultured in chondrogenic media for 4, 7, 14, and 21 days were analysed using Fiji to analyse cell number and size in volumes of interest for each cartilage pellet. Cell counting is presented as average of cell counting per volume of interest, and cell size is presented as average of the mode per volume of interest. All experiments were performed using three different human fetal skeletal cell samples. Error bars represent standard error and there were no statistically significant differences (P>0.05, calculated using ANOVA with Tukey's post-hoc test [cell counting] and Mann–Whitney test [cell size], according to the Shapiro-Wilk test for normal distribution).

In addition, image analysis offered the potential to calculate the amount of collagen fibres present in the same volume of interest to determine collagen production and cell number as a consequence of development of the cartilage tissue in the pellet (Figure 5.9). The number of cells was observed to decline after day 7, possibly associated with the fact that in a confined volume where the collagen fibre amount increases (Figure 5.9) and a modest increase in cell size was observed (Figure 5.8), there is limited space for additional cells in the same volume. Therefore, a new assessment parameter of collagen per cell (CpC) was defined, which captures the net balance between collagen deposition and proliferation of cells. While this needs further evaluation on a larger patient cohort, preliminarily studies using fetal skeletal cells from 3 subjects indicate a switch in chondrogenic differentiation from a proliferative state to a collagen-rich expansion state, suggesting that this parameter can be used to characterise a phenotypic change in chondrogenesis based on cell-matrix organisation. The use of this quantitative parameter could provide an important understanding in assessing the health/phenotype of bioengineered cartilage and measuring the effect of environmental and chemical modulators on engineered tissue.

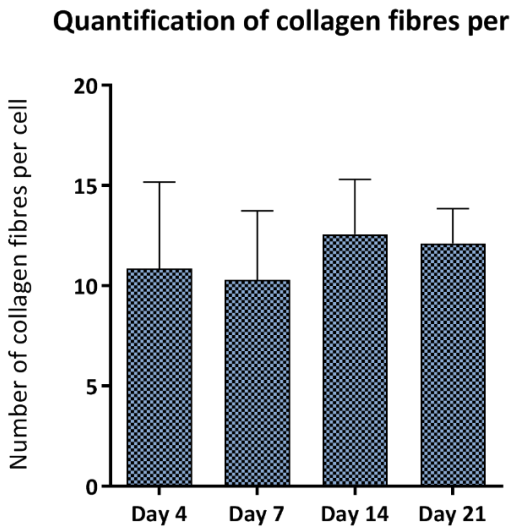

Figure 5.9 – Cartilage differentiation assessment parameter. 3D image analysis allows to quantify the collagen amount per cell (CpC) in a volume of interest. Data generated indicate the ability to combine different image analysis tools to chronological assess the number of collagen fibres produced per number of cell (CpC) in bioengineered cartilage using human fetal skeletal cells.

The multimodal combination of CARS microscopy with SHG and TPEAF, with integrated quantitative 3D imaging analysis, offers unparalleled insight into the chondrogenic differentiation of human fetal skeletal progenitor and stem cell populations. Retrieval of 3D information using non-destructive approaches offers tissue engineers new platform technologies to follow the formation of new regenerated tissues, as well as new tools for stem cell biologists studying health and disease with 3D cartilage models in real-time.

5.5 Conclusions

In conclusion, in this current chapter, quantitative 3D multimodal label-free imaging was applied, offering a non-invasive and non-destructive platform for the analysis of chondrogenic differentiation of human fetal skeletal cell populations, and enabling elucidation of temporal changes in cartilage development. Quantitative analysis of collagen and cells through a multimodal microscope (combining CARS, SHG and TPEAF), yield parameters to objectively assess cartilage development. A new parameter based on quantitative analysis, collagen per cell or CpC, allows to capture the interplay between matrix deposition and cellular proliferation as the bioengineered tissue develops over time. Such non-perturbative label-free analysis in 3D is essential for development of the field of human skeletal repair and regeneration research, with significant impact for tissue engineering and regenerative medicine applications.

6

THREE-DIMENSIONAL, NON-DESTRUCTIVE, LIVE-CELL IMAGING OF BIOENGINEERED CARTILAGE TISSUE USING MULTIMODAL NON-LINEAR MICROSCOPY

Chapter 6 presents work to be submitted to the peer-reviewed journal Nature Communications: "Three-dimensional, non-destructive, live-cell imaging of bioengineered cartilage tissue using multimodal non-linear microscopy", Catarina Costa Moura, Konstantinos N. Bourdakos, Rahul S. Tare, Richard O. C. Oreffo, Sumeet Mahajan.

Contributions: CC Moura performed cell culture, imaging, molecular lab work, Raman spectroscopy, data analysis, image processing and analysis, statistical analysis and participated in the design of the study. S Mahajan and KN Bourdakos designed the multimodal microscopy system, and KN Bourdakos carried out the construction and set-up. RS Tare, ROC Oreffo and S Mahajan conceptualised, designed and coordinated the study. All authors contributed to the writing of the manuscript and gave final approval for publication.

6.1 Abstract

CARS microscopy is a label-free imaging technique and is usually referred to as a non-destructive and non-invasive method. Although live-cell imaging studies have been performed previously, less is known about the effect of CARS microscopy at the molecular level during cell differentiation and tissue development. In this chapter, the differentiation of human fetal-femur derived skeletal cells into cartilage in three-dimensional cultures was monitored using CARS and SHG microscopy. The work detailed in this chapter shows that, by using suitable acquisition parameters, live cell imaging of the same 3D tissue is possible over time. Moreover, this study conclusively establishes that non-linear label-free imaging does not alter the molecular signatures at the different stages of cartilage development and has no adverse effect on the skeletal cell growth/behaviour. Additionally, CARS microscopy revealed to be suitable to image additional molecules of interest, such as lipids, proteins and glycosaminoglycans, in bioengineered cartilage tissue. The label-free and truly non-invasive nature of live CARS and SHG imaging provides an ideal tool to monitor human skeletal cell cartilage development. This study demonstrates the immense value and translation potential of label-free multimodal imaging approaches and their application to human skeletal regeneration research and tissue engineering.

6.2 Introduction

Tissue engineering has been described as the application of scientific methods to produce 'spare parts' of the body for replacement of damaged or lost organs [13, 166, 167]. Skeletal tissue engineering seeks to address the growing need for skeletal tissue augmentation or repair through the generation of functional skeletal tissue by the recapitulation of stem cell developmental processes. A major challenge in Orthopaedics is the regeneration of articular cartilage and the application of cell-based restorative and reparative surgical techniques for articular cartilage repair [168, 169]. Human skeletal cell populations offer significant potential as a cell source for tissue engineering applications, and in particular for skeletal tissue regeneration strategies [2, 143]. The development of appropriate tools to follow skeletal cell development and monitor the formation of newly engineered neocartilage in real-time, non-invasively or non-destructively is crucial and remains, to date, an unmet goal.

CARS microscopy is a powerful chemical imaging technique that maps the distribution of molecules in biological systems in their native state, without the need for an external label (such as stains or fluorophores) [34]. The label-free nature of CARS

microscopy, together with its inherent three-dimensional imaging capability [170], present an exciting imaging tool for biomedical and clinical applications. Since sample preparation and processing are not required, live-cell imaging using CARS microscopes has become a reality [171-173]. As with all optical techniques, power and exposure to light need to be within a threshold to prevent any cell damage and phototoxic effects. However, with CARS microscopy, a number of questions remain as to whether: i) live-cell imaging using CARS microscopy is fully non-invasive; ii) cell development remains unaltered; and iii) the cells remain viable and robust for further use in clinical applications following live cell monitoring with CARS microscopy. Studies have reported on thresholds of photo-induced cell damage by CARS microscopy, commonly by visualising direct cell morphological changes [174], and detecting formation of apoptotic membrane protrusions [175], or by analysing and comparing nuclear staining between damaged and non-damaged cells after laser exposure [176]. The induced damage and changes are obvious at the levels of damage thresholds. For non-linear techniques such as CARS and SHG, given that relatively high peak powers are used, it is necessary to establish that no subtle changes are induced that are detrimental to the biological system under study (even if the laser powers are within damage thresholds). SHG is a well-established technique that allows imaging of collagen fibres in tissues [80], and can be carried out simultaneously with CARS with appropriate laser sources.

Currently, there are no known studies detailing live cell state or cell development in two- or three-dimensional cultures over time using CARS imaging. Critically, there has been no investigation, to date, detailing the potential biological effects on using non-linear imaging techniques such as CARS and SHG on live tissue when the excitation powers are well within damage thresholds. This is essential to establish CARS and related non-linear imaging techniques as mainstream analytical or assessment tools in biomedicine and, more specifically, in skeletal repair and regeneration strategies. The application of robust, real-time, temporal, non-invasive imaging is relevant for tissue engineering, in particular, to ensure the absence of tissue and cell deterioration over time and to investigate appropriate tissue development at the molecular-level. The current work examines these issues with analysis of the development of human fetal femur-derived skeletal cells into cartilage, and attempts to conclusively establish through gene expression analysis and concomitant imaging that under appropriate conditions the non-linear imaging during cell differentiation (carried out over 21 days) has no observed effect.

Lipids remain the molecule of choice in most studies for imaging using CARS, given the role of lipids in metabolism and their strong Raman signal due to CH-

stretching vibrations [152]. More recently, the potential of CARS microscopy for imaging other relevant biological molecules such as phosphate in hydroxyapatite [177, 178], or nucleic acids and proteins [178, 179], has attracted significant interest. In the second part of this chapter, this challenge is addressed, and the ability of CARS microscopy to image relevant molecules, namely proteins and glycosaminoglycans, in the bioengineered cartilage tissue is demonstrated.

6.3 Methods

All the methodology used in this chapter is detailed in Chapter 3.

6.4 Results and Discussion

The differentiation of human fetal-femur derived skeletal cells into cartilage in three-dimensional cultures was analysed using live-cell CARS and SHG microscopy. Human fetal skeletal cells were cultured in an *in vitro* three-dimensional pellet culture system over a period of 21 days in chondrogenic medium to differentiate into chondrocytes and generate cartilage tissue (Figure 6.1). Cartilaginous pellets were formed by skeletal cell aggregation in chondrogenic media. The initiation of extracellular matrix production provides structural integrity to the bioengineered construct. In order to establish that live imaging by CARS and SHG does not affect the development of the bioengineered cartilage the following experiment was designed.

Three different conditions using human skeletal cells derived from the same fetal sample were examined: i) cells cultured over 21 days in absence of live-cell imaging (control); ii) cells cultured over 21 days and live-cell imaging performed at day 7; and iii) cells cultured over 21 days and live-cell imaging performed at day 7 and day 21 (Figure 6.1). Fetal skeletal cells were imaged in real-time under identical culture and chondrogenic environment as the control. For all the three conditions, skeletal lineage-specific gene expression was analysed.

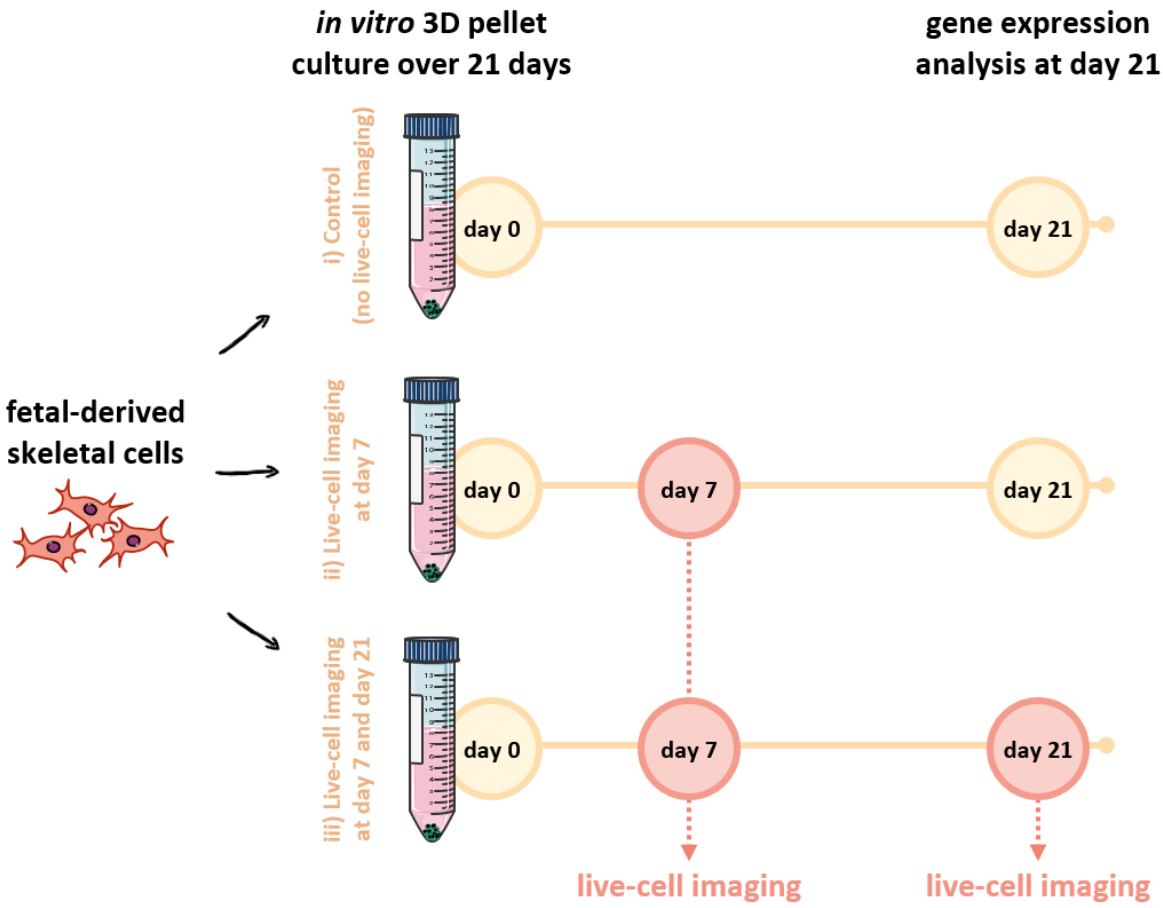

Figure 6.1 – Schematic diagram of the experimental design. Human fetal femur-derived skeletal cells were cultured in an in vitro three-dimensional pellet culture system over a period of 21 days in chondrogenic medium. From the same fetal sample: i) cells were cultured over 21 days in the absence of live-cell imaging (control); ii) cells were cultured over 21 days and live-cell imaging performed at day 7; and iii) cells were cultured over 21 days and live-cell imaging performed at day 7 and day 21. The expression of skeletal lineage-specific genes after 21 days in chondrogenic culture was analysed for all three conditions.

Live-cell imaging of chondrogenic differentiation of skeletal cell populations was performed using a label-free, multimodal, non-linear imaging platform, combining CARS and SHG microscopy (Figure 6.2a). The laser power required for the live-cell imaging procedure to be used in fetal femur-derived skeletal cells without compromising the pellet structure was approximately 120 mW. The optimisation protocol is detailed in Experimental section 3.2.14.1.

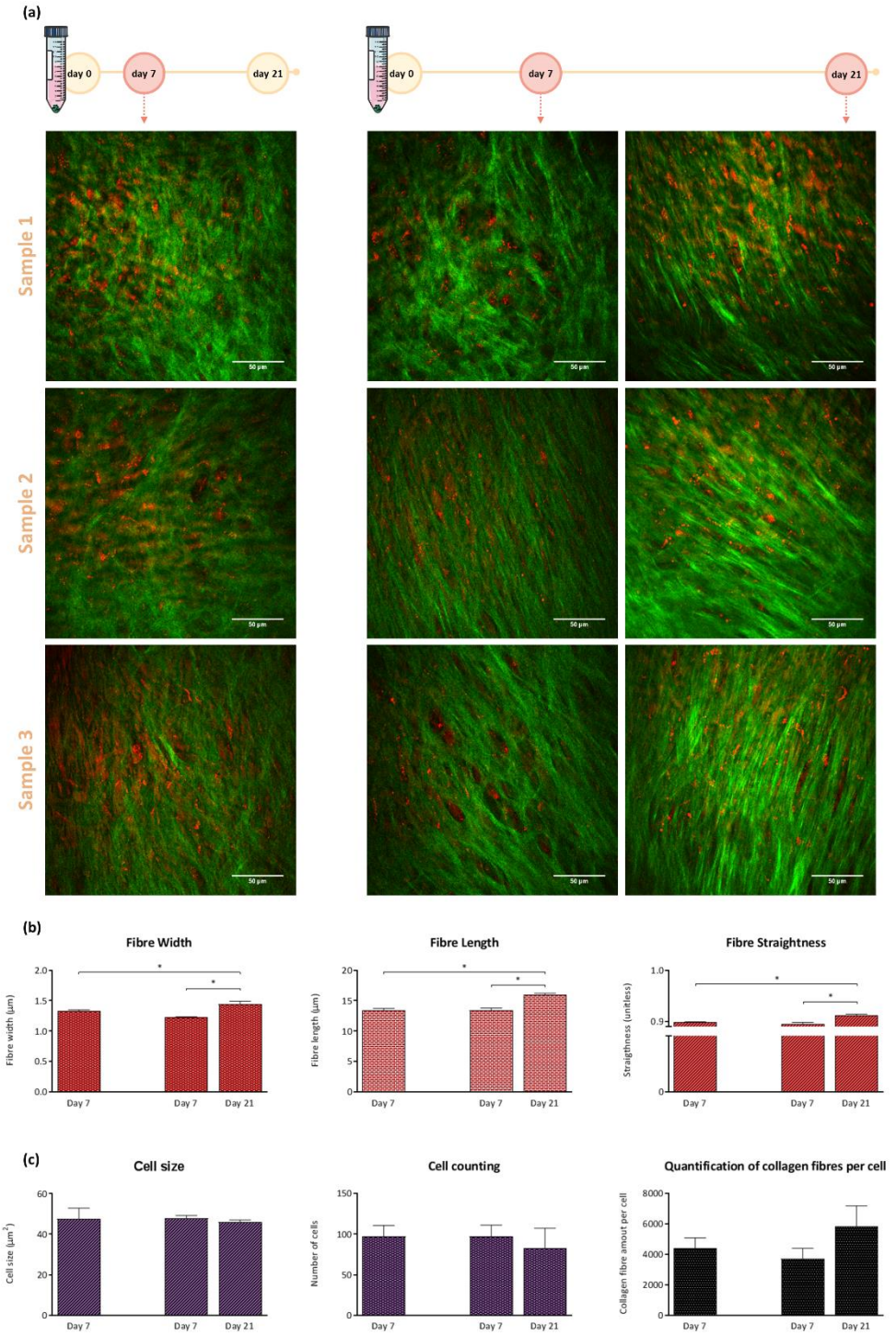

Figure 6.2 – (a) Label-free live-cell imaging at day 7 and day 21 in human fetal femur-derived skeletal cell pellets maintained in chondrogenic media over 21 days of culture. Second harmonic generation (SHG) identified collagen fibres (green) and coherent anti-Stokes Raman scattering (CARS) detected lipid droplets within the cartilage pellet (red). Scale bars correspond to 50 µm. (b) Quantification of collagen fibre width, length and straightness. SHG signal was analysed using CT-FIRE to extract collagen fibre details. (c) CARS images were analysed using Fiji to quantity cell number and size for each cartilage pellet. Quantification of collagen per cell was measured combining SHG and CARS data analysis to assess the amount of collagen fibres produced per number of cell in the bioengineered cartilage tissue. Average of three independent fetal samples; error bars represent standard deviation. *P<0.05 calculated using Mann-Whitney test.

SHG enabled imaging of collagen fibres within the 3D cartilage pellet, providing a comprehensive structural information on the collagen fibre network without using labels. CARS microscopy allowed the visualisation of the lipid distribution during chondrogenesis. At different time-points, all samples were equivalent and presented comparable collagen and lipid patterns. Quantification of the image analysis data sets (Figure 6.2b) demonstrated that collagen fibres increase significantly in width, length and straightness, from day 7 to day 21 of chondrogenic culture. No statistically significant differences in cell size and cell number between the different days of culture, at the same field of view, were observed (Figure 6.2c). Image analysis enabled measurement of the number of collagen fibres present in the same area of interest, to quantify collagen production and cell number during development of the cartilage tissue in the pellet. An increase from day 7 to day 21 in the net balance between collagen deposition and proliferation of fetal skeletal cells was observed (Figure 6.2c).

Gene expression was analysed using RT-qPCR to compare the three different conditions detailed in Figure 6.3. Characteristic chondrogenic genes *COL2A1*, which encodes the α-chain of hyaline cartilage-specific Type II collagen, and *ACAN*, the major proteoglycan in cartilage, were up-regulated in fetal skeletal cells following 21 days of chondrogenic culture (Figure 6.3). *COL10A1*, which encodes the α-chain of Type X collagen expressed by hypertrophic chondrocytes, and *SOX9*, the chondrogenic transcription factor, were negligibly expressed after 21 days of culture (gene amplification only detected beyond 30 cycles). Furthermore, a down-regulation of characteristic osteogenic (*ALPL*) and adipogenic (PPARG and FABP4) genes after 21 days of chondrogenic differentiation were observed (Figure 6.3).

Crucially, analysis across the three human fetal skeletal cell culture conditions (control, live-cell imaging at day 7, and live-cell imaging at day 7 and 21) indicated no significant differences in the chondrogenic gene expression levels. Comparison against the control demonstrated that live-cell imaging procedure with CARS and SHG microscopy, either imaged at one single early time-point (day 7) or two distinct time-points (day 7 and day 21), did not restrict or affect chondrogenic differentiation and development of the cartilage tissue at the molecular level. Label-free multimodal imaging offers a singular tool for stem cell biologists to study tissue repair and regeneration in real-time, non-destructively and non-invasively.

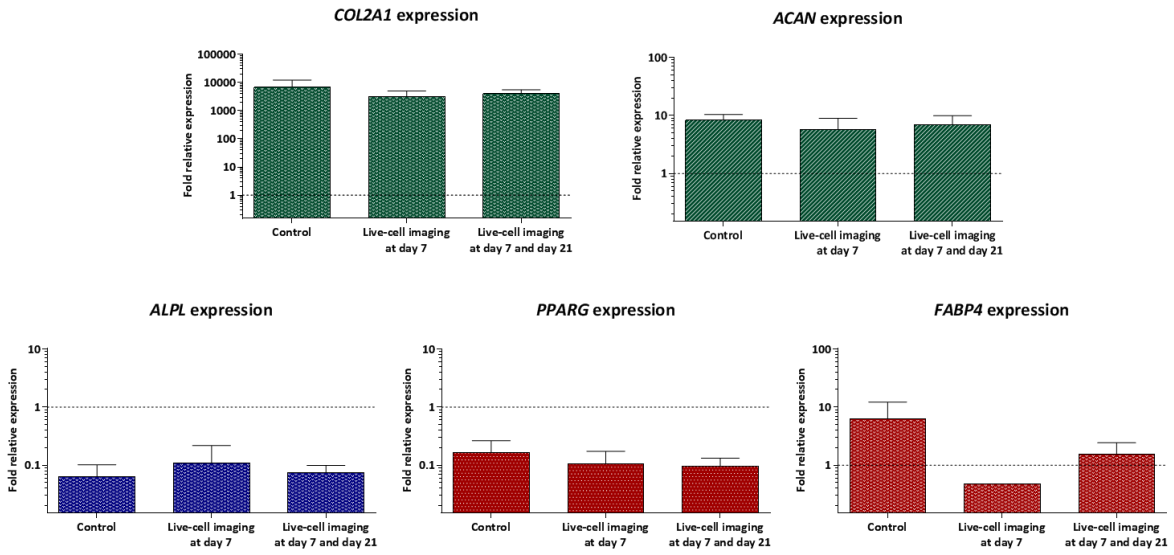

Figure 6.3 – Expression of *COL2A1*, *ACAN*, *ALPL*, *PPARG* and *FABP4* in human fetal femur-derived skeletal cells cultured in chondrogenic media at day 21, including control (cells cultured with no live-cell imaging), cells cultured over 21 days and live-cell imaging performed at day 7, and cells cultured over 21 days and live-cell imaging performed at both days 7 and 21. Relative gene expression was normalised to *ACTB*, and values for gene expression on day 0 were set to one (dotted line). Average of three independent fetal samples; error bars represent standard deviation. **P*<0.05 calculated using Mann-Whitney test.

After monitoring the differentiation of human fetal femur-derived skeletal cells into cartilage in three-dimensional cultures for 21 days, the potential of the multimodal label-free system to image other relevant molecules in the cartilage tissue was investigated. CARS microscopy is commonly applied to image molecules in the CH stretch region of the Raman spectrum (2840-3000 cm^{-1}), such as lipids and cell membranes, important in tissue and cellular analysis [180]. The Raman spectrum of the cartilage tissue in the CH-stretch region was acquired (Figure 6.4a). Images from lipids in the cell pellets were captured by targeting the Raman CH stretching mode at 2845 cm^{1} (CH_2 symmetric stretch) [152, 181], and the SHG signal was simultaneously acquired (Figure 6.4b and Figure 6.4c). The pump beam used for CARS imaging also served as the SHG excitation source (with a separate detection channel). Furthermore, label-free images of proteins within the cartilage construct (Figure 6.4c) were collected by targeting the vibrational modes at 2935 cm^{-1} (CH_3 symmetric stretch) and 3030 cm^{-1} (CH_3 asymmetric stretch) [181]. This was performed sequentially by tuning the pump beam to target the corresponding vibrational frequencies. Similar structures can be observed by targeting different vibrational modes (Figure 6.4). Although the 2935 cm^{-1} vibration mode is commonly assigned to proteins, lipids also have CH_3 moieties that will be detected using CARS microscopy. As CARS provides the chemical distribution of a particular vibrational mode one can observe different molecules at a particular

frequency. Specifically, the multimodal imaging system used in this work has a spectral resolution of approximately 10 cm^{-1} and there is no 'bleed-through' in the different channels.

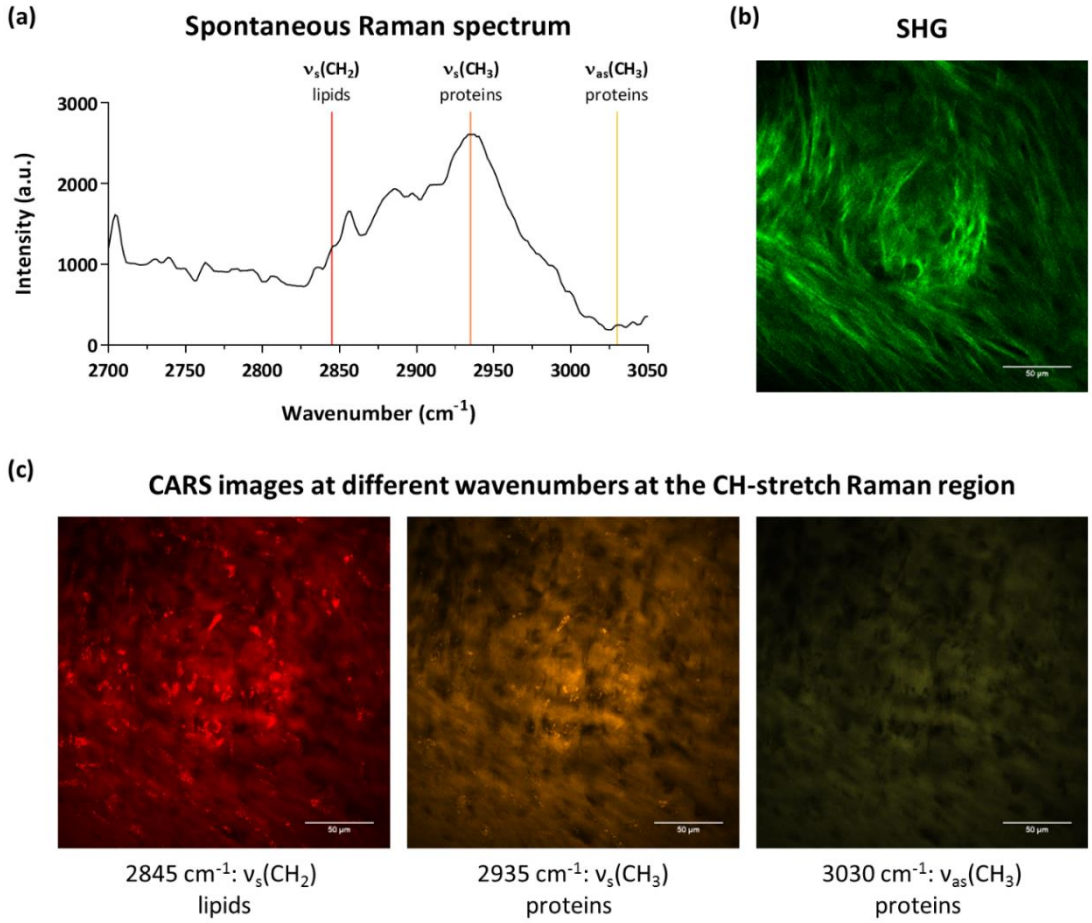

Figure 6.4 – Human fetal femur-derived skeletal cells were cultured in an *in vitro* three-dimensional pellet culture system over 21 days in chondrogenic media to generate cartilage tissue. (a) Raman spectrum at the CH-stretch region. The three marked bands were targeted for coherent anti-Stokes Raman scattering (CARS) imaging. (b) Second harmonic generation (SHG) shows collagen fibres (green) in the bioengineered cartilage tissue. (c) CARS images of the bioengineered cartilage tissue at the CH-stretch region: 2845 cm^{-1} ($\nu_s(CH_2)$), 2935 cm^{-1} ($\nu_s(CH_3)$), and 3030 cm^{-1} ($\nu_{as}(CH_3)$). Scale bars correspond to 50 µm.

Although extensive work has been undertaken employing CARS imaging in the CH stretch region of the Raman spectrum, imaging on the spectral region between 800 cm^{-1} and 1800 cm^{-1} using CARS microscopes has received less attention. This spectral Raman region, the so-called 'fingerprint' region, is rich in biochemical information including chemical functional groups related to tissue proteins, lipids, glycogen and nucleic acids (Figure 6.5a). Articular cartilage consists primarily of extracellular matrix, such as collagens, proteoglycans and non-collagenous proteins, and a sparse population of chondrocytes. Proteoglycans have an important role in the cartilage

matrix and are composed of a protein core and one or more glycosaminoglycan chains, which hold negatively charged carboxylate or sulphate groups [86]. The Raman band at 1061 cm^{-1} is typical from glycosaminoglycans with sulphate groups (OSO^{3-} symmetric stretch) [182], and by targeting this vibrational mode glycosaminoglycans can be imaged using CARS microscopy (Figure 6.5b). Additionally, the amide I band at 1668 cm^{-1} is mainly assigned to collagen [182-184], and in Figure 6.5b CARS signal from both fibrillar and non-fibrillar collagen can be observed. The Raman CH vibrational mode at 1450 cm^{1} (CH_2/CH_3) is related to collagen/proteins [182-184], and although slightly different one can observe the similarities between the 1450 cm^{1} and 1668 cm^{-1} signals. CARS images at different vibrational frequencies acquired from replicate samples are shown in Figure 6.6.

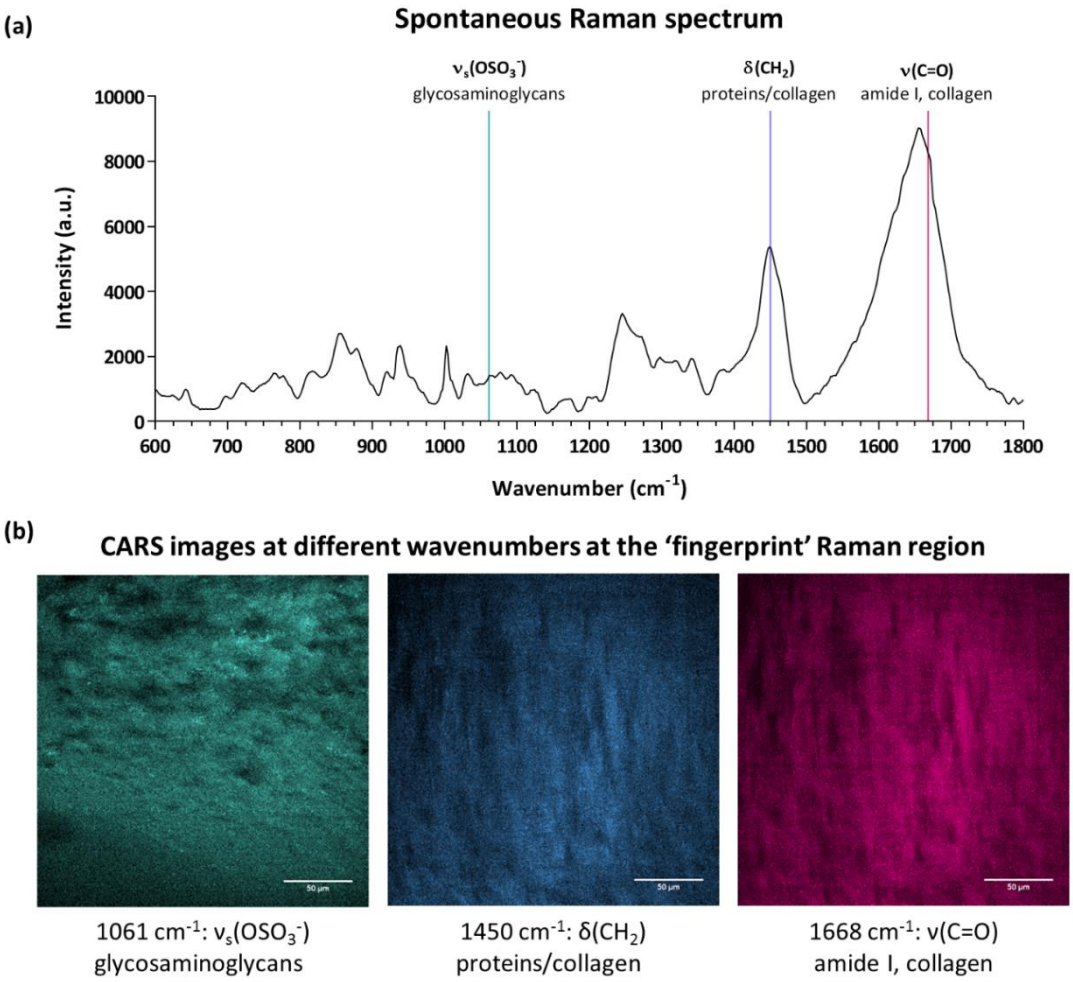

Figure 6.5 – Human fetal femur-derived skeletal cells were cultured in an *in vitro* three-dimensional pellet culture system over 21 days in chondrogenic media to generate cartilage tissue. (a) Raman spectrum at the 'fingerprint' region. The three marked bands were targeted for coherent anti-Stokes Raman scattering (CARS) imaging. (b) CARS images of the bioengineered cartilage tissue at the 'fingerprint' vibrations: 1061 cm^{-1} ($\nu_s(OSO_3^-)$), 1450 cm^{-1} ($\delta(CH_2)$), and 1668 cm^{-1} ($\nu(C=O)$). Scale bars correspond to 50 μm.

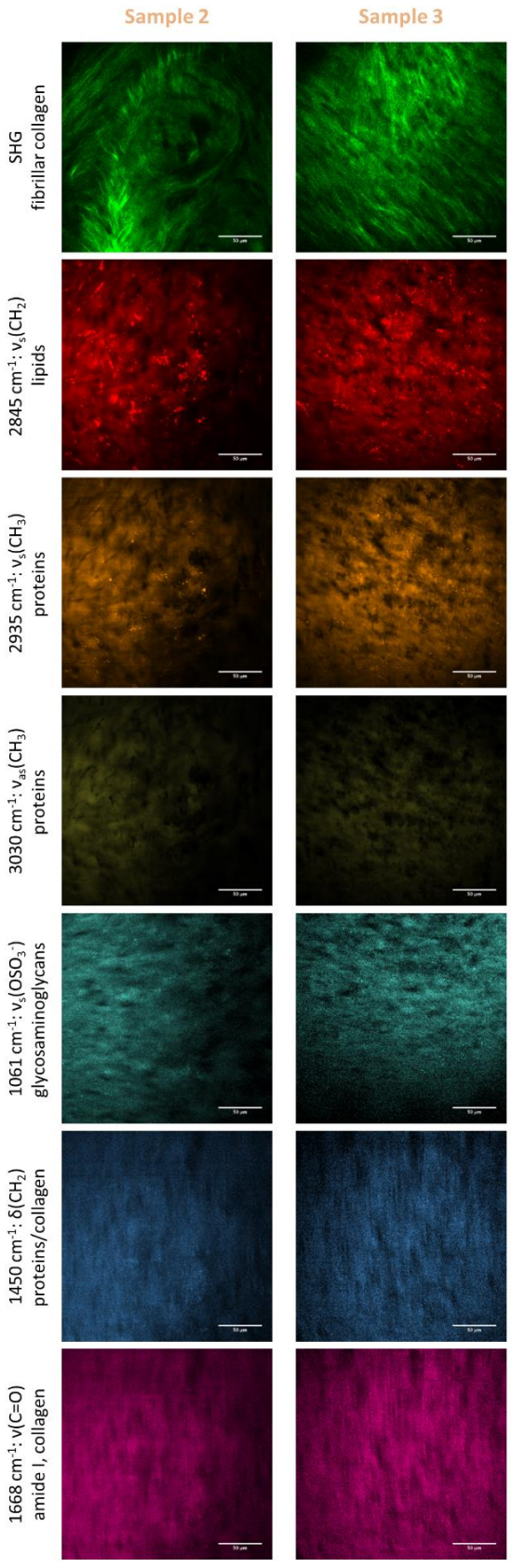

Figure 6.6 – Second harmonic generation (SHG) and coherent anti-Stokes Raman scattering (CARS) images from bioengineered cartilage tissue (replicate samples). Human fetal femur-derived skeletal cells were cultured in an *in vitro* three-dimensional pellet culture system over 21 days in chondrogenic media to generate cartilage tissue. Scale bars correspond to 50 µm. Colour scale was normalised between images within the same Raman region (CH-stretch or fingerprint).

It has not escaped my attention that the field of view was changing when imaging the same sample at different frequencies (Figure 6.7). This change in field of view was a consequence of modifying the short pass dichroic excitation filter in the home-built multimodal imaging system according to the selected wavenumber (Table A.1 in Appendix A.1 shows the different filters used).

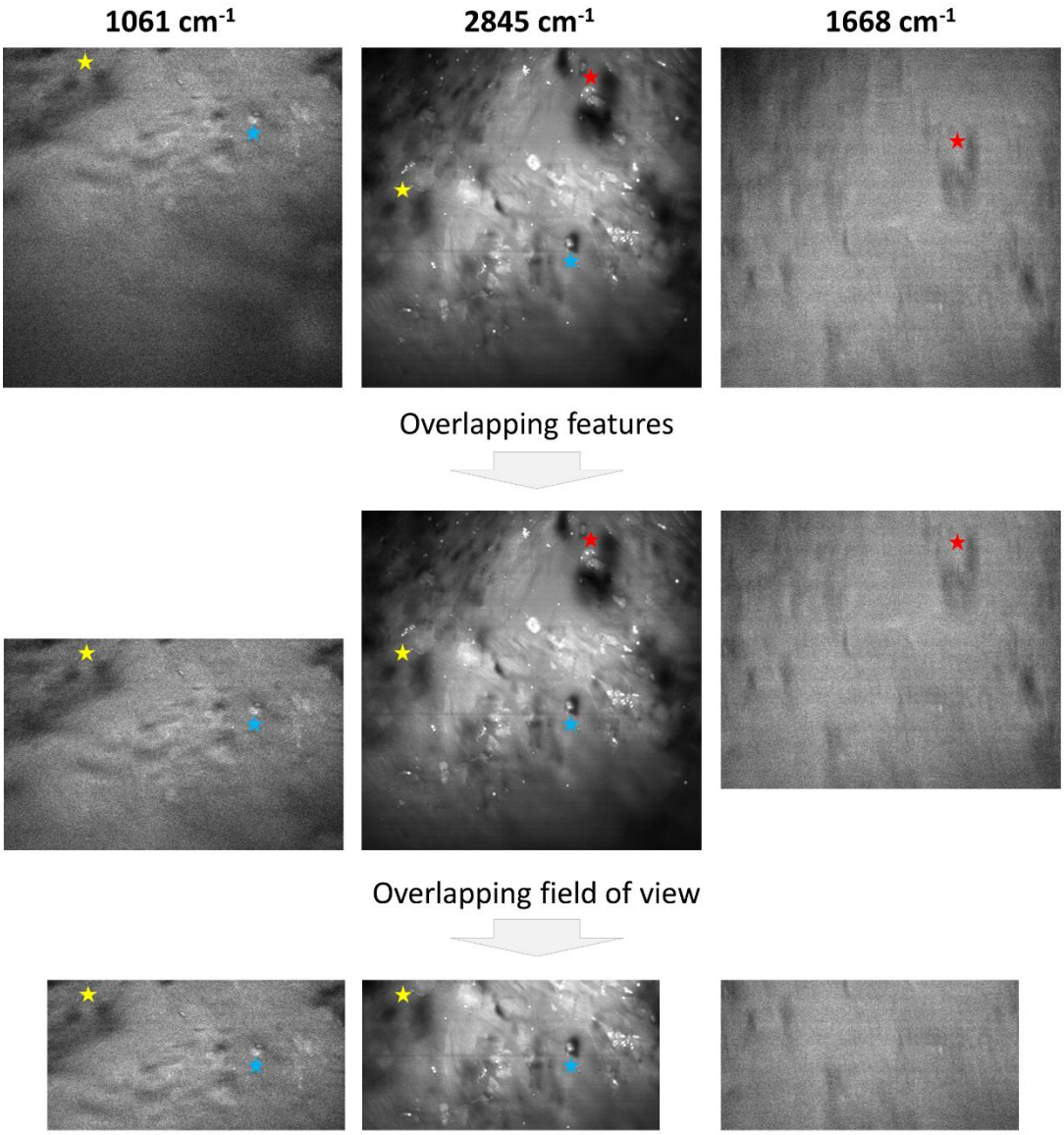

Figure 6.7 – CARS images show different fields of view depending on the selected wavenumber. This change in field of view was a consequence of modifying the short pass dichroic excitation filter in the home-built multimodal imaging system (the different filters used in this work can be consulted in Table A.1 in Appendix A.1).

Interestingly, CARS imaging at the 1668 cm^{-1} Raman band displays a distinct and different signal of collagen compared to SHG. In fact, while CARS is responsive to the molecular structure and chemical composition, in this case proteins that are predominantly collagens, SHG is sensitive to the supermolecular crystalline structure of collagen [58, 185]. Thus, the home-built label-free multimodal system allowed

acquisition of information on collagen by examining the CARS signal at 1668 cm^{-1} band and on fibrillar collagen by analysing the SHG signal (after field of view correction), highlighting the potential of a multimodal label-free imaging system equipped with non-linear techniques such as CARS and SHG as a powerful monitoring tool in tissue engineering (Figure 6.8),.

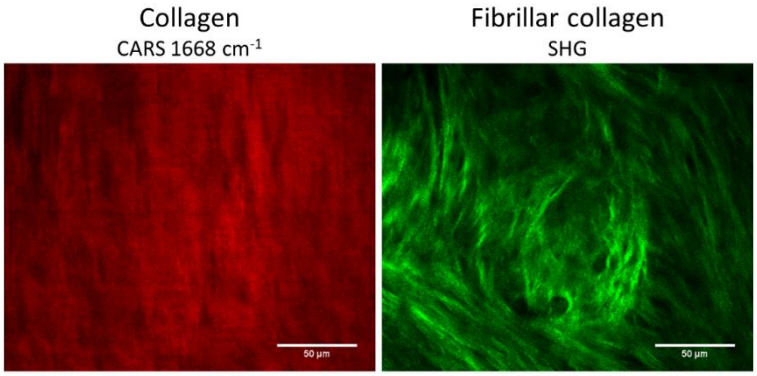

Figure 6.8 – Coherent anti-Stokes Raman scattering (CARS) signal at 1668 cm^{-1}, mainly assigned to collagen, and SHG signal, revealing fibrillar collagen on the bioengineered cartilage tissue.

6.5 Conclusions

In summary, the current studies have investigated the use of label-free imaging techniques, namely CARS and SHG microscopy, in live human fetal-femur derived skeletal cells differentiated into chondrogenic cultures. Although high peak powers from pulsed lasers are used to acquire CARS images, these results demonstrate that under damage thresholds label-free CARS live-cell imaging at the molecular level had negligible effect on human fetal skeletal cell differentiation and development to cartilage, as confirmed by gene expression analysis. The laser power used for the live-cell imaging of fetal femur-derived skeletal cells was approximately 120 mW, without compromising cell differentiation and cartilage development. Furthermore, it was demonstrated that CARS microscopy is a suitable platform to image additional key molecules of interest, with bioengineered cartilage tissue imaged at different wavenumbers corresponding to different vibrational frequencies to acquire CARS signal from lipids, proteins and glycosaminoglycans.

The ability to dynamically follow the formation of new regenerated tissues in real-time using a non-invasive technique offers exciting opportunities for the design and development of innovative tissue engineering solutions for hard and soft tissues. This study indicates that multimodal imaging with non-linear techniques such as CARS and SHG offer new approaches for clinical translation assessment of regenerated skeletal tissues, and are ready for widespread implementation by biomedical scientists.

7

FUTURE DIRECTIONS FOR RESEARCH

Chapter 7 presents indications for further investigations and discusses future directions on multimodal label-free imaging in skeletal cell research.

7.1 Indications for further experiments

7.1.1 Tracking adipogenic differentiation of human fetal femur-derived skeletal cells

In Chapter 4, it was demonstrated that CARS imaging provides an ideal alternative to monitor human adult SSC differentiation into adipocytes, non-destructively and without using any label. After evaluating the potential of CARS microscopy to study adipogenic differentiation of adult SSCs, a similar study using fetal femur-derived skeletal cells was performed.

Raman spectra were obtained by focussing on large lipid droplets in fetal femur-derived skeletal cells cultured after adipogenic differentiation for 14 days. A representative spectrum is shown in Figure 7.1. Similar to the previous experiment with adult SSCs, the CH stretch mode peak at 2845 cm^{-1} was targeted to image lipids using CARS microscopy.

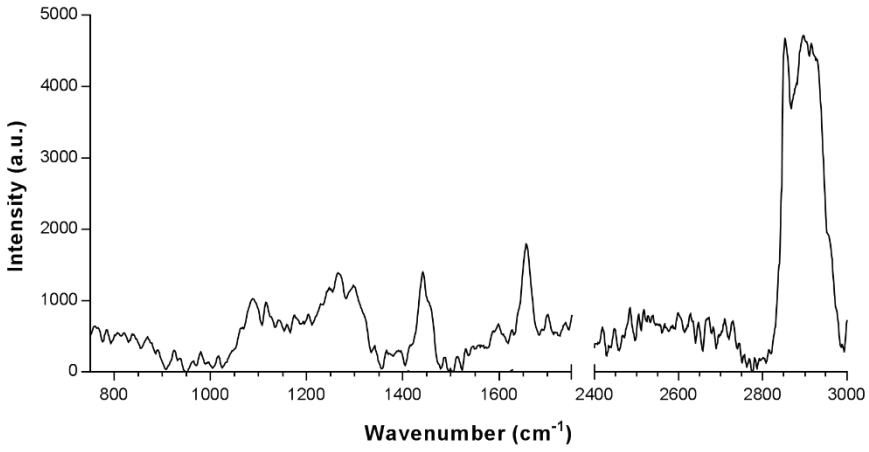

Figure 7.1 – Raman spectra of differentiated (adipogenic media) fetal femur-derived skeletal cells (laser 633 nm, 0.6 mW power). The spectrum from cells cultured for 14 days in adipogenic media was acquired by directly focussing on the lipid droplets. The prominent CH stretch mode peak at 2845 cm^{-1} was targeted to image lipids using coherent anti-Stokes Raman scattering (CARS) microscopy.

Oil Red O staining and CARS images of fetal femur-derived skeletal cells cultured in adipogenic media show the accumulation of lipid droplets after 14 days of differentiation (Figure 7.2). When cultured in basal media, fetal-femur derived skeletal cells display very few lipid droplets and do not show an increase after 14 days of culture (Figure 7.2).

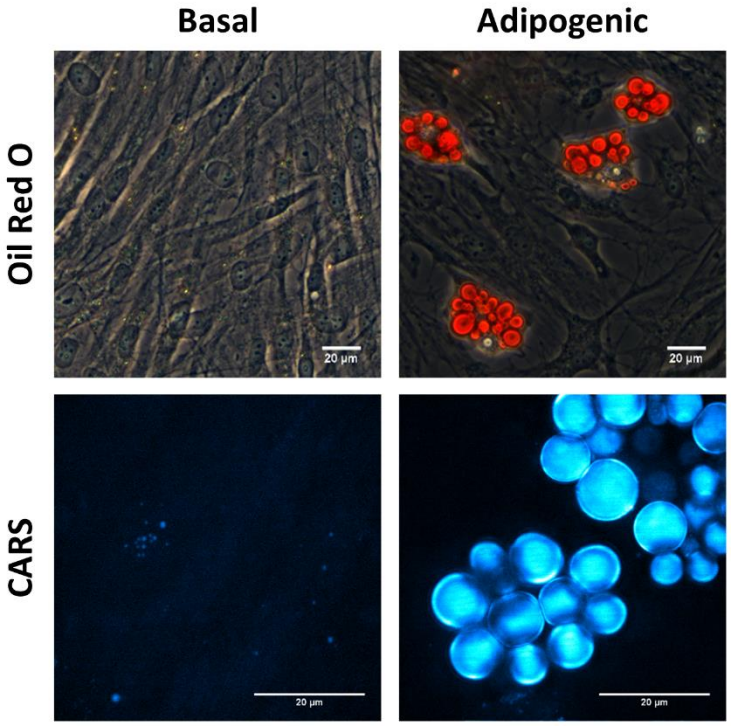

Figure 7.2 – Comparison of Oil Red O staining and label-free coherent anti-Stokes Raman scattering (CARS) imaging to assay adipogenic differentiation of fetal femur-derived skeletal cells (cultured in adipogenic media for 14 days). Scale bars correspond to 20 µm.

The differentiation of fetal femur-derived skeletal cells into adipocytes was validated by qPCR analysis. *PPARG* and *FABP4* expression, as well as *ALPL*, *COL1A1*, and *COL2A1*, were examined at day 1, 3, 4, 7, and 14. Figure 7.3 shows the gene expression profile of human fetal femur-derived skeletal cells cultured in basal and adipogenic media. *PPARG*, *FABP4*, *ALPL*, and *COL1A1* expression in fetal femur-derived skeletal cells show a similar pattern to adult SSCs, when cultured in either basal or adipogenic media. However, when cultured in adipogenic media, human fetal femur-derived skeletal cells have a significant up-regulation of *COL2A1* in every time-point from day 1 to day 14. The up-regulation of *COL2A1* was not observed in adult SSCs when cultured in adipogenic media conditions (Figure 7.4).

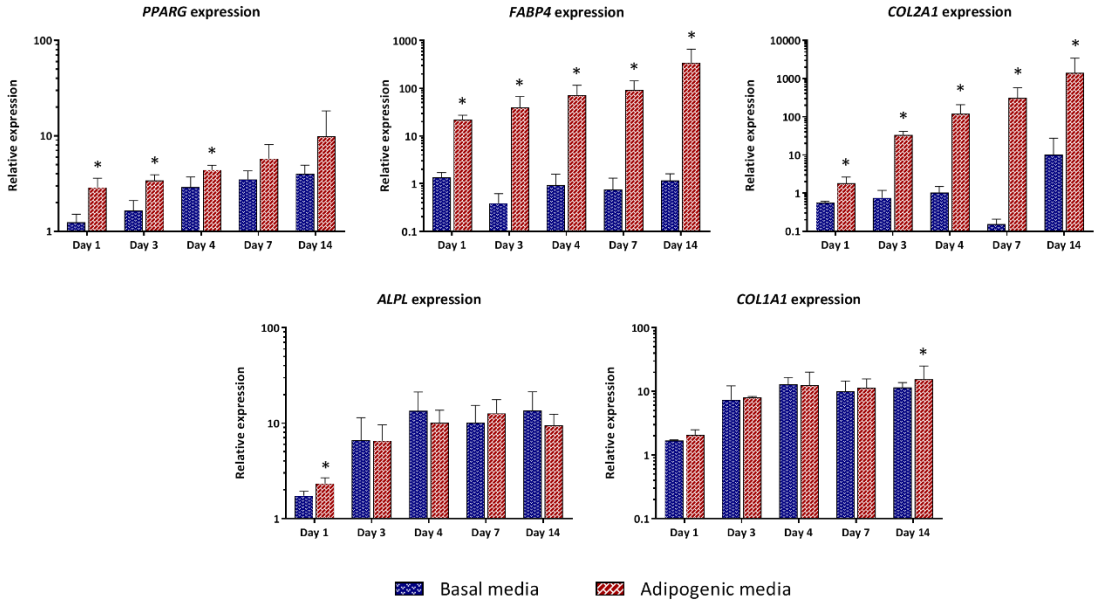

Figure 7.3 – Expression of *PPARG*, *FABP4*, *COL2A1*, *ALPL*, and *COL1A1* in human fetal femur-derived skeletal cells cultured in basal and adipogenic media for 1, 3, 4, 7, and 14 days. Relative gene expression was normalised to ACTB, and values for gene expression on day 0 were set to one. Average of three independent fetal samples; error bars represent standard deviation. **P*<0.05 calculated using Mann-Whitney test.

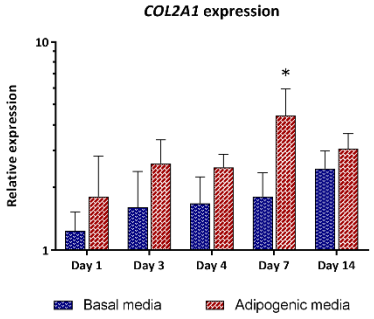

Figure 7.4 – Expression of *COL2A1* in human adult skeletal stem cells (SSCs) cultured in basal and adipogenic media for 1, 3, 4, 7, and 14 days. Relative gene expression was normalised to ACTB, and values for gene expression on day 0 were set to one. Average of three independent patient samples; error bars represent standard deviation. **P*<0.05 calculated using Mann-Whitney test.

Although the three different skeletal lineages – osteogenic, chondrogenic and adipogenic – share some stages in the SSC differentiation pathway, the up-regulation of *COL2A1* in adipogenesis was not expected, as *COL2A1* encodes Type II collagen, the hyaline cartilage-specific collagen [158]. It is necessary to further understand the role or the relationship of Type II collagen in adipogenic differentiation of human fetal-femur derived skeletal cells, or to optimise *in vitro* differentiation protocols. In this thesis CARS imaging was shown to be a good imaging alternative to monitor SSC differentiation in real-time, non-invasively and non-destructively; thus CARS could be an invaluable tool to address this question.

7.1.2 Label-free diagnostics of skeletal diseases

Osteoarthritis and osteoporosis are two common age-related musculoskeletal disorders which cause disability in the majority of the elderly population affected. The application of label-free and non-invasive tools to investigate potential bone markers in early osteoarthritis or osteoporosis could have a large impact in skeletal disease diagnostics and prognostics.

Histological analysis of bone samples is a valuable clinical and research tool. In order to prepare good-quality paraffin sections and preserve all the essential microscopic elements, decalcification is required to remove mineral from bone tissue. However, decalcification is performed after sample fixation and most commonly requires long incubation times. In some preliminary work, an osteoarthritic femoral head sample was prepared. The methodology used in this section is available in Appendix A.2. The method to determine the end-point of decalcification is to X-ray the specimen, as the final radiographic image reveals any residual calcium deposits. In this particular osteoarthritic femoral head sample, the end-point of decalcification was after 12 weeks (Figure 7.5), resulting in very long processing time and laborious work.

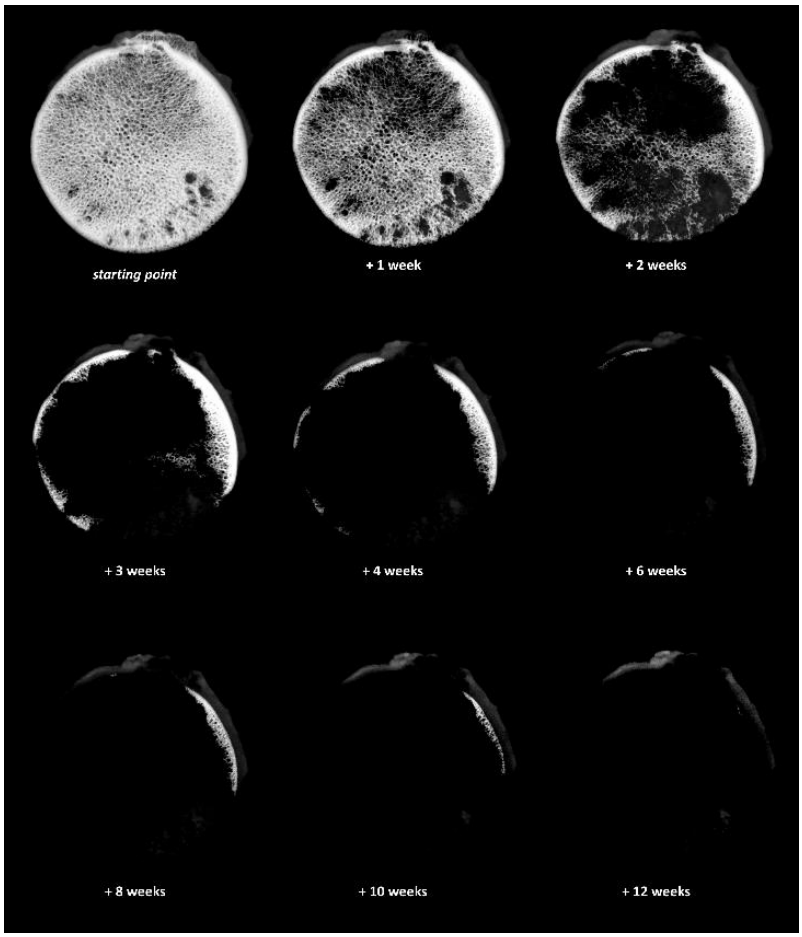

Figure 7.5 – An X-ray series following the process of decalcification of an osteoarthritic femoral head slice sample. The radiographs were imaged using a Faxitron® MX-20 and allowed to determine the end-point of decalcification.

Finding skeletal disease markers using label-free techniques would allow research and clinical studies with shorter duration, and potentially supporting the diagnostics process. Raman spectra of a fixed osteoarthritic femoral head slice display constituents attributed to mineralised tissue including phosphate/hydroxyapatite, amide I and amide III (Figure 7.6). It is possible to detect changes in characteristic Raman peaks in different areas of the femoral head sample, related to the distinct biochemical composition (bone/cartilage).

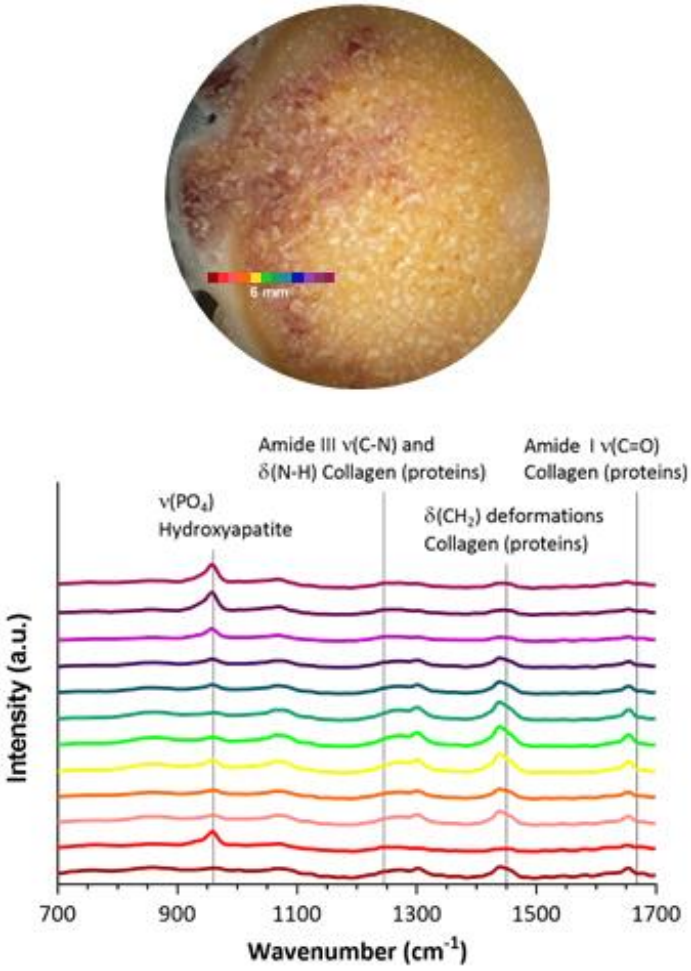

Figure 7.6 – Raman spectra of different regions of an osteoarthritic femoral head sample.

Additionally, analysis of human bone samples with multimodal imaging could also provide more information on how bone/cartilage structure change in skeletal diseases. Figure 7.7 shows an example of multimodal label-free microscopy on an osteoarthritic femoral head slice, comprising SHG and TPEAF imaging. SHG could be used to image collagen fibres (green) and to deliver information on how the structure relates to the mechanical properties on bone/cartilage and what changes occur in osteoarthritis.

These preliminary data suggest Raman spectroscopy and multimodal label-free imaging as potential tools to describe signatures of healthy/diseased skeletal tissue samples and offer enhanced information to indicate early changes regarding the phenotype of skeletal tissue. Other research groups have also been working in this direction [107, 186]. Further investigations on label-free characterisation of bone and cartilage samples might open new areas of research and diagnostics in skeletal health and disease.

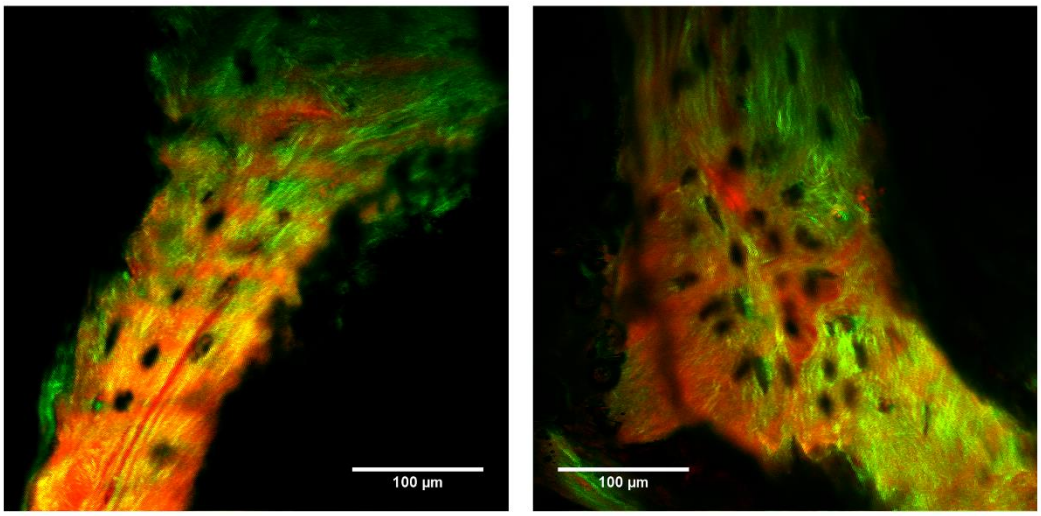

Figure 7.7 – Example of non-destructive label-free imaging of an osteoarthritic femoral head sample. Two-photon excited auto-fluorescence (TPEAF) and second harmonic generation (SHG) signals, represented in red and green respectively, could be used to provide information on how the structure relates to the mechanical properties on bone/cartilage and what changes occur in osteoarthritis.

7.2 Outlook

Non-destructive and non-invasive, chemically and structurally selective, label-free imaging techniques are now being recognised as advantageous methodologies for SSC assessment in research studies, for evaluation and monitoring of new bone and cartilage formation, or even for applications in reparative and regenerative medicine.

For multimodal CARS imaging to be used as a routine technique several technological hurdles still need to be overcome. The majority of CARS applications were performed imaging at a single vibrational frequency, and to date only a couple of biomolecules are typically visualised using CARS microscopy given the limitations related to the availability of broadband laser sources. To surmount this limitation, broadband CARS technologies are being developed, where multiple Raman frequencies are imaged simultaneously [187]. It should also be mentioned that in CARS the signal is proportional to the square of the concentration of vibrational oscillators, hence for

low quantities of biomolecules, CARS sensitivity considerably decreases and imaging becomes more challenging [24, 68]. Another issue is the non-resonant background observed in CARS imaging which can decrease signal to noise ratio. Potentially, these disadvantages can be addressed by using a similar coherent Raman technique named stimulated Raman scattering (reviewed in Zhang *et al.* 2014 [188], and Cheng *et al.* 2015 [189]), though it still faces many similar challenges as CARS [189, 190]. Furthermore, CARS microscopy remains relatively expensive in comparison to other characterisation techniques and requires sophisticated instrumentation. CARS microscopy is now commercialised by Leica Microsystems [191], but further developments are still required to make the technique more accessible. High-quality imaging systems will need to be built using affordable components, to enable and enhance uptake and application of this technique.

On a different note, while Raman probes are in advanced stage of translation, application of multimodal CARS through optical fibres is still in its infancy. The development of special fibres that can handle laser pulses used in CARS, SHG and TPEAF, and that have large bandwidth and low distortion, is an active area of research [192].

In summary, while promising multimodal label-free imaging still does not provide the simplicity offered by many established characterisation techniques for skeletal regeneration for routine use. For adoption of CARS, SHG and TPEAF imaging in the clinic, in addition to overcoming the technological hurdles, it will also be necessary to: i) standardise protocols (sample preparation, data analysis and presentation, *etc.*), ii) perform multicentre studies, iii) provide cost rationale/justification for the national health systems, and iv) provide specific training to clinicians (reviewed in Sulé-Suso *et al.* [108]). Nevertheless, only by acknowledgement of the relative strengths/weaknesses and current challenges can a step change occur in methodologies to monitor the differentiation of SSCs in their natural state, and indeed other stem and progenitor populations in other tissues.

The research findings discussed in this thesis provide a strong case for the use of multimodal label-free imaging techniques for skeletal cell characterisation. The non-destructive and non-invasive nature of CARS and SHG microscopy present an exciting prospective alternative to dynamically monitor SSC development for skeletal regeneration, with widespread potential in other hard and soft tissues.

Appendix

A.1 CARS imaging at different wavenumbers

Table A.1 – CARS signal for different Raman peaks and the corresponding modifications in the multimodal label-free imaging set up (Stokes laser at 1032 nm).

Raman peak	Pump laser	CARS signal	Excitation filter	Interference filters	
			short pass dichroic	*short pass*	*band pass*
1000 cm^{-1}	935.5 nm	855.4 nm	875 nm	no filter	857/30 nm
1020 cm^{-1}	933.7 nm	852.5 nm	875 nm	no filter	857/30 nm
1040 cm^{-1}	932.0 nm	849.6 nm	875 nm	no filter	857/30 nm
1060 cm^{-1}	930.2 nm	846.8 nm	875 nm	no filter	840/12 nm
1080 cm^{-1}	928.5 nm	843.9 nm	875 nm	no filter	840/12 nm
1100 cm^{-1}	926.8 nm	841.1 nm	875 nm	no filter	840/12 nm
1120 cm^{-1}	925.1 nm	838.2 nm	875 nm	no filter	840/12 nm
1140 cm^{-1}	923.4 nm	835.4 nm	875 nm	no filter	840/12 nm
1160 cm^{-1}	921.7 nm	832.6 nm	875 nm	no filter	840/12 nm
1180 cm^{-1}	920.0 nm	829.9 nm	875 nm	no filter	820/12 nm
1200 cm^{-1}	918.3 nm	827.1 nm	875 nm	no filter	820/12 nm
1220 cm^{-1}	916.6 nm	824.4 nm	875 nm	no filter	820/12 nm
1240 cm^{-1}	914.9 nm	821.7 nm	825 nm	no filter	820/12 nm
1260 cm^{-1}	913.2 nm	819.0 nm	825 nm	no filter	820/12 nm
1280 cm^{-1}	911.6 nm	816.3 nm	825 nm	no filter	820/12 nm
1300 cm^{-1}	909.9 nm	813.7 nm	825 nm	no filter	820/12 nm
1320 cm^{-1}	908.3 nm	811.0 nm	825 nm	no filter	820/12 nm
1340 cm^{-1}	906.6 nm	808.4 nm	825 nm	no filter	800/12 nm
1360 cm^{-1}	905 nm	805.8 nm	825 nm	no filter	800/12 nm
1380 cm^{-1}	903.4 nm	803.2 nm	825 nm	no filter	800/12 nm
1400 cm^{-1}	901.7 nm	800.7 nm	825 nm	no filter	800/12 nm

1420 cm^{-1}	900.1 nm	798.1 nm	825 nm	800 nm	800/12 nm
1440 cm^{-1}	898.5 nm	795.6 nm	825 nm	800 nm	800/12 nm
1460 cm^{-1}	896.9 nm	793.0 nm	825 nm	800 nm	800/12 nm
1480 cm^{-1}	895.3 nm	790.5 nm	825 nm	800 nm	800/12 nm
1500 cm^{-1}	891.7 nm	788.0 nm	825 nm	800 nm	780/12 nm
1520 cm^{-1}	892.1 nm	785.6 nm	825 nm	800 nm	780/12 nm
1540 cm^{-1}	890.5 nm	783.1 nm	825 nm	800 nm	780/12 nm
1560 cm^{-1}	888.9 nm	780.6 nm	825 nm	800 nm	780/12 nm
1580 cm^{-1}	887.3 nm	778.2 nm	825 nm	800 nm	780/12 nm
1600 cm^{-1}	885.8 nm	775.8 nm	825 nm	800 nm	780/12 nm
1620 cm^{-1}	884.2 nm	773.4 nm	825 nm	800 nm	766/13 nm
1640 cm^{-1}	882.6 nm	771.0 nm	825 nm	800 nm	766/13 nm
1660 cm^{-1}	881.1 nm	768.6 nm	825 nm	800 nm	766/13 nm
1680 cm^{-1}	879.5 nm	766.3 nm	825 nm	800 nm	766/13 nm
2820 cm^{-1}	799.3 nm	652.3 nm	750 nm	775 nm	643/20 nm
2840 cm^{-1}	798.1 nm	650.6 nm	750 nm	775 nm	643/20 nm
2860 cm^{-1}	796.8 nm	648.9 nm	750 nm	775 nm	643/20 nm
2880 cm^{-1}	795.6 nm	647.3 nm	750 nm	775 nm	643/20 nm
2900 cm^{-1}	794.3 nm	645.6 nm	750 nm	775 nm	643/20 nm
2920 cm^{-1}	793.0 nm	643.9 nm	750 nm	775 nm	643/20 nm
2940 cm^{-1}	791.8 nm	642.3 nm	750 nm	775 nm	643/20 nm
2960 cm^{-1}	790.5 nm	640.6 nm	750 nm	775 nm	643/20 nm
2980 cm^{-1}	798.3 nm	639.0 nm	750 nm	775 nm	643/20 nm
3000 cm^{-1}	788.0 nm	637.4 nm	750 nm	775 nm	643/20 nm
3020 cm^{-1}	786.8 nm	635.7 nm	750 nm	775 nm	643/20 nm
3040 cm^{-1}	785.6 nm	634.1 nm	750 nm	775 nm	643/20 nm

A.2 Femoral head sample preparation

Human femoral heads were collected following routine total hip arthroplasty surgery at Southampton General Hospital or Spire Southampton Hospital. Only tissue that would have been discarded was used, with approval of the Southampton and South West Hampshire Research Ethics Committee (194/99/1 & 210/01). Patient consent was obtained for every case.

Femoral head slices were prepared using an IsoMet™ low speed precision cutter from Buehler (Switzerland), with a diamond blade for precise and delicate cuts (Figure A.1). Femoral head samples were washed with PBS and fixed in a 4 % formaldehyde (v/v) solution for 72 hours at 4 °C, with gentle agitation.

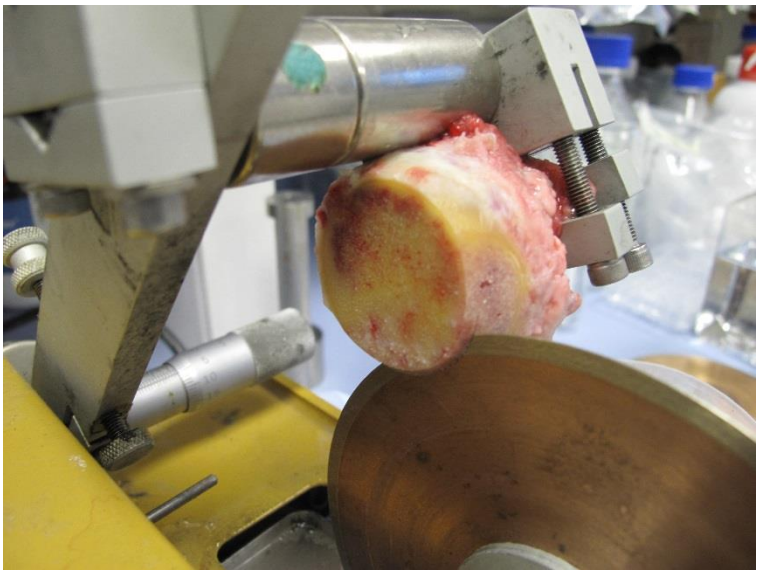

Figure A.1 – Femoral head slice preparation. Samples were cut using an IsoMet™ low speed precision cutter with a diamond blade.

Fixed samples were characterised using Raman spectroscopy as detailed in Chapter 3, section 3.2.10; and imaged using SHG and TPEAF, as described in Chapter 3, section 3.2.12.

Before starting the decalcification protocol, an X-ray image of the femoral head sample was acquired using a Faxitron® MX-20 system (Qados Ltd), to identify the starting point of mineralisation. Femoral head samples were washed with PBS and incubated in a decalcifying solution (5 % EDTA in 0.1 M Tris (v/v), pH 7.3) at 4 °C with gentle agitation. The decalcifying solution was freshly prepared and replenished twice a week. An X-ray image was acquired once a week to follow the process of decalcification of the femoral head sample and to determine the end-point of decalcification.

References

1. Dawson, J.I., et al., *Skeletal Regeneration: application of nanotopography and biomaterials for skeletal stem cell based bone repair.* Inflamm. Regen., 2012. **32**(3): p. 072-089.

2. Dawson, J.I., et al., *Concise Review: Bridging the Gap: Bone Regeneration Using Skeletal Stem Cell-Based Strategies—Where Are We Now?* Stem Cells, 2014. **32**(1): p. 35-44.

3. Lovell-Badge, R., *The future for stem cell research.* Nature, 2001. **414**(6859): p. 88-91.

4. Tare, R.S., et al., *Skeletal stem cells and bone regeneration: translational strategies from bench to clinic.* Proc. Inst. Mech. Eng. H, 2010. **224**(12): p. 1455-70.

5. Oreffo, R.O., *Centre for human development, stem cells & regeneration.* Regen. Med. , 2014. **9**(5): p. 563-7.

6. Srivastava, D. and K.N. Ivey, *Potential of stem-cell-based therapies for heart disease.* Nature, 2006. **441**(7097): p. 1097-1099.

7. Chidgey, A.P., et al., *Tolerance strategies for stem-cell-based therapies.* Nature, 2008. **453**(7193): p. 330-7.

8. Wickramasinghe, S.N., A. Porwit, and W.N. Erber, *Chapter 2 - Normal bone marrow cells: Development and cytology*, in *Blood and Bone Marrow Pathology (second edition)*, A. Porwit, J. McCullough, and W.N. Erber, Editors. 2011, Churchill Livingstone: Edinburgh. p. 19-44.

9. Bianco, P., *"Mesenchymal" stem cells.* Annu. Rev. Cell Dev. Biol. , 2014. **30**: p. 677-704.

10. Bianco, P., et al., *Bone marrow stromal stem cells: nature, biology, and potential applications.* Stem Cells, 2001. **19**(3): p. 180-92.

11. Bianco, P. and P.G. Robey, *Skeletal stem cells.* Development, 2015. **142**(6): p. 1023-1027.

12. Bianco, P. and P.G. Robey, *39 - Skeletal Stem Cells*, in *Handbook of Stem Cells*, R. Lanza, et al., Editors. 2004, Academic Press: Burlington. p. 415-424.

13. Bianco, P. and P.G. Robey, *Stem cells in tissue engineering.* Nature, 2001. **414**(6859): p. 118-21.

14. Bianco, P. and P.G. Robey, *Skeletal stem cells.* Development (Cambridge, England), 2015. **142**(6): p. 1023-1027.

15. Chamberlain, G., et al., *Concise review: mesenchymal stem cells: their phenotype, differentiation capacity, immunological features, and potential for homing.* Stem Cells, 2007. **25**(11): p. 2739-49.

16. Murray, I.R., et al., *Natural history of mesenchymal stem cells, from vessel walls to culture vessels.* Cell. Mol. Life Sci. , 2014. **71**(8): p. 1353-74.

17. Aarvold, A., et al., *From bench to clinic and back: skeletal stem cells and impaction bone grafting for regeneration of bone defects.* Journal of Tissue Engineering and Regenerative Medicine, 2014. **8**(10): p. 779-786.

18. Krause, U., A. Seckinger, and C.A. Gregory, *Assays of osteogenic differentiation by cultured human mesenchymal stem cells.* Methods Mol. Biol., 2011. **698**: p. 215-30.

19. Fink, T. and V. Zachar, *Adipogenic differentiation of human mesenchymal stem cells.* Methods Mol. Biol., 2011. **698**: p. 243-51.

20. Solchaga, L.A., K.J. Penick, and J.F. Welter, *Chondrogenic differentiation of bone marrow-derived mesenchymal stem cells: tips and tricks.* Methods Mol. Biol., 2011. **698**: p. 253-78.

21. Kallepitis, C., et al., *Quantitative volumetric Raman imaging of three dimensional cell cultures.* 2017. **8**: p. 14843.

22. Streets, A.M., et al., *Imaging without fluorescence: nonlinear optical microscopy for quantitative cellular imaging.* Anal Chem, 2014. **86**(17): p. 8506-13.

23. Notingher, I., et al., *In situ non-invasive spectral discrimination between bone cell phenotypes used in tissue engineering.* J. Cell. Biochem., 2004. **92**(6): p. 1180-92.

24. Downes, A., et al., *Raman spectroscopy and CARS microscopy of stem cells and their derivatives.* J. Raman Spectrosc., 2011. **42**(10): p. 1864-1870.

25. Robey, P.G., *Cell sources for bone regeneration: the good, the bad, and the ugly (but promising).* Tissue Eng. Part B Rev., 2011. **17**(6): p. 423-30.

26. Atkins, P. and J. de Paula, *Physical Chemistry for the Life Sciences*. 2011: W. H. Freeman.

27. Butcher, G., *Tour of the Electromagnetic Spectrum*. 2010.

28. Barry N. Taylor, Ambler Thompson, and NIST, eds. *The International System of Units (SI).* 2008: International Bureau of Weights and Measures

29. Bohren, C.F. and A.B. Fraser, *Colors of the sky.* The Physics Teacher, 1985. **23**(5): p. 267-272.

30. Wachsmann-Hogiu, S., T. Weeks, and T. Huser, *Chemical analysis in vivo and in vitro by Raman spectroscopy—from single cells to humans.* Current Opinion in Biotechnology, 2009. **20**(1): p. 63-73.

31. Patel, I.I., et al., *Coherent anti-Stokes Raman scattering for label-free biomedical imaging.* Journal of Optics, 2013. **15**(9): p. 094006.

32. Folick, A., W. Min, and M.C. Wang, *Label-free imaging of lipid dynamics using Coherent Anti-stokes Raman Scattering (CARS) and Stimulated Raman Scattering (SRS) microscopy.* Current Opinion in Genetics & Development, 2011. **21**(5): p. 585-90.

33. Rodriguez, L.G., S.J. Lockett, and G.R. Holtom, *Coherent anti-stokes Raman scattering microscopy: a biological review.* Cytometry A, 2006. **69**(8): p. 779-91.

34. Moura, C.C., et al., *Raman spectroscopy and coherent anti-Stokes Raman scattering imaging: prospective tools for monitoring skeletal cells and skeletal regeneration.* Journal of The Royal Society Interface, 2016. **13**(118).

35. Planck, M., *On the Theory of the Energy Distribution Law of the Normal Spectrum*. Verhandlungen der Deutschen Physikalischen Gesellschaft, 1900. **2**(237).

36. Banwell, C.N., in *Fundamentals of Molecular Spectroscopy (third edition)*. 1983, McGraw-Hill: England. p. 124-154.

37. Chan, J.W. and D.K. Lieu, *Label-free biochemical characterization of stem cells using vibrational spectroscopy*. Journal of Biophotonics, 2009. **2**(11): p. 656-68.

38. Chiang, H.K., et al., *In situ Raman spectroscopic monitoring of hydroxyapatite as human mesenchymal stem cells differentiate into osteoblasts*. Journal of Raman Spectroscopy, 2009. **40**(5): p. 546-549.

39. Hung, P.S., et al., *Detection of osteogenic differentiation by differential mineralized matrix production in mesenchymal stromal cells by Raman spectroscopy*. PLoS One, 2013. **8**(5): p. e65438.

40. Notingher, I., et al., *In situ spectral monitoring of mRNA translation in embryonic stem cells during differentiation in vitro*. Analytical Chemistry, 2004. **76**(11): p. 3185-93.

41. Tsai, T.H., et al., *Label-free identification and characterization of murine hair follicle stem cells located in thin tissue sections with Raman micro-spectroscopy*. Analyst, 2014. **139**(11): p. 2799-805.

42. Ichimura, T., et al., *Visualizing cell state transition using Raman spectroscopy*. PLoS One, 2014. **9**(1): p. e84478.

43. Notingher, I., et al., *In situ spectral monitoring of mRNA translation in embryonic stem cells during differentiation in vitro*. Anal. Chem. , 2004. **76**(11): p. 3185-93.

44. Notingher, I., et al., *Multivariate analysis of Raman spectra for in vitro non-invasive studies of living cells*. J. Mol. Struct. , 2005. **744–747**(0): p. 179-185.

45. Chan, J.W., et al., *Label-free separation of human embryonic stem cells and their cardiac derivatives using Raman spectroscopy*. Anal. Chem., 2009. **81**(4): p. 1324-31.

46. Pascut, F.C., et al., *Non-invasive label-free monitoring the cardiac differentiation of human embryonic stem cells in-vitro by Raman spectroscopy*. Biochim. Biophys. Acta, 2013. **1830**(6): p. 3517-3524.

47. Schulze, H.G., et al., *Assessing Differentiation Status of Human Embryonic Stem Cells Noninvasively Using Raman Microspectroscopy*. Anal. Chem., 2010. **82**(12): p. 5020-5027.

48. Tan, Y., et al., *Comparative study using Raman microspectroscopy reveals spectral signatures of human induced pluripotent cells more closely resemble those from human embryonic stem cells than those from differentiated cells*. Analyst, 2012. **137**(19): p. 4509-4515.

49. Chiang, H.K., et al., *In situ Raman spectroscopic monitoring of hydroxyapatite as human mesenchymal stem cells differentiate into osteoblasts*. J. Raman Spectrosc. , 2009. **40**(5): p. 546-549.

50. Pijanka, J.K., et al., *Vibrational spectroscopy differentiates between multipotent and pluripotent stem cells*. Analyst, 2010. **135**(12): p. 3126-32.

51. James, S., et al., *Multiparameter Analysis of Human Bone Marrow Stromal Cells Identifies Distinct Immunomodulatory and Differentiation-Competent Subtypes.* Stem Cell Rep., 2015. **4**(6): p. 1004-1015.

52. McManus, L.L., et al., *Raman spectroscopic monitoring of the osteogenic differentiation of human mesenchymal stem cells.* Analyst, 2011. **136**(12): p. 2471-81.

53. Ojansivu, M., et al., *Bioactive glass ions as strong enhancers of osteogenic differentiation in human adipose stem cells.* Acta Biomater., 2015. **21**(0): p. 190-203.

54. Notingher, I., et al., *In situ spectroscopic study of nucleic acids in differentiating embryonic stem cells.* Vib. Spectrosc., 2004. **35**(1–2): p. 199-203.

55. Mitchell, A., et al., *Detection of early stage changes associated with adipogenesis using Raman spectroscopy under aseptic conditions.* Cytometry A, 2015. **87**(11): p. 1012-9.

56. Downes, A., R. Mouras, and A. Elfick, *A versatile CARS microscope for biological imaging.* J. Raman Spectrosc., 2009. **40**(7): p. 757-762.

57. Lloyd, G.R., et al., *Discrimination between benign, primary and secondary malignancies in lymph nodes from the head and neck utilising Raman spectroscopy and multivariate analysis.* Analyst, 2013. **138**(14): p. 3900-8.

58. Camp Jr, C.H. and M.T. Cicerone, *Chemically sensitive bioimaging with coherent Raman scattering.* Nature Photonics, 2015. **9**: p. 295.

59. Tolles, W.M., et al., *A Review of the Theory and Application of Coherent Anti-Stokes Raman Spectroscopy (CARS).* Applied Spectroscopy, 1977. **31**(4): p. 253-271.

60. Evans, C.L. and X.S. Xie, *Coherent Anti-Stokes Raman Scattering Microscopy: Chemical Imaging for Biology and Medicine.* Annual Review of Analytical Chemistry, 2008. **1**(1): p. 883-909.

61. Pezacki, J.P., et al., *Chemical contrast for imaging living systems: molecular vibrations drive CARS microscopy.* Nature Chemical Biology, 2011. **7**(3): p. 137-45.

62. Steuwe, C., et al., *CARS based label-free assay for assessment of drugs by monitoring lipid droplets in tumour cells.* J. Biophotonics, 2014. **7**(11-12): p. 906-913.

63. Cheng, J.-X. and X.S. Xie, *Coherent Anti-Stokes Raman Scattering Microscopy: Instrumentation, Theory, and Applications.* The Journal of Physical Chemistry B, 2004. **108**(3): p. 827-840.

64. Konorov, S.O., et al., *In situ analysis of living embryonic stem cells by coherent anti-stokes Raman microscopy.* Analytical chemistry, 2007. **79**(18): p. 7221-5.

65. Krafft, C., B. Dietzek, and J. Popp, *Raman and CARSmicrospectroscopy of cells and tissues.* Analyst, 2009. **134**(6): p. 1046-1057.

66. Evans, C.L., et al., *Chemical imaging of tissue in vivo with video-rate coherent anti-Stokes Raman scattering microscopy.* Proc. Natl. Acad. Sci. U. S. A., 2005. **102**(46): p. 16807-12.

67. Evans, C.L. and X.S. Xie, *Coherent Anti-Stokes Raman Scattering Microscopy: Chemical Imaging for Biology and Medicine.* Annu. Rev. Anal. Chem., 2008. **1**(1): p. 883-909.

68. Pezacki, J.P., et al., *Chemical contrast for imaging living systems: molecular vibrations drive CARS microscopy.* Nat. Chem. Biol., 2011. **7**(3): p. 137-45.

69. Krafft, C., B. Dietzek, and J. Popp, *Raman and CARS microspectroscopy of cells and tissues.* Analyst, 2009. **134**(6): p. 1046-1057.

70. Salameh, T.S., et al., *An ex vivo co-culture model system to evaluate stromal-epithelial interactions in breast cancer.* Int. J. Cancer, 2013. **132**(2): p. 288-96.

71. Konorov, S.O., et al., *In situ analysis of living embryonic stem cells by coherent anti-stokes Raman microscopy.* Anal. Chem., 2007. **79**(18): p. 7221-5.

72. Schie, I.W., et al., *Simultaneous forward and epi-CARS microscopy with a single detector by time-correlated single photon counting.* Opt. Express, 2008. **16**(3): p. 2168-75.

73. Jo, S.J., et al., *Temporary increase of PPAR-gamma and transient expression of UCP-1 in stromal vascular fraction isolated human adipocyte derived stem cells during adipogenesis.* Lipids, 2011. **46**(6): p. 487-94.

74. Di Napoli, C., et al., *Hyperspectral and differential CARS microscopy for quantitative chemical imaging in human adipocytes.* Biomed. Opt. Express, 2014. **5**(5): p. 1378-90.

75. Mouras, R., et al., *Label-free assessment of adipose-derived stem cell differentiation using coherent anti-Stokes Raman scattering and multiphoton microscopy.* J. Biomed. Opt., 2012. **17**(11): p. 116011.

76. Mortati, L., C. Divieto, and M.P. Sassi, *CARS and SHG microscopy to follow collagen production in living human corneal fibroblasts and mesenchymal stem cells in fibrin hydrogel 3D cultures.* J. Raman Spectrosc., 2012. **43**(5): p. 675-680.

77. Campagnola, P., *Second Harmonic Generation Imaging Microscopy: Applications to Diseases Diagnostics.* Analytical chemistry, 2011. **83**(9): p. 3224-3231.

78. So, P.T., *Two-photon Fluorescence Light Microscopy*, in *eLS*. 2001.

79. Cox, G. and E. Kable, *Second-Harmonic Imaging of Collagen*, in *Cell Imaging Techniques: Methods and Protocols*, D.J. Taatjes and B.T. Mossman, Editors. 2006, Humana Press: Totowa, NJ. p. 15-35.

80. Campagnola, P.J. and L.M. Loew, *Second-harmonic imaging microscopy for visualizing biomolecular arrays in cells, tissues and organisms.* Nat Biotechnol, 2003. **21**(11): p. 1356-60.

81. Campagnola, P.J., et al., *Three-dimensional high-resolution second-harmonic generation imaging of endogenous structural proteins in biological tissues.* Biophys J, 2002. **82**(1 Pt 1): p. 493-508.

82. Awasthi, S., et al., *Label-free identification and characterization of human pluripotent stem cell-derived cardiomyocytes using second harmonic generation (SHG) microscopy.* J Biophotonics, 2012. **5**(1): p. 57-66.

83. Chen, X., et al., *Second harmonic generation microscopy for quantitative analysis of collagen fibrillar structure.* Nat. Protocols, 2012. **7**(4): p. 654-669.

84. Mouw, J.K., G. Ou, and V.M. Weaver, *Extracellular matrix assembly: a multiscale deconstruction.* Nat Rev Mol Cell Biol, 2014. **15**(12): p. 771-785.

85. Exposito, J.-Y., et al., *The Fibrillar Collagen Family.* International Journal of Molecular Sciences, 2010. **11**(2): p. 407-426.

86. Buckwalter, J.A., H.J. Mankin, and A.J. Grodzinsky, *Articular cartilage and osteoarthritis.* Instr Course Lect, 2005. **54**: p. 465-80.

87. Reddi, A.H., *Structure and Function of Cartilage*, in *Articular Cartilage*. 2013, CRC Press. p. 1-50.

88. Sophia Fox, A.J., A. Bedi, and S.A. Rodeo, *The Basic Science of Articular Cartilage: Structure, Composition, and Function.* Sports Health, 2009. **1**(6): p. 461-468.

89. Aloísio, M.G., et al., *Second harmonic generation imaging of the collagen architecture in prostate cancer tissue.* Biomedical Physics & Engineering Express, 2018. **4**(2): p. 025026.

90. Saitou, T., H. Kiyomatsu, and T. Imamura, *Quantitative Morphometry for Osteochondral Tissues Using Second Harmonic Generation Microscopy and Image Texture Information.* Scientific Reports, 2018. **8**(1): p. 2826.

91. Albro, M.B., et al., *Raman spectroscopic imaging for quantification of depth-dependent and local heterogeneities in native and engineered cartilage.* NPJ Regen Med, 2018. **3**: p. 3.

92. Zoumi, A., A. Yeh, and B.J. Tromberg, *Imaging cells and extracellular matrix in vivo by using second-harmonic generation and two-photon excited fluorescence.* Proceedings of the National Academy of Sciences, 2002. **99**(17): p. 11014-11019.

93. Heikal, A.A., *Intracellular coenzymes as natural biomarkers for metabolic activities and mitochondrial anomalies.* Biomark Med, 2010. **4**(2): p. 241-63.

94. Denk, W., J. Strickler, and W. Webb, *Two-photon laser scanning fluorescence microscopy.* Science, 1990. **248**(4951): p. 73-76.

95. Shirshin, E.A., et al., *Two-photon autofluorescence lifetime imaging of human skin papillary dermis in vivo: assessment of blood capillaries and structural proteins localization.* Scientific Reports, 2017. **7**(1): p. 1171.

96. Knight, A. and N. Billington, *Distinguishing GFP from cellular autofluorescence.* Biophotonics International, 2001. **8**: p. 42-50.

97. Rice, W.L., D.L. Kaplan, and I. Georgakoudi, *Two-Photon Microscopy for Non-Invasive, Quantitative Monitoring of Stem Cell Differentiation.* PLOS ONE, 2010. **5**(4): p. e10075.

98. Meleshina, A.V., et al., *Two-photon FLIM of NAD(P)H and FAD in mesenchymal stem cells undergoing either osteogenic or chondrogenic differentiation.* Stem Cell Research & Therapy, 2017. **8**(1): p. 15.

99. Hofemeier, A.D., et al., *Label-free nonlinear optical microscopy detects early markers for osteogenic differentiation of human stem cells.* Sci Rep, 2016. **6**: p. 26716.

100. Mouras, R., et al., *Non linear optical microscopy of adipose-derived stem cells induced towards osteoblasts and adipocytes.* Proc SPIE Int Soc Opt Eng, 2011. **8086**.

101. Mansfield, J., et al., *The elastin network: its relationship with collagen and cells in articular cartilage as visualized by multiphoton microscopy.* J Anat, 2009. **215**(6): p. 682-91.

102. Kong, K., et al., *Raman spectroscopy for medical diagnostics — From in-vitro biofluid assays to in-vivo cancer detection.* Adv. Drug Deliv. Rev. , 2015. **89**: p. 121-134.

103. Bergholt, M.S., et al., *Fiber-optic Raman spectroscopy probes gastric carcinogenesis in vivo at endoscopy.* J. Biophotonics, 2013. **6**(1): p. 49-59.

104. Jermyn, M., et al., *Intraoperative brain cancer detection with Raman spectroscopy in humans.* Sci. Transl. Med., 2015. **7**(274): p. 274ra19-274ra19.

105. Desroches, J., et al., *A new method using Raman spectroscopy for in vivo targeted brain cancer tissue biopsy.* Scientific Reports, 2018. **8**(1): p. 1792.

106. Iping Petterson, I.E., et al., *Characterisation of a fibre optic Raman probe within a hypodermic needle.* Anal. Bioanal. Chem. , 2015. **407**(27): p. 8311-20.

107. Buckley, K., et al., *Measurement of abnormal bone composition in vivo using noninvasive Raman spectroscopy.* IBMS BoneKEy, 2014. **11**.

108. Sulé-Suso, J., et al., *Vibrational spectroscopy in stem cell characterisation: is there a niche?* Trends Biotechnol., 2014. **32**(5): p. 254-262.

109. Folick, A., W. Min, and M.C. Wang, *Label-free imaging of lipid dynamics using Coherent Anti-stokes Raman Scattering (CARS) and Stimulated Raman Scattering (SRS) microscopy.* Curr. Opin. Genet. Dev. , 2011. **21**(5): p. 585-90.

110. Fitter, S., et al., *The Mesenchymal Precursor Cell Marker Antibody STRO-1 Binds to Cell Surface Heat Shock Cognate 70.* STEM CELLS, 2017. **35**(4): p. 940-951.

111. Gothard, D., et al., *Prospective isolation of human bone marrow stromal cell subsets: A comparative study between Stro-1-, CD146- and CD105-enriched populations.* J Tissue Eng, 2014. **5**: p. 2041731414551763.

112. Simmons, P.J. and B. Torok-Storb, *Identification of stromal cell precursors in human bone marrow by a novel monoclonal antibody, STRO-1.* Blood, 1991. **78**(1): p. 55-62.

113. Tare, R.S., et al., *Isolation, differentiation, and characterisation of skeletal stem cells from human bone marrow in vitro and in vivo.* Methods Mol Biol, 2012. **816**: p. 83-99.

114. Xavier, M., et al., *Mechanical phenotyping of primary human skeletal stem cells in heterogeneous populations by real-time deformability cytometry.* Integrative Biology, 2016. **8**(5): p. 616-623.

115. Stewart, K., et al., *Further Characterization of Cells Expressing STRO-1 in Cultures of Adult Human Bone Marrow Stromal Cells.* Journal of Bone and Mineral Research, 1999. **14**(8): p. 1345-1356.

116. Williams, E.L., K. White, and R.O. Oreffo, *Isolation and enrichment of Stro-1 immunoselected mesenchymal stem cells from adult human bone marrow.* Methods Mol Biol, 2013. **1035**: p. 67-73.

117. de Andrés, M.C., et al., *Suppressors of cytokine signalling (SOCS) are reduced in osteoarthritis.* Biochemical and biophysical research communications, 2011. **407**(1): p. 54-59.

118. Mirmalek-Sani, S.H., et al., *Characterization and multipotentiality of human fetal femur-derived cells: implications for skeletal tissue regeneration.* Stem Cells, 2006. **24**(4): p. 1042-53.

119. Tare, R.S., et al., *Tissue engineering strategies for cartilage generation--micromass and three dimensional cultures using human chondrocytes and a continuous cell line.* Biochem Biophys Res Commun, 2005. **333**(2): p. 609-21.

120. Kubista, M., et al., *The real-time polymerase chain reaction.* Molecular Aspects of Medicine, 2006. **27**(2): p. 95-125.

121. Trevisan, J., et al., *IRootLab: a free and open-source MATLAB toolbox for vibrational biospectroscopy data analysis.* Bioinformatics, 2013. **29**(8): p. 1095-7.

122. Pologruto, T.A., B.L. Sabatini, and K. Svoboda, *ScanImage: flexible software for operating laser scanning microscopes.* Biomed Eng Online, 2003. **2**: p. 13.

123. Preibisch, S., S. Saalfeld, and P. Tomancak, *Globally optimal stitching of tiled 3D microscopic image acquisitions.* Bioinformatics, 2009. **25**(11): p. 1463-5.

124. Bredfeldt, J.S., et al., *Computational segmentation of collagen fibers from second-harmonic generation images of breast cancer.* J Biomed Opt, 2014. **19**(1): p. 16007.

125. Bredfeldt, J.S., et al., *Automated quantification of aligned collagen for human breast carcinoma prognosis.* Journal of Pathology Informatics, 2014. **5**: p. 28.

126. Zumbusch, A., G.R. Holtom, and X.S. Xie, *Three-dimensional vibrational imaging by coherent anti-Stokes Raman scattering.* Phys. Rev. Lett., 1999. **82**(20): p. 4142-4145.

127. Min, W., et al., *Coherent nonlinear optical imaging: beyond fluorescence microscopy.* Annu. Rev. Phys. Chem., 2011. **62**: p. 507-30.

128. Camp Jr, C.H. and M.T. Cicerone, *Chemically sensitive bioimaging with coherent Raman scattering.* Nat Photon, 2015. **9**(5): p. 295-305.

129. Legare, F., et al., *Towards CARS Endoscopy.* Opt. Express, 2006. **14**(10): p. 4427-32.

130. Potma, E.O., C.L. Evans, and X.S. Xie, *Heterodyne coherent anti-Stokes Raman scattering (CARS) imaging.* Opt. Lett., 2006. **31**(2): p. 241-243.

131. Petrov, G.I., et al., *Comparison of coherent and spontaneous Raman microspectroscopies for noninvasive detection of single bacterial endospores.* Proc. Natl. Acad. Sci. U. S. A., 2007. **104**(19): p. 7776-9.

132. Wang, H.-W., et al., *Chasing lipids in health and diseases by coherent anti-Stokes Raman scattering microscopy.* Vib. Spectrosc., 2009. **50**(1): p. 160-167.

133. Chien, C.-H., et al., *Label-free imaging of Drosophila in vivo by coherent anti-Stokes Raman scattering and two-photon excitation autofluorescence microscopy.* J. Biomed. Opt., 2011. **16**(1): p. 016012-016012.

134. Movasaghi, Z., S. Rehman, and I.U. Rehman, *Raman Spectroscopy of Biological Tissues.* Appl. Spectrosc. Rev. , 2007. **42**(5): p. 493-541.

135. Matthäus, C., et al., *Label-Free Detection of Mitochondrial Distribution in Cells by Nonresonant Raman Microspectroscopy.* Biophys. J., 2007. **93**(2): p. 668-673.

136. Rinia, H.A., et al., *Quantitative label-free imaging of lipid composition and packing of individual cellular lipid droplets using multiplex CARS microscopy.* Biophys. J., 2008. **95**(10): p. 4908-4914.

137. Brasaemle, D.L., et al., *Adipose differentiation-related protein is an ubiquitously expressed lipid storage droplet-associated protein.* J. Lipid Res., 1997. **38**(11): p. 2249-63.

138. Tauchi-Sato, K., et al., *The Surface of Lipid Droplets Is a Phospholipid Monolayer with a Unique Fatty Acid Composition.* J. Biol. Chem., 2002. **277**(46): p. 44507-44512.

139. Xu, Y., et al., *Adipocyte differentiation induced using nonspecific siRNA controls in cultured human mesenchymal stem cells.* RNA, 2007. **13**(8): p. 1179-1183.

140. Kinkel, A.D., et al., *Oil red-O stains non-adipogenic cells: a precautionary note.* Cytotechnology, 2004. **46**(1): p. 49-56.

141. Farmer, S.R., *Regulation of PPAR[gamma] activity during adipogenesis.* Int. J. Obes., 2005. **29**(S1): p. S13-S16.

142. Furuhashi, M., et al., *Treatment of diabetes and atherosclerosis by inhibiting fatty-acid-binding protein aP2.* Nature, 2007. **447**(7147): p. 959-965.

143. Cheung, K.S., et al., *MicroRNA-146a regulates human foetal femur derived skeletal stem cell differentiation by down-regulating SMAD2 and SMAD3.* PLoS One, 2014. **9**(6): p. e98063.

144. McNamara, L.E., et al., *Nanotopographical Control of Stem Cell Differentiation.* J. Tissue Eng., 2010. **2010**: p. 120623.

145. Ali, A.T., et al., *Alkaline phosphatase is involved in the control of adipogenesis in the murine preadipocyte cell line, 3T3-L1.* Clin. Chim. Acta, 2005. **354**(1-2): p. 101-9.

146. Bianco, P., et al., *Alkaline phosphatase positive precursors of adipocytes in the human bone marrow.* Br. J. Haematol., 1988. **68**(4): p. 401-3.

147. Budd, E., et al., *MiR-146b is down-regulated during the chondrogenic differentiation of human bone marrow derived skeletal stem cells and up-regulated in osteoarthritis.* 2017. **7**: p. 46704.

148. Serafini, M., et al., *Establishment of bone marrow and hematopoietic niches in vivo by reversion of chondrocyte differentiation of human bone marrow stromal cells.* Stem Cell Research, 2014. **12**(3): p. 659-672.

149. Khademhosseini, A. and R. Langer, *A decade of progress in tissue engineering.* Nat. Protocols, 2016. **11**(10): p. 1775-1781.

150. Cheng, J.X. and X.S. Xie, *Coherent Raman Scattering Microscopy*. 2012: Taylor & Francis.

151. Downes, A., et al., *Raman spectroscopy and CARS microscopy of stem cells and their derivatives.* J Raman Spectrosc, 2011. **42**(10): p. 1864-1870.

152. Smus, J.P., et al., *Tracking adipogenic differentiation of skeletal stem cells by label-free chemically selective imaging.* Chemical Science, 2015. **6**(12): p. 7089-7096.

153. Mortati, L., C. Divieto, and M.P. Sassi, *CARS and SHG microscopy to follow collagen production in living human corneal fibroblasts and mesenchymal stem cells in fibrin hydrogel 3D cultures.* Journal of Raman Spectroscopy, 2012. **43**(5): p. 675-680.

154. Hoover, E.E. and J.A. Squier, *Advances in multiphoton microscopy technology.* Nat Photon, 2013. **7**(2): p. 93-101.

155. Li, S., et al., *Application of an acoustofluidic perfusion bioreactor for cartilage tissue engineering.* Lab Chip, 2014. **14**(23): p. 4475-85.

156. Lewis, M.C., et al., *Extracellular Matrix Deposition in Engineered Micromass Cartilage Pellet Cultures: Measurements and Modelling.* PLOS ONE, 2016. **11**(2): p. e0147302.

157. Gentili, C. and R. Cancedda, *Cartilage and bone extracellular matrix.* Curr Pharm Des, 2009. **15**(12): p. 1334-48.

158. Li, S., et al., *Chondrogenic potential of human articular chondrocytes and skeletal stem cells: a comparative study.* Journal of Biomaterials Applications, 2015. **29**(6): p. 824-36.

159. Bancroft, J.D., C. Layton, and S.K. Suvarna. *Bancroft's theory and practice of histological techniques*. 2013.

160. Villalvilla, A., et al., *Lipid Transport and Metabolism in Healthy and Osteoarthritic Cartilage.* International Journal of Molecular Sciences, 2013. **14**(10): p. 20793-20808.

161. Ghadially, F.N., G. Meachim, and D.H. Collins, *Extra-cellular Lipid in the Matrix of Human Articular Cartilage.* Annals of the Rheumatic Diseases, 1965. **24**(2): p. 136-146.

162. Cox, G., et al., *3-dimensional imaging of collagen using second harmonic generation.* J Struct Biol, 2003. **141**(1): p. 53-62.

163. Holmes, D.F. and K.E. Kadler, *The 10+4 microfibril structure of thin cartilage fibrils.* Proceedings of the National Academy of Sciences, 2006. **103**(46): p. 17249-17254.

164. Wen, C.K. and M.C. Goh, *Fibrous long spacing type collagen fibrils have a hierarchical internal structure.* Proteins, 2006. **64**(1): p. 227-33.

165. Diaspro, A., *Confocal and Two-Photon Microscopy: Foundations, Applications and Advances*. 2001: Wiley.

166. Rose, F.R. and R.O. Oreffo, *Bone tissue engineering: hope vs hype.* Biochem Biophys Res Commun, 2002. **292**(1): p. 1-7.

167. Vacanti, J.P. and R. Langer, *Tissue engineering: the design and fabrication of living replacement devices for surgical reconstruction and transplantation.* The Lancet. **354**: p. S32-S34.

168. Shimomura, K., et al., *Scaffold-free tissue engineering for injured joint surface restoration.* J Exp Orthop, 2018. **5**(1): p. 2.

169. Yang, Y., et al., *Mesenchymal Stem Cell-Derived Extracellular Matrix Enhances Chondrogenic Phenotype of and Cartilage Formation by Encapsulated Chondrocytes in vitro and in vivo.* Acta Biomater, 2018.

170. Zumbusch, A., G.R. Holtom, and X.S. Xie, *Three-Dimensional Vibrational Imaging by Coherent Anti-Stokes Raman Scattering.* Physical Review Letters, 1999. **82**(20): p. 4142-4145.

171. Khmaladze, A., et al., *Hyperspectral imaging and characterization of live cells by broadband coherent anti-Stokes Raman scattering (CARS) microscopy with singular value decomposition (SVD) analysis.* Appl Spectrosc, 2014. **68**(10): p. 1116-22.

172. Bradley, J., et al., *Quantitative imaging of lipids in live mouse oocytes and early embryos using CARS microscopy.* Development (Cambridge, England), 2016. **143**(12): p. 2238-2247.

173. Nan, X., J.X. Cheng, and X.S. Xie, *Vibrational imaging of lipid droplets in live fibroblast cells with coherent anti-Stokes Raman scattering microscopy.* J Lipid Res, 2003. **44**(11): p. 2202-8.

174. Nan, X., E.O. Potma, and X.S. Xie, *Nonperturbative chemical imaging of organelle transport in living cells with coherent anti-stokes Raman scattering microscopy.* Biophys J, 2006. **91**(2): p. 728-35.

175. Fu, Y., et al., *Characterization of photodamage in coherent anti-Stokes Raman scattering microscopy.* Opt Express, 2006. **14**(9): p. 3942-51.

176. Minamikawa, T., et al., *Photo-Induced Cell Damage Analysis for Single- and Multifocus Coherent Anti-Stokes Raman Scattering Microscopy.* Journal of Spectroscopy, 2017. **2017**: p. 8.

177. Pegoraro, A.F., et al., *Hyperspectral multimodal CARS microscopy in the fingerprint region.* J Biophotonics, 2014. **7**(1-2): p. 49-58.

178. Downes, A., et al., *Raman spectroscopy and CARS microscopy of stem cells and their derivatives().* Journal of Raman spectroscopy : JRS, 2011. **42**(10): p. 1864-1870.

179. Camp, C.H., Jr., et al., *High-Speed Coherent Raman Fingerprint Imaging of Biological Tissues.* Nat Photonics, 2014. **8**: p. 627-634.

180. Parekh, S.H., et al., *Label-Free Cellular Imaging by Broadband Coherent Anti-Stokes Raman Scattering Microscopy.* Biophysical Journal, 2010. **99**(8): p. 2695-2704.

181. Long, D.A., *Infrared and Raman characteristic group frequencies. Tables and charts George Socrates John Wiley and Sons, Ltd, Chichester, Third Edition, 2001. Price £135.* Journal of Raman Spectroscopy, 2004. **35**(10): p. 905-905.

182. Bonifacio, A., et al., *Chemical imaging of articular cartilage sections with Raman mapping, employing uni- and multi-variate methods for data analysis.* Analyst, 2010. **135**(12): p. 3193-204.

183. Gasior-Glogowska, M., et al., *Structural alteration of collagen fibres--spectroscopic and mechanical studies.* Acta Bioeng Biomech, 2010. **12**(4): p. 55-62.

184. Alebrahim, M.A., C. Krafft, and J. Popp, *Raman imaging to study structural and chemical features of the dentin enamel junction.* IOP Conference Series: Materials Science and Engineering, 2015. **92**(1): p. 012014.

185. Chen, X., et al., *Second harmonic generation microscopy for quantitative analysis of collagen fibrillar structure.* Nature Protocols, 2012. **7**: p. 654.

186. Mandair, G.S. and M.D. Morris, *Contributions of Raman spectroscopy to the understanding of bone strength.* BoneKEy Rep, 2015. **4**.

187. Camp Jr, C.H. and M.T. Cicerone, *Chemically sensitive bioimaging with coherent Raman scattering.* Nat. Photon., 2015. **9**(5): p. 295-305.

188. Zhang, D., et al., *Fast Vibrational Imaging of Single Cells and Tissues by Stimulated Raman Scattering Microscopy.* Accounts Chem. Res., 2014. **47**(8): p. 2282-2290.

189. Cheng, J.X. and X.S. Xie, *Vibrational spectroscopic imaging of living systems: An emerging platform for biology and medicine.* Science, 2015. **350**(6264): p. aaa8870.

190. Ozeki, Y., et al., *High-speed molecular spectral imaging of tissue with stimulated Raman scattering.* Nat. Photon., 2012. **6**(12): p. 845-851.

191. Leica-Microsystems. *CARS Microscope - Label Free Imaging Leica TCS SP8 CARS*. 2016.

192. Latka, I., et al., *Fiber optic probes for linear and nonlinear Raman applications – Current trends and future development.* Laser Photonics Rev., 2013. **7**(5): p. 698-731.